Molecular Dynamics Investigation of Fast Ion Transport in Oxide Frameworks

A dissertation submitted to the department of physics And the Committee of the Doctoral Studies of IIT Guwahati in partial fulfillment of the requirements for the Degree of

Doctor of Philosophy

By

Kartik Sau

Department of Physics

Indian Institute of Technology Guwahati

Guwahati-781039, India

February, 2017

Synopsis

Introduction

Ever-growing consumer appetite for smaller, light-weight and powerful electronic devices have resulted unprecedented demand for the development of the high energy density rechargeable battery. Further, batteries and fuel cells are promising portable power sources for larger scale applications such as powering motor vehicles, as an environment friendly alternate to fossil fuels. Fast ion conducting solids are an integrated part of the batteries both as electrolyte and electrode materials. Li –conducting high energy density batteries already have a major market share in powering electronic gadgets [1-9]. However, Na based batteries are probably more attractive [10], particularly for large scale applications, owing to their natural abundance, better suited electrode potential and higher operating temperatures [11-16]. Thus they are both cost-effective and safer.

The understanding of microscopic mechanism of ion transport in solids, and the factors influencing conduction are invaluable in the search of potential materials for the battery applications [17]. Due to the revolutionary advances in computer hardware and algorithms, atomistic simulation techniques such as, molecular dynamics and Monte Carlo methods, has emerged as powerful tools in elucidating many microscopic structural and dynamical properties of interest which are generally hard to obtain from experiments [18, 19].

The thesis report detailed molecular dynamics investigation of microscopic mechanism and factors influencing ion transport in two promising oxide frameworks,

1. $Na_2M_2TeO_6$, where M = Ni, Zn, Co and Mg − an Na^+ conductor with a layered framework [20], and
2. $Li_{1+x}Al_xTi_{2-x}P_3O_{12}$, where $0 \leq x \leq 0.67$ − an Li^+ conductor having NASICON structure [21, 22].

The thesis is organized into six chapters, as follows,

Chapter 1 *provides an introduction to the thesis with a brief review of fast ion transport in different matrices, and the motivation for the research work carried out.*

A survey of the state of the art in the field is presented, covering several classes of fast ion conductors, including covalent framework solids such as, the NASICONs [23, 24], argyrodites [25], garnets [26], β-alumina [27], several soft framework conductors such as AgI,

CuI, Ag_2X (X=S, Se and Te) etc., fluorites, proton conductors and perovskites. The atomic level insights derived from modeling and simulation studies in these matrices are highlighted.

Chapter 2 *provides an introduction to the computational techniques employed in the studies, namely, molecular dynamics (MD).*

The MD studies reported in this thesis employs the interatomic potential of the Parrinello-Rahman-Vashishta form [28, 29],

$$V_{ij}(r_{ij}) = \frac{q_i q_j}{4\pi\varepsilon_0 r_{ij}} + \frac{A_{ij}\left(\sigma_i + \sigma_j\right)^{n_{ij}}}{r_{ij}^{\,n_{ij}}} - \frac{P_{ij}}{r_{ij}^{\,4}} - \frac{C_{ij}}{r_{ij}^{\,6}} \qquad (1)$$

where q_i and σ_i are respectively the effective charge and ionic radius of i^{th} ion. r_{ij} is the inter-atomic distance, A_{ij} and C_{ij} are the overlap-repulsive energy and dispersion terms respectively between ion pairs *i* and *j*. An overview of MD algorithm for micro-canonical (NVE), canonical (NVT) and isobaric-isothermal (NPT) ensembles is discussed. Implementation of periodic boundary conditions (PBC) for general non-cubic simulation cells, and Ewald summation technique for improving convergence of long-range coulombic interactions are discussed. The velocity-Verlet scheme for propagation of atomic trajectories, and conservation properties in MD simulations are outlined. Calculation of various structural, thermo-dynamic and dynamical properties employed in the study are described. A brief discussion on the advantages and limitations of these techniques are also included.

Chapter 3 *reports the interatomic potential developed for $Na_2M_2TeO_6$ (M=Ni, Zn, Co and Mg). The gross structural and ion transport properties based on this model is critically compared to available experimental data. Fresh insights on the mechanism of Na^+ transport in $Na_2Ni_2TeO_6$ is provided.*

$Na_2M_2TeO_6$, where M = Ni, Zn, Co or Mg, is an Na^+ fast ion conductor reported recently [20]. These solids consist of edge shared M-O and Te-O octahedral layers spanning the ab-plane, with the Na^+ ions occupying the inter-layer forming three dimensional hexagonal structure. The Ni-system, $Na_2Ni_2TeO_6$ (figure 1), has the highest ionic conductivity of the series (σ = 0.11S/cm at 573 K) which compares well with some of the best known fast ion conductors such as, β –alumina and NASICONs [27, 30-32]. The interatomic forces to describe $Na_2M_2TeO_6$ (M=Ni, Zn, Co and Mg) is parameterized employing empirical fitting to the experimental structure and conductivity. Simulations are carried out both in NVE and NPT-

MD ensembles, and MD trajectories are analyzed for critical comparison with reported X-ray structure and ionic conductivity over the range of 500-800 K. The Na^+ transport, as expected, is observed to be 2-dimentional, confined to the interlayer of the metal-oxide polyhedral slabs. The population of Na^+ at the three sites, Na1, Na2 and Na3, is found to be in qualitative agreement with those reported in experimental studies. Potential energy profiles of the individual Na^+ ions mapped on the interlayer shows that Na2 sites are the only potential energy minima, despite the fact that Na1 and Na2 sites nearly equally populated.

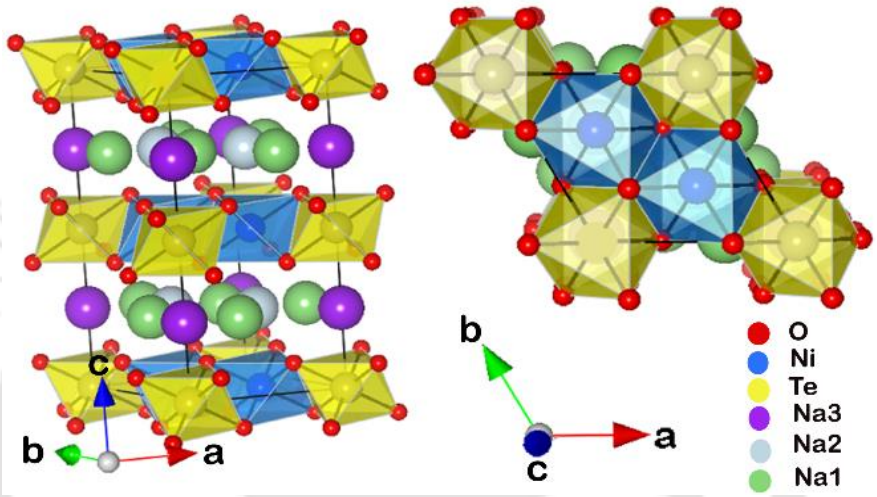

Figure 1. Views of the $Na_2Ni_2TeO_6$ structure having edge-shared octahedral layers parallel to the ab-plane; NiO_6 –octahedra (blue) and TeO_6-octahedra (yellow). A single rhombohedral unit cell is shown (along with the fringe atoms on the cell edges and oxygens (red) necessary for completing the octahedral). The Na-sites, Na1 (green), Na2 (light blue) and Na3 (violet), are also shown.

This hints upon entropic contribution playing a significant role in dictating the Na^+ distribution across the two sites. Based on the typical separation Na^+ ions maintains (for example, the Na-Na radial distribution suggest that simultaneous occupancy of nearest Na1 and Na2 are forbidden), and the topology of the sites it is proposed that Na^+ disorder is essential for their transport in $Na_2Ni_2TeO_6$.

Chapter 4 *discusses a series of MD simulations intended to gain better insights on role of entropic effects on ion transport. In these virtual experiments, the nature of ion transport at different interlayers of* $Na_2Ni_2TeO_6$ *having different concentration of* Na^+ *ions are investigated. The results predict a gradual crossover from an energy driven to entropy driven transport of* Na^+ *ions with the* Na^+ *concentration at the interlayers.*

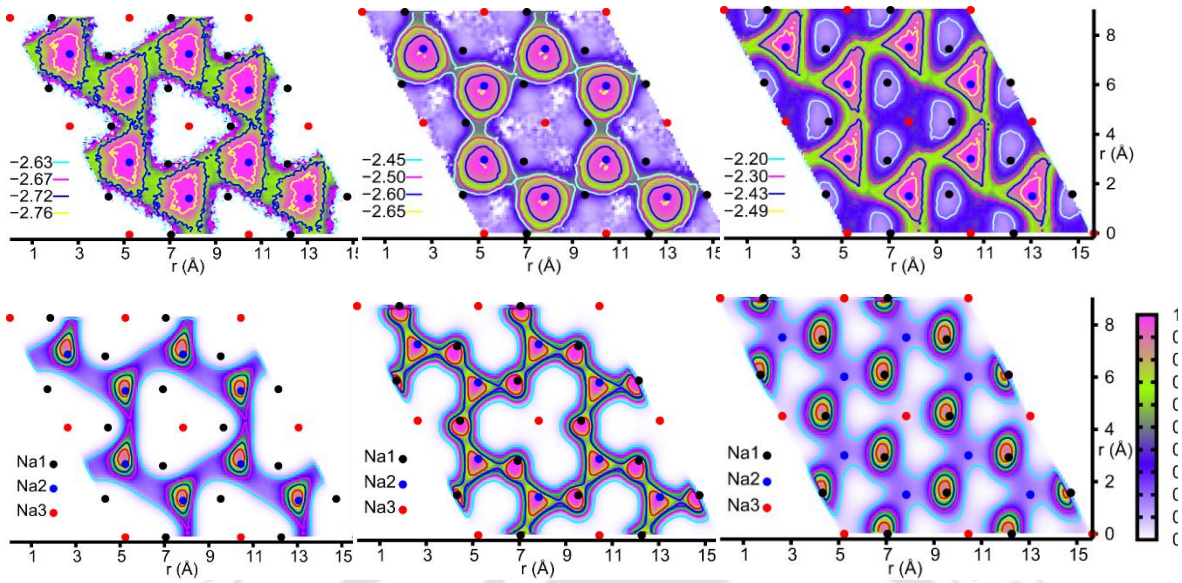

Figure 2. Average potential energy in eV (top panel) and population distributions (bottom panel) of Na^+ at the interlayers for under-loaded (left), normal (middle) and over-loaded (right) interlayers, having respectively 40, 50 and 60 Na^+ ions per interlayer of the simulation cell (containing 5×5×2 unit cells) at 600 K (mapped into 2 × 2).

The nature of ion transport at the interlayers having different number of Na^+ ions (maintaining overall charge neutrality of the system) is examined. It is noted that at low concentrations (having less than 50 Na^+ ions/interlayer of the simulated system, consisting of 5×5×2 unit cells), the Na^+ populations follow the energetic comfort of the framework (figure 2) and migration channels involve direct transfer between lowest energy Na2 sites. With the increase in concentration of Na^+, Na1 sites that are energetically less favorable starts populating, and the migration channels connecting Na2-Na1-Na2 emerge. For higher concentrations (having more than 50 Na^+ ions/interlayer of the simulated system) a reversal of Na^+ population in favor Na1 sites, that are less preferable in terms of energy, but larger in multiplicity is observed. This gradual evolution of the Na^+ population from lower energy to higher energy, while gaining in terms of more accessible sites, reflect a crossover from energetically driven to entropically driven transport of Na^+ ions. Also, the self-diffusion coefficient of Na^+ is predicted to an order of magnitude higher for interlayers with 20% less Na^+ ions relative to the standard composition. This has useful implications in the search for better fast ion conductors.

Chapter 5 *discusses the molecular dynamics investigation of ion transport in* $Li_{1+x}Ti_{2-x}Al_x(PO_4)_3$ *, where* $0 \leq x \leq 0.67$.

A detailed molecular dynamics study on $Li_{1+x}Ti_{2-x}Al_x(PO_4)_3$ (figure 3), a NASICON type fast ion conductor, over the composition range $0 \leq x \leq 0.67$ is carried out. The study employs the previously proposed interatomic potential for $Na_{1+x}Zr_2Si_xP_{3-x}O_{12}$ [33, 34], with necessary re-parameterization. The lattice parameters are found to decrease systematically with the Al^{3+} substitution at the Ti^{4+} in qualitative agreement with experiments. For the optimal substitution (x=0.33) of Al^{3+} the Li^+ conductivity is found to enhance by two-three order of magnitude in good agreement with recent experimental results [21, 22]. The study provides fresh insights on the free energy barriers, migration channels and hopping mechanism of Li^+ in the system.

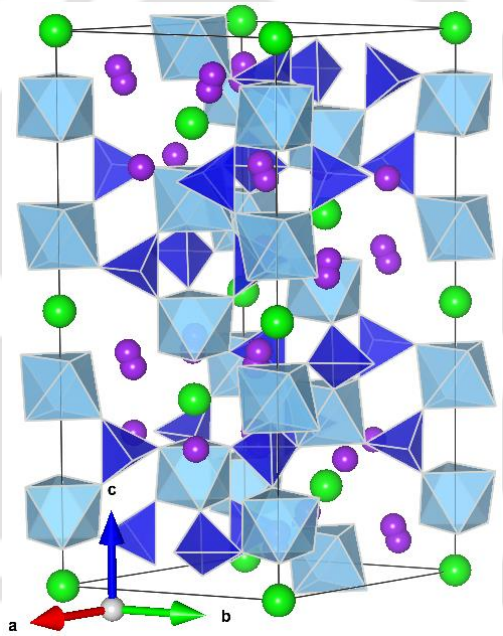

Figure 3. Polyhedral view of one unit cell of $Li_{1+x}Al_xTi_{2-x}(PO_4)_3$ showing $(Ti/Al)O_6$ octahedra (cyan) sharing corners with PO_4 tetrahedra (blue). The interstitial Li sites Li1 (green) and Li2 (purple) are also shown.

Chapter 6 *summarizes the major conclusions of the studies.*

References:

[1] J.B. Goodenough, *J Solid State Electrochem* **16** (2012) 2019.
[2] G. Sahu, Z. Lin, J. Li, Z. Liu, N. Dudney, C. Liang, *Energy Environ. Sci.* **7** (2014) 1053.
[3] K. Takada, *Acta Mater.* **61** (2013) 759.
[4] C. Masquelier, *Nat. Mater.* **10** (2011) 649.
[5] P. Bron, S. Johansson, K. Zick, J.r. Schmedt auf der Günne, S. Dehnen, B. Roling, *J. Am. Chem. Soc.* **135** (2013) 15694.

[6] N. Kamaya, K. Homma, Y. Yamakawa, M. Hirayama, R. Kanno, M. Yonemura, T. Kamiyama, Y. Kato, S. Hama, K. Kawamoto, *Nat. Mater.* **10** (2011) 682.
[7] S. Adams, R.P. Rao, *J. Mater. Chem.* **22** (2012) 7687.
[8] C. Cao, Z.-B. Li, X.-L. Wang, X.-B. Zhao, W.-Q. Han, *Front. Energy Res.* **2** (2014) 25.
[9] M. Barghamadi, A.S. Best, A.I. Bhatt, A.F. Hollenkamp, M. Musameh, R.J. Rees, T. Ruther, *Energy Environ. Sci.* **7** (2014) 3902.
[10] K.B. Hueso, M. Armand, T. Rojo, *Energy Environ. Sci.* **6** (2013) 734.
[11] S.Y. Hong, Y. Kim, Y. Park, A. Choi, N.-S. Choi, K.T. Lee, *Energy Environ. Sci.* **6** (2013) 2067.
[12] V. Palomares, P. Serras, I. Villaluenga, K.B. Hueso, J. Carretero-Gonzalez, T. Rojo, *Energy Environ. Sci.* **5** (2012) 5884.
[13] A. Hayashi, K. Noi, A. Sakuda, M. Tatsumisago, *Nat. Commun.* **3** (2012) 856.
[14] B.L. Ellis, L.F. Nazar, *Curr. Opin. Solid State Mater. Sci.* **16** (2012) 168.
[15] M.D. Slater, D. Kim, E. Lee, C.S. Johnson, *Adv. Funct. Mater.* **23** (2013) 947.
[16] J.W. Fergus, *Solid State Ionics* **227** (2012) 102.
[17] P.P. Kumar, S. Yashonath, *Journal of Chemical Sciences* **118** (2006) 135.
[18] J.a. Meller, *eLS*, John Wiley & Sons, Ltd (2001).
[19] Z. Deng, Y. Mo, S.P. Ong, *NPG Asia Mater* **8** (2016) e254.
[20] M.A. Evstigneeva, V.B. Nalbandyan, A.A. Petrenko, B.S. Medvedev, A.A. Kataev, *Chem. Mater.* **23** (2011) 1174.
[21] K. Arbi, J. Rojo, J. Sanz, *J. Eur. Ceram. Soc.* **27** (2007) 4215.
[22] K. Arbi, M. Hoelzel, A. Kuhn, F. García-Alvarado, J. Sanz, *Inorg. Chem.* **52** (2013) 9290.
[23] J.B. Goodenough, H.P. Hong, J.A. Kafalas, *Mater. Res. Bull.* **11** (1976) 203.
[24] A.R. Rodger, J. Kuwano, A.R. West, *Solid State Ionics* **15** (1985) 185.
[25] H.J. Deiseroth, S.T. Kong, H. Eckert, J. Vannahme, C. Reiner, T. Zaiß, M. Schlosser, *Angew. Chem., Int. Ed.* **47** (2008) 755.
[26] V. Thangadurai, S. Narayanan, D. Pinzaru, *Chem. Soc. Rev.* **43** (2014) 4714.
[27] B. Hafskjold, X. Li, *J. Phys. Condens. Matter* **7** (1995) 2949.
[28] P. Vashishta, A. Rahman, *Phys. Rev. Lett.* **40** (1978) 1337.
[29] M. Parrinello, A. Rahman, P. Vashishta, *Phys. Rev. Lett.* **50** (1983) 1073.
[30] M.A. Zendejas, J.O. Thomas, *Phys. Scr.* **47** (1993) 240.
[31] S. Edvardsson, L. Ojamae, J.O. Thomas, *J. Phys. Condens. Matter* **6** (1994) 1319.
[32] Z. Skotniczny, J. MoScinski, Z. Rycerz, *J. Phys. C: Solid State Phys.* **19** (1986) 4781.
[33] P. Padma Kumar, S. Yashonath, *J. Am. Chem. Soc.* **124** (2002) 3828.
[34] P.P. Kumar, S. Yashonath, *J. Phys. Chem. B* **106** (2002) 7081.

CERTIFICATE

This is certify that the work contained in the dissertation entitled ***"Molecular Dynamics Investigation of Fast Ion Transport in Oxide Frameworks"*** has been carried out by Mr. Kartik Sau at Indian Institute of Technology Guwahati under my supervision. This work has not been submitted elsewhere for the award of any degree.

(Dr. Padma Kumar Padmanabhan)

Thesis Supervisor Date 17th February, 2017

Dedicated to my parents

Acknowledgements

I would like to take this opportunity to express my heartily gratitude to all who was by my side during my PhD study. First of all, I would like to thank my supervisor, Prof. Padma Kumar Padmanabhan. I benefited tremendously from all the discussions we had. His constant encouraging guidance, creative thoughts and suggestions led to every progress during my PhD study. I am grateful and honored to have the opportunity to learn and work with him.

I am thankful to my doctoral committee members, Prof. S. Ghosh, Dr. A. K. Sharma and Dr. S. Paul for their valuable support and suggestions during my research period. I thank the Department of Physics, IIT Guwahati for carrying out of the research work and to provide the friendly environment which always motivates me. I also thank DST, India for the providing supercomputing facility. Big thanks to all of my batchmates, seniors and juniors who were always supportive. I want to specially mention my dear seniors Supriya da, Biswanath da, Souvik da, Poulumi di, Vindhyawasini da, both Bappa da, Pritam da, Obai da, Rashidul da, Sunanda da for giving valuable tips and mental support in my initial Ph.D days. They helped me a lot to develop my skill on Linux system and in more other issues. I wish to thank all of my friends from IITG with whom I played, shared light moments, jokes, arguments over non-academic issues which kept me refreshed and energetic. I would like to thank all of my group members Krishnanjan, Debapriya, Sangkha and Omkar. They have been always very close to my heart. And the rigorous discussions with them on our research field, helped me to clear my concept and gaining more insight into the subject. Special thanks to Dr. Charudatt Kadolkar and my dear friends Tapas, Arnab, Jiarul, Kartick, Ashim, Shankar, Paban, Samit, Debashish, Biplob, Ranganadha, Mahesh, Shanata and juniors Abhijit, Ramiz, Kallol, Sourav, Sudin, Ashish, Anil, Koushik, Pankaj, Bijita, Noor, Srimoy, Sanjib, Pratap, Srikrishna, Kajwal, Indu, Joy, Nawaz, Kishan, Sheuly, Sunayana, Sumiya, Soma, Shefali with them I shared very enjoyable and memorable moments and their mental support in my tough times always kept me refreshed for the next working day.

Last but not least, I would like to give my hearted thanks to my parents and my brother and sister. Their deep love, understanding, constant support, help and encouragement over the years are the great thrust to my study.

Contents

Chapter 1

Introduction

Fast ion conducting solids find numerous technological applications such as in batteries, fuel cells, sensors, memory devices, super-capacitors etc. Fast ion conducting solids having ionic conductivities better than 10^{-3} S/cm and negligible electronic conductivity are also referred to as superionic conductors (SIC) [1, 2]. The history of fast ion conductors dates back to Faraday who observed low electrical resistance in PbF_2 and Ag_2S in the late 1830's, and promptly attributed it to the presence of mobile charge carriers other than electrons [3]. Yattria (Y_2O_3) stabilized zirconia (ZrO_2) and AgI are well known for fast ion conduction since early nineteenth century [4,5]. In 1967 high conducting MAg_4I_5 (where M = Rb, K and NH_4) [4, 5] and Na -β-alumina [6] were reported. Na -β-alumina is one of the earliest fast ion conductors to be discovered with a covalent framework structure. It showed high Ag^+ and Na^+ conductivity of the order of 10^{-2} Scm^{-1} [7, 8] at 298 K. Other classes of matrices to observe high ionic conductivity includes inorganic glasses and polymers (by Otto in 1966) . In a major breakthrough Hong [9] and Goodenough *et al.* [10] reported high alkali ion conduction in a series of skeleton structural solids such as $KSbO_3$, $RbMgAlF_6$, $NaAlSiO_4$, and $Na_{1+x}Zr_2P_{3-x}Si_xO_{12}$ ($0 \leq x \leq 3$) in 1976. Among these solids, NASICONs ($Na_{1+x}Zr_2P_{3-x}Si_xO_{12}$, $0 \leq x \leq 3$) are particularly attractive for their versatility in terms of their structural stability against various ion substitutions, as well as high thermal and chemical stabilities [11]. One of the best studied members of the series $Na_3Zr_2PSi_2O_{12}$ has an ionic conductivity of 0.35 S/cm at 573 K [12, 13], which is comparable to the β-alumina with the additional advantage of 3-dimentional conductivity.

The utility of fast ion conductors in battery applications, such as electrodes or electrolytes, were not recognized until 1960, even though lead-acid batteries were in use since

nineteenth century. Li-ion batteries are now an indispensable household device to power variety of electronic gadgets. The present-day batteries typically use graphite as the positive electrode, and lithium iron phosphate ($LiFePO_4$) or lithium cobalt oxide ($LiCoO_2$), doped with nickel and manganese as the negative electrode. The electrolytes typically are lithium salts, such as, $LiPF_6$, $LiClO_4$ etc., dissolved in organic solvents such as ethylene carbonate or dimethyl carbonate. Use of aqueous electrolytes have several disadvantages such as, electrode corrosion and growth of dendrites in to the liquid phase causing short-circuit, leading to fire or explosion. Other drawbacks include leakage of the electrolyte and effusion of gases etc. These factors are major safety concerns, also limits the operating temperature and durability. Solid electrolytes have several advantages over their liquid counterparts such as, significantly higher energy density, recyclability or longer cell life, better safety and low leakage etc. Thus solid state batteries, that uses solid electrolytes, are envisaged as the next generation batteries. However, use of solid electrolytes would require optimization of several interfacial properties of the battery components as well as their mutual compatibility [14-16]. More importantly solid electrolytes known till date have significantly lower ionic conductivity, at least by an order of magnitude, than their liquid counterparts which limits the efficiency. This calls for the search for better fast ion conducting solids working at ambient temperatures [17]. Li^+ and Na^+ conducting solids are particularly attractive as Li^+ solids could offer light weight and high energy density batteries, while Na^+ based materials would be cost effective for large scale applications [18].

The understanding of microscopic mechanism of ion transport in solids, and the factors influencing conduction are invaluable in the search of potential materials for the battery applications. Due to the revolutionary advances in computer hardware and algorithms, atomistic simulation techniques such as, molecular dynamics, has emerged as a powerful tool in elucidating many microscopic structural and dynamical properties of interest which are generally hard to obtain from experiments [19, 20]. Chapters 3, 4 and 5 of this thesis presents detailed molecular dynamics study on two promising classes of fast ion conductors, namely $Na_2M_2TeO_6$, (where M = Ni, Zn, Co, and Mg) and $Li_{1+x}Ti_{2-x}Al_x(PO_4)_3$, where $0.0 \leq x \leq 0.67$.

Fast ion conduction is realized in several different matrices, such as crystalline, amorphous, polymeric etc. Alkali ions such as, Li^+ and Na^+, oxygen (O^{2-}) and protons (H^+) are the most common mobile species across these diverse range of materials, though some

Ag^+, Cu^{2+} and F^- conducting solids have also been reported. The classification of fast ion conducting solids is a difficult task, given the different possible attributes, such as, the nature of the matrices, mobile species and their potential applications (as in batteries or in fuel cells). However, based on their most striking feature, across these varied possible attributes, a brief overview on the different fast ion conductors is presented below. Later, the section 1.5 is dedicated to a more comprehensive account on the state-of-the-art Li^+/Na^+ conducting solid electrolytes, which is close to the theme of the present thesis. This survey pays special attention atomistic simulation studies of fast ion conductors, and the fresh insights gained from them.

1.1 Oxygen-ion conductors

Oxygen ion (O^{2-}) conductors find applications in solid oxide fuel cells (SOFC) [21-26]. SOFCs are primary energy devices, which convert chemical energy to electricity. It has significantly high conversion efficiency compared to the fossil fuel and is environmental friendly, portable and inexpensive.

SOFC mainly comprises of electrodes (anode and cathode) and electrolyte. The typical electrodes should have both ionic and electronic conductivity and porosity for gaseous diffusion between electrode-electrolyte interface and outer surface of the electrode. While electrolytes have to be pure ionic conductors. The main charge carriers in electrolytes material are anions (O^{2-}) or cations (proton). The fuel (typically H_2 gas, organic fuels, natural gases and hydrocarbons are also possible fuels for fuel cells [27-29]) is filled to the anode compartment. It flows through the porous anode and reacts to the oxide ion (O^{2-}). The typical reactions in an anion conducting fuel cell,

Cathode: $\frac{1}{2}\ O_2 + 2e^- = O^{2-}$

Anode: $H_2 + O^{2-} = H_2O + 2e^-$

The electrons flow through the external circuits and have reached to the cathode. Thus it completes the full circles and by product is the H_2O.

Similarly in fuel cells having cationic (typically H^+) conducting electrolytes the fuel, typically ethanol or methanol, undergoes oxidation reaction at the anode releasing cations and electrons as follows

Cathode: $\frac{1}{2}\ O_2 + 2H^+ + 2e^- = H_2O$

Anode: $H_2 = 2H^+ + 2e$

The proton (H^+) goes through the electrolyte and the electrons through the external circuit. In the cathode absorbed electrons from the external circuit undergo reduction reaction with the oxidant present and typically water is formed as a byproduct.

One of the disadvantages with the current status of SOFC is their high operating temperature (> 750 °C [30]) which demands high thermal, mechanical and chemical stability of the component materials. Thus understanding of the oxygen ion transport in materials [31] for SOFCs [32] is one of the major focus area in the current field of material developments that could reduce the operating temperature of SOFC [23, 33, 34]. The following are some of the oxide ion conducting materials that have been investigated in the recent past.

AO_2-type solids (A = Zr, Ce)

Several conventional oxide-ion conducting AO_2-type materials have the fluorite structure. 'A' forms tetrahedra with oxygen and occupies the face-centered positions of the cubic fluorite structure [35]. ZrO_2 [36] and CeO_2 doped AO_2 structure is very promising for SOFCs. The calcia-stabilized zirconia (CSZ) and yttria-stabilized zirconia (YSZ) exhibit promising oxide-ion conductivity about 700°C [31]. However, at high operating temperature (typically 800–1000 °C) it shows stability issue. In contrast, Sc-doped ZrO_2 shows very high conductivity [37, 38] and again it is expensive. δ-Bi_2O_3 [27, 31, 39] is also very promising as it shows high oxygen vacancies resulting high ionic conductivity (range 0.28–0.34 Scm^{-1} at 1000 °C [37]).

ABO_3-types solids (A = La, Sr; B = Cr, Mn, Fe, Co)

ABO_3-types solids [40-42] generally exhibit mixed conductivity, ionic as well as electronic, and relatively fast oxygen surface exchange kinetics [43-45]. Generally A is a larger cation connected to twelve anions and B is another cation forming a BO_6 octahedra. The BO_6 octahedra shares their corners to form a 3D network following cubic symmetry [35]. The compositions such as, $La_{1-x}Sr_xMnO_3$ (LSM) ($0.0 \leq x \leq 0.7$) has been studied extensively since the sixties [46].

Several theoretical effort have been made to understand the oxygen ion transport in Perovskite structure [47, 48]. Cherry *et al.* [49] and Islam [50] investigated the oxygen ion migration mechanism of $LaBO_3$ (B = Cr, Mn, Fe and Co) employing molecular dynamics

simulations. It is found that the oxygen transport involving hopping of oxygen ions through vacancies via a curved path along the BO_6 octahedral edge. The larger the size of B ion, more is the deviation of the path of oxygen ion from the B site cation. This work reveals the importance of the polarization of the ions which shows that the La^{3+} and B^{3+} ions displace by 0.08 Å and 0.07 Å respectively from the mobile oxygen ion. The study investigates the variation of migration energy with different sizes of A and B site cation (ABO_3). The study has shown that the oxygen ion follows minimum energy path. It is noted that the oxygen diffusion and catalytic activities are highest when $LaBO_3$ is doped with Sr.

In 1996, Islam *et al.* [51] have carried out another MD study on $La_{1-x}Sr_xMnO_{3-\delta}$ and $La_{1-x}Sr_xCoO_{3-\delta}$ (LSCF) to understand structural and transport properties. Considerable oxygen disorder is found to be responsible for high oxygen diffusion. The activation energy for oxygen in $La_{1-x}Sr_xMnO_{3-\delta}$ is more than $La_{1-x}Sr_xCoO_{3-\delta}$. Again the oxygen is observed to migrate to a vacant site by hopping mechanism through the edge of the BO_6 octahedra. The path way of oxygen is through the saddle point positioned at the center of the triangle formed by two A site cation (La) and one B site cation (Mn or Co) [51].

The Sr doped $La_{1-x}Sr_xFeO_{3-\delta}$ (perovskite type structure) is another material having high electronic and ionic conductivities combined with thermal stability [52] which makes it a promising candidate as cathodes for SOFCs. The MD simulation have been employed by Jones and Islam [53] to study the energetic of defects, dopants, nano-clustering and ion migration mechanism in lanthanum ferrite ($LaFeO_3$). The doping of Sr to La site increases the conductivity owing to the low binding energy of dopant-oxygen and enhancement of oxygen vacancy. On the other hand, the study shows that Mg^{2+} substitution would result a tendency to trap migrating oxygen thus decreasing the conductivity. The oxygen migration to the vacant sites takes place along the edges of octahedra. The activation energies for two different oxygen sites are found to be 0.70 eV and 0.84 eV when $LaFeO_3$ is doped with Sr. The cationic diffusion is negligible as compared to oxygen diffusion having their high activation energy [53].

An extension to the above work was carried out by Fisher *et al.* [54] in 2005 where they have carried out MD simulation on two mixed-conducting strontium ferrite materials, $Sr_2Fe_2O_5$ and $Sr_4Fe_6O_{13}$ to examine structures, defect energetics and oxygen migration mechanisms. The structure $Sr_2Fe_2O_5$ consists of alternating layers of perovskite- type

octahedra with FeO_4 tetrahedra and $Sr_4Fe_6O_{13}$ is formed by alternating layers of perovskite-type octahedra with mixed FeO_4/FeO_5 polyhedra. They have calculated migration energy [54] of oxide ion in both cases and it depends on the direction of the migration channels. The equilateral planes of FeO_6 octahedra is appropriate for oxide ion migration for both materials.

Razmkhah *et al.* [55] have recently studied Nd^{3+} or Gd^{3+} stabilized zirconia previously reported by other groups such as Okazaki *et al.* [56], Brinkman *et al.* [57] and Yamamura et al [58]. It is found that pure zirconia does not have appreciable oxygen diffusion due to absence of the vacant oxygen sites. However, Partial incorporation of Nd^{3+} or Gd^{3+} instead of Zr^{4+} generates the oxygen vacancy to maintain charge neutrality. The oxygen vacancy generates the local imbalance of charge which forces the oxygen ion to show long range diffusion. Razmkhah *et al.* [55] have carried out MD simulation for the system $Nd_{2-x}Gd_xZr_2O_7$ ($0.8 \leq x \leq 1.2$). The highest oxygen diffusion is obtained at $x = 0.8$ composition. It is reported that the reduction of the formal charge enhances the oxygen ion diffusion significantly.

1.2 Protonic conductors

Protonic conductors are another important class of fast ion conductors for SOFC applications. Proton conduction was first discovered by Iwahara *et al.* [59] in doped barium and strontium cerates. These material usually stabilizes in perovskite type structure [60]. A good proton conduction is required to have significant oxygen ion vacancies in the structure and dissociative absorption in the surface.

The protonic conductors have several advantages over their oxide ion counterparts such as better conductivity at intermediate temperature range (500 to 700 °C). It can work both in electrolysis mode or fuel cell mode [61]. While there is excess electricity coming from uncertain sources such as hydroelectricity, solar energy or wind energy all such renewable and sustainable source, reverse-SOFCs (r-SOFC) can work in the electrolysis mode (solid oxide electrolysis cells, SOECs) by dissociating water into H_2 as energy storage. This H_2 can be used for load leveling of the power output of these [62].

Cerates and zirconates are also good proton conductors. Many doped cerates and zirconates have been reported showing high protonic conductivity as a function of doping concentration [63]. $SrCeO_3$, $CaZrO_3$ and $BaCeO_3$ show good proton conductivity (of about 10^{-2} Scm^{-1} at 600°C) when doped with trivalent ions [63-71]. Among them $BaCe_{0.80}Y_{0.2}O_{2.9}$

shows one of the best protonic conduction. $BaCO_3$ shows poor chemical stability under 800°C when used in hydrocarbons or SOFCs it reacts with CO_2 and decomposes into barium carbonate and cerium oxide. In comparison with $BaCO_3$, $BaZrO_3$ shows much better chemical stability and shows high intrinsic proton conduction.

1.3 Soft Framework Fast Ion Conductors

Generally heavy metals form a large class of solid electrolytes [72]. The soft framework solid usually show low Debye temperature, low melting point and sharp phase transition (normal to superionic). AgI, Ag_2Se, Ag_2S, CaF_2 and PbF_2 are the examples of the soft framework solids.

AgI, CuI

AgI was one of the early day's material which showed high ionic conductivity. It got attention in past to understand ion conduction mechanism owing to its simple structure. It showed a sudden jump of conductivity at high temperature. The low temperature (below 420 K) phase AgI structure is referred as β-AgI forming FCC structure, while at high temperature, it is known as α-AgI where iodine forms the BCC structure and Ag ions are distributed across the octahedral (6b), tetrahedral (12d) and trigonal (24h) sites as identified by XRD [1, 73-77]. The microscopic understanding was found from MD study carried out by Vashista and Rahman [78] in 1978. The Ag ion mainly hops through the interstitial tetrahedral sites [79-81] resulting long range ionic diffusion. The energetically favorable tetrahedral sites are distributed around 3 to 4 Å attributing liquid like nature of the Ag^+ ions. The Ag ion resides at tetrahedral site roughly for a few picosecond, while it spends one order less in octahedral sites [82]. More recently, *ab initio* MD simulations by Wood and Marzar examined the nature of normal to superionic phase transitions [77].

There exist a number of quasi-binary mixtures AgI-AgX (X=Br, Cl) and AgMI (M = Cu, Cs) stable over a wide range of substitution as well as temperature range. Concentration dependent conductivities have been studied for α-$AgI_{1-x}Cl_x$ [83-87] ($0<x<0.1$) [88] and $Ag_{1-y}Cu_yI$ ($0<y<0.1$). MD simulations also have been carried out for α-$AgI_{1-x}Cl_x$ and $Ag_{1-y}Cu_yI$ for the composition range $0.0 < x, y < 0.25$ [89, 90]. The Ag^+ ion diffusion reduces with the increasing of Cu concentration which is almost immobile and obstructs the Ag^+ ion diffusion. The activation energy is found to be maximum near $y = 0.15$ composition for $Ag_{1-y}Cu_yI$ [89,

91, 92]. The Ag^+ ion is smaller than Cu^+ and Cl^- is smaller than I^-. Thus free volume available for mobile ion diminishes significantly due to Cu^+ or Cl^- doping and it exhibits lower ionic diffusion.

Ag_2X (S, Se, Te), Ag_3SI, Ag_4RbI_5

Silver chalcogenides, general formula Ag_2X (X = Te [93], S [94-96] or Se [97]) show high Ag^+ conductivity. Te and S substituted system possess the BCC structure at high temperature phase near 1200 K whereas Se possess FCC structure. Recent neutron diffraction studies [98, 99] found that at high temperature phase, the Ag^+ ions occupy the tetrahedral and octahedral Ag-sites. Thus Ag^+ ion migration path connects the tetrahedral and octahedral sites for Ag_2Te system. Some other materials Ag_3SI [100] and Ag_4RbI_5 [101] (0.21 S/cm at 293 K [102]) also showed high ionic conductivity. The Ag_3SI structure is very similar to α-AgI structure, where instead of only I^-, the S^{2-} and I^- distribute randomly at BCC-anionic sub lattice above 519 K. Such anionic configuration produces highly disorder arrangement of Ag^+ ions [2].

MF_2 (M=Ca, Ba, Sr, or Pb)

This type of fast ion conductors have received considerable attention in past [103, 104]. The M^{2+} forms FCC structure and F^- ions occupies the octahedral positions. MD simulations has been carried out by Rahman in 1976 to study CaF_2 [105, 106] to understand the basic mechanism of ion hopping. At low temperature, all F^- ions fully occupy the octahedral sites. F^- ion does not show significant diffusion at low temperatures as there is no such vacant site to jump. On the other hand, significant diffusion is observed at high temperature (1600^0 C) where F^- ion occupancy is found to be half [107]. Thus, the new sites for F^- ions to hop was expected. Dixon and Gillan [108-110] confirmed that it happened due to site-site F^- ion correlated jump. Several others interesting theoretical investigations have been made recently in CaF_2 type structure employing atomistic simulations [111, 112].

1.4 Amorphous–glassy electrolytes

Amorphous glassy electrolytes [113] have attracted significant attention owing to its advantages over the crystalline or polycrystalline materials such as absence of the grain

boundary, isotropic conductivity, free volume [114] and versatility of chemical substitutions etc. [115-117].

First high ionic conduction ($\sigma \sim 10^{-2}$ Scm^{-1}) was observed in $AgI\text{-}Ag_2SeO_4$ glass by Kunze [118] in 1973. Since then, a large number of high conducting silicate, phosphate and borate glasses have been synthesized with various mobile species such as Ag^+ [119, 120], Li^+ [121, 122], Cu^+ [123], Na^+ [124], F^- etc. The general formula of glasses is $MX : M_2O : A_xO_y$ where A_xO_y (B_2O_3, MoO_3, WO_3, MoO_3, P_2O_5, SiO_2, As_2O_5 etc.) is glass former and M_2O (Ag_2O, Li_2O, Cu_2O, Na_2O, etc.) is called glass modifier. MX (silver halides, alkali halides, copper halides, etc.) is the dopant salt. Glasses are also made by replacing the oxygen with S or Se in the above compositions.

Angel *et al.* [125, 126] reported inorganic crystalline silicate-$CaSi_2O_5$-containing SiO_5 groups which was quite unusual. It was confirmed by the previously reported [127-129] Si NMR spectrum and it influences on network ion diffusivities. Adam and Swenson [38] have investigated the correlation between local structure of alkali glasses ($Li_xRb_{1-x}PO_3$; $0.0 \leq x \leq 1.0$) and ionic conductivity employing bond valance analysis. It was found that the immobile Rb^+ ions mainly block the diffusion path of the Li^+ ions. Very similar behavior is also observed in the system $Ag_xNa_{1-x}PO_3$ ($0.0 \leq x \leq 1.0$) [130], $35[xLi_2O.(1 - x)K_2O]65SiO_2$ ($0.0 \leq x \leq 1.0$) [131, 132].

1.5 Covalent Framework Fast Ion conductors

Solid electrolytes with covalent bonded, interconnected polyhedral structures form another class of materials. They usually have very high Debye temperature, high thermal and chemical stability and high melting points offering high operating temperatures for practical applications.

Lithium Garnets

Garnet type materials, with the general chemical formula $A_3B_2(XO_4)_3$ (A = Ca, Mg, Y, La or rare earth; B = Al, Fe, Ga, Ge, Mn, Ni or V; X = Si, Ge, Al), promise high thermal stability, high electrochemical window as well as high ionic conductivity [133]. They generally stabilize in the cubic phase with the space group $Ia\bar{3}d$. The A, B and X sites are respectively 8-fold (anti-prismatic), 6-fold (octahedral) and 4-fold (tetrahedral) coordinated to oxygen.

Lithium conducting garnets, $Li_3Ln_3Te_2O_{12}$ (Ln = Y, Pr, Nd, Sm–Lu), typically contains 5-7 formula units where lithium ions occupies the 4-fold coordinated tetrahedral sites. Since the original work by Murugan *et al.* [133], it has attracted numerous experimental and theoretical studies. It is observed that at low lithium content, $Li_3Ln_3Te_2O_{12}$, where Li^+ ions are tetrahedrally coordinated does not show significant ionic conductivity ($\sigma \approx 10^{-5}$ S/cm) [134, 135]. However, higher ionic conductivity has been achieved for Li-rich, "stuffed garnets", such as, $Li_5La_3M_2O_{12}$ (M = Nb, Ta and Sb), $Li_6ALa_2M_2O_{12}$ (A = Mg, Ca, Sr and Ba; M = Nb and Ta), and $Li_7La_3M_2O_{12}$ (M = Zr and Sn) [136] where Li ions occupy the tetrahedral as well as octahedral interstitial sites partially. Generally the conductivity value increases with higher Li content. The conductivity enhances by 9 orders of magnitude from $Li_3Ln_3Te_2O_{12}$ to $Li_7La_3M_2O_{12}$ due to significant Li^+ occupancy switches from tetrahedral to octahedral sites [134, 135].

The high conducting cubic garnet $Li_7La_3Zr_2O_{12}$ (LLZO) was reported by Murgun *et al.* [133] and later on the tetragonal phase was detected at lower temperature by Awaka *et al.* [137]. The cubic phase shows two orders of magnitude higher conductivity than the tetragonal phase [138]. Several computational studies have been carried out to explain such behavior [139, 140]. Low temperature tetragonal phase exhibits synchronous collective Li^+ ion hopping causes high activation energy barrier. While in cubic LLZO, the Li^+ finds unoccupied sites resulting uncorrelated Li^+ motion costs less activation energy. Hu *et al.* [141] and others [142-144] have reported that highervalent ion (Al^{3+}) substitution at Li sublatice improve the stability of cubic garnet of nominal composition in $Li_7La_3Zr_2O_{12}$. The Al^{3+} substitution genrates more Li sites which leads more entropy and reduces the free energy. Several studies have been also carried out to improve its conductivity further. The aliovalent substitutions (e.g. Ta^{5+}) at Zr sites also enhances the ionic conductivity [145, 146]. An order of magnitude of conductivity is enhanced from $Li_5La_3Ta_2O_{12}$ to $Li_6BaLa_2Ta_2O_{12}$ [147-149] where the Li ions are occupied in tetrahedral as well as octahedral sites [147, 150]. Thus garnet type materials are found to be promising fast ion conductors owing to its wide range of substitutions and stability of its skeleton structure.

Lithium Argyrodites

Lithium argyrodite Li_6PS_5X (with X = Cl, Br, or I) is another class of fast ion conducting materials synthesized and characterized recently by Deiseroth *et al.* [151]. Lithium argyrodites generally stabilize in the cubic structure (space group F-43m) [152-157] with phosphorus atoms located at the tetrahedral sites (48h and 24g sites) forming the tetrahedra with S and halides are generally located at the corner of the cell. Several interstitial sites are available for lithium around the halide ions facilitating high conductivity (10^{-2} – 10^{-3} S/cm at room temperature) with low activation energies of about 0.2 to 0.3 eV [158]. The Li_6PS_5Cl and Li_6PS_5Br show high conductivity compared to the iodide compositions ($\sigma \approx 10^{-7}$ S/cm) owing to S^{2-}/X^- disorder which does not observe in iodide case due to its large size. The O^{2-} substitution by replacing S^{2-} decreases the conductivity by several order of magnitude which was also observed in thio-LISICON structure [135].

M_3PX_4 (M = Li, Na, K and X= S, O or Se)

M_3PX_4, where M = Li, Na, K and X = S, O or Se, is another class of fast ion conducting materials comprising of isolated PX_4 tetrahedra arranged to form cubic structure. The mobile M-ions occupy the tetrahedral voids in the cubic structure with space group I-43m. They generally undergo normal to superionic transition (tetragonal to cubic) and cubic phase is stable at room temperature for M_3PO_4 (M = Li, Na and K). M_3PO_4 shows the conductivity value of the order of 10^{-3} S/cm at 873 K [159]. In contrast, Na_3PS_4 and Na_3PSe_4 shows conductivity value 0.46×10^{-3} and 0.10×10^{-3} S/cm respectively at room temperature [160, 161]. Based on experimental studies, two transport mechanisms have been proposed [2, 162-165] 1) percolation mechanism and 2) paddle wheel mechanism. According to the paddle wheel mechanism, the rotating PX_4 tetrahedron pushes Na^+ ions through the interstitial sodium lattice sites. MD studies also have supported such tetrahedral rotations and correlated sodium ion motions. However, no evidence for these mechanism was found in neutron diffraction studies [162, 164, 166]. Yin *et al.* [167] have studied these materials extensively with the help of computer simulation and it is found that both tetrahedral and octahedral coordinated Na-sites ions contribute to produce high sodium conductivity. Their study supports the microscopic percolation mechanism for Na^+ ion diffusion.

Yin *et al.* have carried out MD simulations [171] on many other similar solids, such as, K_2SeO_4, K_2SO_4, Ca_2SiO_4, $NaClO_4$, KNO_3, $NaNO_2$, $NaMgF_3$ etc. [167-170]. It reproduces the structural phase transition in agreement with experimental results. Microscopic insights on sodium ion motion is described in detailed and concluded that sodium ions equally prefer to occupy tetrahedral as well as octahedral interstitial sites facilitating high ionic conductivity. The sodium ion follows the percolation mechanism according to their microscopic findings. However, previously reported preferable site was octahedral Na sites MD studied by Harrison and co-workers [167, 171].

Recently, cubic Na_3PS_4 and Na_3PSe_4 are gaining attention for their high Na^+ conductivity. Selenium is relatively less explored chemical species for the fast ion conductors compared to the oxide and sulfide [172, 173]. Recently Bo *et al.* [161] have carried out a combined experimental as well as *ab initio* MD study directed to the coast effective materials. They have found almost identical hopping energy barrier of the Na^+ diffusion for both Se and S substituted systems. Their study provided valuable guide lines for improving Na^+ conductivity in these systems. It is proposed that introducing 2.1% Na ion vacancy would reduce the activation energy to 0.11 eV resulting conductivity to enhance by nearly two orders of magnitude to about 28.9×10^{-3} S/cm at room temperature.

Subsequently, Zhu *et al.* [174] have studied *ab initio* MD on the system Na_3PS_4 [175, 176]. Na^+ ions migrate through the interstitial Na1 (6b) and Na2 (12d) sites and it mostly prefers Na1 sites. Aliovalent substitution i.e. $Na_{3+x}M_xP_{1-x}S_4$ with M = Si, Ge, and Sn enhances the sodium ion conductivity significantly at room temperature. The excess Na^+ ions bound to displace the Na^+ ions from their usual lattice sites i.e. Na1 and Na2 which helps to form shallow energy landscape and it produces cooperative Na^+ ion motion resulting high conductivity. The maximum Na^+ conductivity of 1.66×10^{-3} S/cm is achieved with Si/P ratio 6:94 is with the reported experimental conductivity of 0.74×10^{-3} S/cm by Tanibata *et al.* [177, 178].

LISICONs

Recently Kamaya *et al.* [179] have synthesized a material $Li_{10}GeP_2S_{12}$ (LGPS) which exhibits one of the best Li^+ ion conductivity (10^{-2} S/cm) at room temperature. This class of materials known as LISICON (LIthium Super Ionic CONductors) with space group $P4_2/nmc$ consisting

of $(Ge_{0.5}P_{0.5})S_4$ tetrahedra, PS_4 tetrahedra and Li^+ ions are occupied tetrahedral, and octahedral sites. The edge sharing polyhedra allow the Li^+ ion movement along c-axis and exhibits 1D Li^+ diffusion. Interestingly, Li^+ ions are highly localized at the octahedral Li sites and do not contribute to Li^+ ion diffusion. It provides highly anisotropic conduction of the Li^+ ion through partially occupied tetrahedral Li-sites and exhibits low activation energy (0.24 eV).

Mo *et al.* [180] have reported the 1D lithium ion diffusion along c-axis from their *ab initio* MD. The MD simulations have been carried out by Adams and Rao [181] where the microscopic of the Li ion dynamics is studied. The Li^+ ions are found to be distributed along the c direction among several interstitial Li sites. The study indicates the possibility of the rotation of PS_4^{3-}/GeS_4^{2-} which helps the Li^+ dynamics through paddle-wheel mechanism [182]. Bron *et al.* [183] have synthesized $Li_{10}SnP_2S_{12}$ where costly Ge is replaced by Sn. It shows comparable ionic conductivity and negligible electronic conductivity. It has attracted considerable attention as it is cost effective. Recently, Khun *et al.* have reported $Li_{11}Si_2PS_{12}$ which exhibits higher conductivity than LGPS at room temperature with an activation energy of about 0.19 eV [184].

β-alumina

Discovery of β-alumina by Yao and Kummer [6] is an important breakthrough in the field of solid state fast ion conductors (FIC) in the mid-twentieth century which unfolds a new class of superionic conductors. It has an ionic conductivity of 1.4×10^{-2} Scm^{-1} at 300 K which is comparable to typical liquid electrolytes. A large number of theoretical [185-188] and experimental [189-192] works have been dedicated to understand the transport properties. The general formula $M_2O.xAl_2O_3$ (where M = Li, Na, Ag, K and Rb) comprises of compact layer of spinel blocks, formed by Al^{3+} with tetrahedrally and octahedrally coordinated oxygens. Conduction planes are sandwiched between two such spinel blocks altogether forming a 3D hexagonal structure ($P6_3/mcm$ space group). Three different Na-sites are found anti-Beevers-Ross (aBR), Beevers-Ross (BR) and mid Oxygen (mO) through which Na ions can hop through attributing high diffusion [193, 194]. The mobile Na-ions are mainly occupy the aBR and mO sites as reported by Collin et al [195].

A systematic study have been carried out by Kummer for different monovalent (Li^+, Na^+, Ag^+, K^+, Rb^+ etc.) [196] counterpart. The study reveals that the ionic radius between Na^+

and Ag^+ among the mentioned series is suitable for the ion diffusion in β-alumina skeleton framework. Kumar and Yashonath [197] have observed this phenomenon in NASICON type structure where optimal ionic radius of mobile cation produces best ionic conductivity for fixed skeleton framework. The mobile Ag^+ ions in conducting plane are distributed over BR and aBR sites with asymmetric large thermal amplitude. Their further studies [198] have concluded that the Ag-Ag repulsion changes the dynamics of Ag from random hopping to the cooperative motion. Higher Ag-Ag repulsion makes the Ag ion distribution into small domains belonging to BR and aBR sites and exhibits low conductivity.

NASICON

The discovery of NASICON (acronym for Na SuperIonic CONductor) by Hong [9] and Goodenough *et al.* [10] was a major breakthrough in the search for fast ion conductors. It is a very promising candidate owing to its high 3D ionic conductivity and high thermal and chemical stability as well as it provides a wide range of substitution window. It finds several other applications such as nuclear waste disposal [199, 200], low thermal expansion ceramics [200-206] and sensor etc.

The general formula of the NASICON is $Na_{1+x}Zr_2Si_xP_{3-x}O_{12}$ ($0.0 \leq x \leq 3.0$) and it consists of ZrO_6 corner shared octahedra and $(Si/P)O_4$ tetrahedra connecting to form a three dimensional rhombohedral unit possessing R3-c symmetry. The higher oxidation states of Zr^{4+} and Si^{4+}/P^{5+} make the framework very rigid which allow wide range of mobile ion substitutions as well as improves the thermal stability (high melting point >1650 ^{0}C). There are Na1 (6b) and Na2 (18e) interstitial sites where Na1 is sandwiched between two ZrO_6 octahedra along z-axis and Na2 site connects two such Na1 sites. Na1 is a center of six coordinates oxygen octahedra ($Na1O_6$) and Na2 sites are irregular eight coordinated oxygens. The unit cell consists of six formula units. There exist one more site so called mid-Na (36f) and such six mid-Na are located in a circle parallel to the ab-plane surrounded by each Na1 site. These 3D distributed sites help Na ion to form 3D migration path.

The material $Na_{1+x}Zr_2Si_xP_{3-x}O_{12}$ ($0.0 \leq x \leq 3.0$) shows excellent ionic conductivity at $x = 2.0$ [207, 208]. Henceforth very few theoretical studies have been made to understand the ionic motion in NASICON [209-212]. Their model reproduced the experimental structural and dynamical properties in agreement with experimental results. The highest conductivity

was found near the composition $x = 2$ and their investigation provided the valuable microscopic insights. For $x = 0.0$ composition, Na1 sites are fully occupied and produces low diffusivity [213]. The Na2 and mid-Na sites are getting populated with $x > 0.0$ and the availability of the Na2 and mid-Na sites enhances the conductivity. The free energy profiles along the Na^+ migration path have been also shown and it is pointing toward the significant entropic contributions [214].

Roy and Kumar [215] have recently studied the influence of Si/P ordering on the conductivity. There are six basal planes perpendicular to *c*-axis and each plane consists of three tetrahedra per unit cell. Three different orders are studied. First, two Si^{4+} and one P^{5+} in each plane are placed. Second, two planes made of SiO_4 tetrahedra are sandwiched by one plane made of PO_4 tetrahedra and third, the random order (Si^{4+} and P^{5+} placed randomly at the Si/P sites). The conductivity varies by one order of magnitude depending on the Si/P order in the structure. The study suggests the significance of the framework cationic order in conductivity with aliovalent substitutions. Experimentally, such orders could be possible depending on the sintering temperature and duration. This possibly explains the large variance in the reported ionic conductivities by different groups.

Roy and Kumar have also studied the system for $x = 1.0$ i.e. $Na_2Zr_2SiP_2O_{12}$ [127] where anisotropic 2D diffusion is obtained for certain arrangement of the Si and P. They have tried with two different orders on the basal plane. One is two P^{5+} rich planes sandwiching by one Si^{4+} rich plane parallel to the *ab*-plane and other order where each plane contains one Si^{4+}. The Later order shows the usual isotropic diffusion and former order exhibits an-isotropic diffusion even though the gross diffusivity does not differ significantly. Population profile along z-axis including Si and P positions for the two different orders reveal that the high P-P repulsion breaks continuation of the Na^+ ions motion.

It is very important to understand the ionic motion inside the solid in terms of the connecting channels and existing bottlenecks. Essentially two types of conduction channels have been investigated; one is connecting Na1 and neighboring Na2 sites and other one connecting Na2 to Na2. In $Na_4Zr_2Si_3O_{12}$ system, bottleneck exists in trapezoidal form with oxygens sitting at the corners reported by Tran Qui *et al.* [216] and it is wider than triangular bottleneck.

Ionic conductivity is strongly correlated on the framework skeleton of the NASICON. Typically ionic diffusion increases with larger bottleneck size formed by the skeleton NASICON framework. Martínez-Juárez *et al.* [217] reported such behaviors in the system $LiM_2(PO_4)_3$ where M = Ge, Ti, Sn, Hf and Zr etc. with respective ionic radius $\sigma_{Ge} < \sigma_{Ti} < \sigma_{Sn} < \sigma_{Hf} < \sigma_{Zr}$. Hence the bottleneck radius formed by the skeleton framework systematically increases with higher size of the cationic substitutions. Thus higher diffusivity of the mobile Li^+ ions is found. The activation energy is also systematically reduces with the higher bottleneck radius. On the contrary, $Na_3Zr_2Si_2P_{12}$ system exhibits highest conductivity whereas $Li_3Zr_2Si_2P_{12}$ shows very low ionic conductivity. It means that the larger tunnel constructed by $(Zr_2Si_2P_{12})^{3-}$ skeleton is not suitable for Li^+ ion conduction [218]. Kumar and Yashonath have made a theoretical study on the system $MZr_2(PO_4)_3$ system with varying mobile ion (M) radius and it produces highest conductivity for the optimal radius of the mobile ion (0.59Å) and the mean square force is minimum near this ionic radius [197].

Chapter 5 discusses molecular dynamics study of $Li_{1+x}Al_xTi_{2-x}P_3O_{12}$ ($0.0 \leq x \leq 0.67$), a promising NASICON-type fast ion conductor.

$Na_2M_2TeO_6$

There are several telluride compound which shows very high ionic conductivity and negligible electronic conductivity. It would be a very promising candidate for the electrolyte. Evstigneeva *et al.* [219] have synthesized a family of fast ion conductors $Na_2M_2TeO_6$, where M=Ni, Zn, Co or Mg. Ni composition exhibits highest ionic conductivity among the series.

More detailed description of the structure and conductivity of these systems are given in Chapters 3 and 4.

Bibliography

[1] M. Aniya, *Physics Procedia* **44** (2013) 25.
[2] S. Hull, *Rep. Prog. Phys.* **67** (2004) 1233.
[3] B. Xu, D. Qian, Z. Wang, Y.S. Meng, *Materials Science and Engineering R: Reports* **73** (2012) 51.
[4] B.B. Owens, G.R. Argue, *Science* **157** (1967) 308.
[5] J.N. Bradley, P.D. Greene, *Trans. Faraday Soc.* **63** (1967) 424.
[6] Y.F.Y. Yao, J.T. Kummer, *J. Inorg. Nucl. Chem.* **29** (1967) 2453.
[7] R.C. Agrawal, R.K. Gupta, *J. Mater. Sci.* **34** (1999) 1131.
[8] J.L. Briant, G.C. Farrington, *J. Solid State Chem.* **33** (1980) 385.
[9] H.P. Hong, *Mater. Res. Bull.* **11** (1976) 173.
[10] J.B. Goodenough, H.P. Hong, J.A. Kafalas, *Mater. Res. Bull.* **11** (1976) 203.
[11] N. Anantharamulu, K. Koteswara Rao, G. Rambabu, B. Vijaya Kumar, V. Radha, M. Vithal, *J. Mater. Sci.* **46** (2011) 2821.
[12] J.P. Boilot, G. Collin, P. Colomban, *J. Solid State Chem.* **73** (1988) 160.
[13] H.Y.P. Hong, *Mater. Res. Bull.* **11** (1976) 173.
[14] V. Etacheri, R. Marom, R. Elazari, G. Salitra, D. Aurbach, *Energ Environ Sci* **4** (2011) 3243.
[15] H. Pan, Y.S. Hu, L. Chen, *Energ Environ Sci* **6** (2013) 2338.
[16] E. Kendrick, P. Slater, *Annu. Rep. Prog. Chem., Sect. A: Inorg. Chem.* **108** (2012) 424.
[17] J.W. Fergus, *Solid State Ionics* **227** (2012) 102.
[18] K.B. Hueso, M. Armand, T. Rojo, *Energ Environ Sci* **6** (2013) 734.
[19] C. Catlow, Z. Guo, M. Miskufova, S. Shevlin, A. Smith, A. Sokol, A. Walsh, D. Wilson, S. Woodley, *Phil. Trans. R. Soc. A* **368** (2010) 3379.
[20] Y. Mo, S.P. Ong, G. Ceder, *Chem. Mater.* **24** (2012) 15.
[21] D.J.L. Brett, A. Atkinson, N.P. Brandon, S.J. Skinner, *Chemical Society reviews* **37** (2008) 1568.
[22] B.C.H. Steele, *Solid State Ionics* **134** (2000) 3.
[23] T. Hibino, A. Hashimoto, T. Inoue, J.I. Tokuno, S.I. Yoshida, M. Sano, *Science* **288** (2000) 2031.
[24] Z. Shao, S.M. Haile, J. Ahn, P.D. Ronney, Z. Zhan, S.A. Barnett, *Nature* **435** (2005) 795.
[25] Y. Wang, W.D. Richards, S.P. Ong, L.J. Miara, J.C. Kim, Y. Mo, G. Ceder, *Nat Mater* **14** (2015) 1026.
[26] S.C. Singhal, *Solid State Ionics* **152-153** (2002) 405.
[27] S.M. Haile, *Acta Mater.* **51** (2003) 5981.
[28] D.J. Brett, A. Atkinson, N.P. Brandon, S.J. Skinner, *Chem. Soc. Rev.* **37** (2008) 1568.
[29] A.J. Jacobson, *Chem. Mater.* **22** (2010) 660.
[30] P. Knauth, *Solid State Ionics* **180** (2009) 911.
[31] B.C.H. Steele, A. Heinzel, *Nature* **414** (2001) 345.
[32] K.C. Lau, B.I. Dunlap, *InTech* **1** (2012).
[33] K.D. Kreuer, *Solid State Ionics* **97** (1997) 1.
[34] K.D. Kreuer, Proton-Conducting Oxides, *Annu. Rev. Mater. Res.* (2003), p.333.
[35] L. Malavasi, C.A. Fisher, M.S. Islam, *Chem. Soc. Rev.* **39** (2010) 4370.

[36] C.S. Tedmon, Jr., H.S. Spacil, S.P. Mitoff, *J. Electrochem. Soc.* **116** (1969) 1170.
[37] S.P.S. Badwal, F.T. Ciacchi, D. Milosevic, *Solid State Ionics* **136–137** (2000) 91.
[38] S. Sarat, N. Sammes, A. Smirnova, *J Power Sources* **160** (2006) 892.
[39] J.B. Goodenough, *Annu. Rev. Mater. Res.* **33** (2003) 91.
[40] R.W. Balluffi, S.M. Allen, W.C. Carter, *Kinetics of Materials* (2005).
[41] K.R. Kendall, C. Navas, J.K. Thomas, H.C. Zur Loye, *Chem. Mater.* **8** (1996) 642.
[42] H. Jonsson, G. Mills, K.W. Jacobsen, *Classical and Quantum Dynamics in Condensed Phase Simulations-Proceedings of the International School of Physics* (1998).
[43] P. Knauth, H.L. Tuller, *J. Am. Ceram. Soc.* **85** (2002) 1654.
[44] A. Hammou, J. Guindet, *Solid Oxide Fuel Cells* 407.
[45] H.J.M. Bouwmeester, A.J. Burggraaf, *Dense Ceramic Membranes for Oxygen Separation* (1997) 481.
[46] N. Kamaya, K. Homma, Y. Yamakawa, M. Hirayama, R. Kanno, M. Yonemura, T. Kamiyama, Y. Kato, S. Hama, K. Kawamoto, A. Mitsui, *Nat Mater* **10** (2011) 682.
[47] M.E. Glicksman, *Diffusion in Solids: Field Theory, Solid-State Principles, and Applications* (2000).
[48] G.H. Vineyard, *J Phys Chem Solids* **3** (1957) 121.
[49] M. Cherry, M.S. Islam, C.R.A. Catlow, *J. Solid State Chem.* **118** (1995) 125.
[50] M.S. Islam, *Solid State Ionics* **154-155** (2002) 75.
[51] M.S. Islam, M. Cherry, C.R.A. Catlow, *J. Solid State Chem.* **124** (1996) 230.
[52] J.B. Goodenough, H.Y.P. Hong, J.A. Kafalas, *Mater Res Bull* **11** (1976) 203.
[53] A. Jones, M.S. Islam, *J. Phys. Chem. C* **112** (2008) 4455.
[54] C.A.J. Fisher, M.S. Islam, *J. Mater. Chem.* **15** (2005) 3200.
[55] M. Razmkhah, M.H. Mosavian, F. Moosavi, *Int. J. Hydrogen Energy* **39** (2014) 8437.
[56] H. Okazaki, H. Suzuki, K. Ihata, *Phys. Lett. A* **188** (1994) 291.
[57] H.W. Brinkman, W.J. Briels, H. Verweij, *Chem. Phys. Lett.* **247** (1995) 386.
[58] Y. Yamamura, S. Kawasaki, H. Sakai, *Solid State Ionics* **126** (1999) 181.
[59] H. Iwahara, T. Esaka, H. Uchida, N. Maeda, *Solid State Ionics* **3-4** (1981) 359.
[60] K.D. Kreuer, *Chem. Mater.* **8** (1996) 610.
[61] L. Bi, S. Boulfrad, E. Traversa, *Solid State Ionics* **275** (2015) 101.
[62] M.A. Laguna-Bercero, *J. Power Sources* **203** (2012) 4.
[63] H. Iwahara, T. Yajima, T. Hibino, H. Ushida, *J. Electrochem. Soc.* **140** (1993) 1687.
[64] D.A. Stevenson, N. Jiang, R.M. Buchanan, F.E.G. Henn, *Solid State Ionics* **62** (1993) 279.
[65] E. Fabbri, A. D'Epifanio, E. Di Bartolomeo, S. Licoccia, E. Traversa, *Solid State Ionics* **179** (2008) 558.
[66] K. Katahira, Y. Kohchi, T. Shimura, H. Iwahara, *Solid State Ionics* **138** (2000) 91.
[67] G. Ma, T. Shimura, H. Iwahara, *Solid State Ionics* **110** (1998) 103.
[68] M. Oishi, S. Akoshima, K. Yashiro, K. Sato, J. Mizusaki, T. Kawada, *Solid State Ionics* **179** (2008) 2240.
[69] T. Hibino, A. Hashimoto, M. Suzuki, M. Sano, *J. Phys. Chem. B* **105** (2001) 11399.
[70] J. Melnik, J. Luo, K.T. Chuang, A.R. Sanger, *The Open Energy and Fuels Journal* **1** (2008) 7.
[71] H. Matsumoto, Y. Kawasaki, N. Ito, M. Enoki, T. Ishihara, *Electrochem. Solid-State Lett.* **10** (2007) B77.

[72] B.M. De Boisse, D. Carlier, M. Guignard, C. Delmas, *J Electrochem Soc* **160** (2013) A569.
[73] S. Hoshino, *J. Phys. Soc. Jpn.* **9** (1954) 295.
[74] S. Chandra, *Superionic Solids: Principles and Applications* (1981).
[75] K. Funke, *Prog. Solid State Chem.* **11** (1976) 345.
[76] D.A. Keen, S. Hull, A.C. Barnes, P. Berastegui, W.A. Crichton, P.A. Madden, M.G. Tucker, M. Wilson, *Phys. Rev. B* **68** (2003) 141171.
[77] C. Delmas, C. Fouassier, P. Hagenmuller, *Physica B+C* **99** (1980) 81.
[78] P. Vashishta, A. Rahman, *Phys. Rev. Lett.* **40** (1978) 1337.
[79] A. Yoshiasa, H. Maeda, T. Ishii, K. Koto, *Solid State Ionics* **40** (1990) 341.
[80] W. Bührer, W. Hälg, *Helv. Phys. Acta* **47** (1974).
[81] A.F. Wright, B.E.F. Fender, *J. Phys. C: Solid State Phys.* **10** (1977) 2261.
[82] A. Ivanov-Shitz, *Crystallogr. Rep.* **52** (2007) 302.
[83] J.C. Bazán, J.A. Schmidt, *J. Appl. Electrochem.* **6** (1976) 411.
[84] J.A. Schmidt, R.E. Fornari, J.C. Bazán, *Electrochim. Acta* **24** (1979) 1131.
[85] M. Kusakabe, Y. Shirakawa, S. Tamaki, Y. Ito, *J. Phys. Soc. Jpn.* **64** (1995) 170.
[86] P.S. Kumar, P. Balaya, P.S. Goyal, C.S. Sunandana, *J. Phys. Chem. Solids* **64** (2003) 961.
[87] S. Ihara, K. Suzuki, *Physica Status Solidi (B) Basic Research* **131** (1985) 97.
[88] J. Nölting, *Ber. Bunsenges. Phys. Chem.* **68** (1964).
[89] A.K. Ivanov-Schitz, B.J. Mazniker, E.S. Povolotskaya, *Solid State Ionics* **159** (2003) 63.
[90] A. Ivanov-Schitz, S. Savvin, G. Mazo, *Crystallogr. Rep.* **54** (2009) 292.
[91] A.K. Ivanov-Shitz, B.Y. Mazniker, E.S. Povolotskaya, *Kristallografiya* **46** (2001) 336.
[92] A.K. Ivanov-Shitz, B.Y. Mazniker, E.S. Povolotskaya, *Kristallografiya* **47** (2002) 125.
[93] F. Tachibana, M. Kobayashi, H. Okazaki, *Solid State Ionics* **28-30** (1988) 41.
[94] J.R. Ray, P. Vashishta, *J. Chem. Phys.* **90** (1989) 6580.
[95] S. Ihara, K. Suzuki, *J. Phys. Soc. Jpn.* **53** (1984) 3081.
[96] P. Vashishtat, I. Ebbsjo, R. Dejus, K. Skold, *J. Phys. C: Solid State Phys.* **18** (1985) L291.
[97] J.P. Rino, Y.M.M. Hornos, G.A. Antonio, I. Ebbsjö, R.K. Kalia, P. Vashishta, *J. Chem. Phys.* **89** (1988) 7542.
[98] D.A. Keen, S. Hull, *Journal of Physics Condensed Matter* **10** (1998) 8217.
[99] S. Hull, D.A. Keen, P. Berastegui, *J. Phys. C: Cond. Matt.* **14** (2002) 13579.
[100] B. Reuter, K. Hardel, *Z. Anorg. Allg. Chem.* **340** (1965).
[101] T. Takeuchi, *Phys. Stat. Sol. (B)* **147** (1988).
[102] D.O. Raleigh, *J. Appl. Phys.* **41** (1970) 1876.
[103] H.Y.P. Hong, *Mater Res Bull* **11** (1976) 173.
[104] Y. Mo, S.P. Ong, G. Ceder, *Chem. Mater.* **26** (2014) 5208.
[105] A. Rahman, *J. Chem. Phys.* **65** (1976) 4845.
[106] G. Jacucci, A. Rahman, *J. Chem. Phys.* **69** (1978) 4117.
[107] M.J. Gillan, *J. Phys. C: Solid State Phys.* **19** (1986) 3517.
[108] M. Dixon, M.J. Gillan, *J. Phys. (Paris)* **41** (1980) C6.
[109] M.J. Gillan, *Physica B+C* **131** (1985) 157.
[110] C. Tubandt, E. Lorenz, *Z. Phys. Chem.* **87** (1914).
[111] A. Annamareddy, J. Eapen, *J. Chem. Phys.* **143** (2015).

[112] V.A. Annamareddy, P.K. Nandi, X. Mei, J. Eapen, *Phys. Rev. E: Stat. Nonlinear Soft Matter Phys.* **89** (2014).
[113] A. Pedone, G. Malavasi, M.C. Menziani, A.N. Cormack, U. Segre, *J Phys Chem B* **110** (2006) 11780.
[114] J. Swenson, L. Börjesson, *Phys. Rev. Lett.* **77** (1996) 3569.
[115] J. Kawamura, R. Asayama, N. Kuwata, O. Kamishima, *Phys. Solid State Ionics* (2006) 193.
[116] P. Boolchand, W. Bresser, *Nature* **410** (2001) 1070.
[117] A. Chandra, A. Bhatt, A. Chandra, *J. Mater. Sci. Technol.* **29** (2013) 193.
[118] D. Kunze, W. Van Gool, *North Holland, Amsterdam* (1973) 495.
[119] T. Minami, *J. Non-Cryst. Solids* **56** (1983) 15.
[120] J. Kawamura, M. Shimoji, *Mater. Chem. Phys.* **23** (1989) 99.
[121] J. Kennedy, *Mater. Chem. Phys.* **23** (1989) 29.
[122] A. Pradel, M. Ribes, *Mater. Chem. Phys.* **23** (1989) 121.
[123] C. Liu, C. Angell, *Solid State Ionics* **13** (1984) 105.
[124] C. Hunter, M. Ingram, *Solid State Ionics* **14** (1984) 31.
[125] R.J. Angel, N.L. Ross, F. Seifert, T.F. Fliervoet, *Nature* **384** (1996) 441.
[126] R. Angel, *Am Mineral* **82** (1997) 836.
[127] S. Roy, P.P. Kumar, *Solid State Ionics* **253** (2013) 217.
[128] B.E. Francisco, C.R. Stoldt, J.-C. M'Peko, *J. Phys. Chem. C* **119** (2015) 16432.
[129] A.K. Padhi, K.S. Nanjundaswamy, J.B. Goodenough, *J Electrochem Soc* **144** (1997) 1188.
[130] P.E. Stallworth, J.J. Fontanella, M.C. Wintersgill, C.D. Scheidler, J.J. Immel, S.G. Greenbaum, A.S. Gozdz, *J Power Sources* **81-82** (1999) 739.
[131] S. Balasubramanian, K.J. Rao, *J. Non-Cryst. Solids* **181** (1995) 157.
[132] M. Xu, J. Ding, E. Ma, *Appl Phys Lett* **101** (2012).
[133] R. Murugan, V. Thangadurai, W. Weppner, *Angew. Chem., Int. Ed.* **46** (2007) 7778.
[134] V. Thangadurai, S. Narayanan, D. Pinzaru, *Chem. Soc. Rev.* **43** (2014) 4714.
[135] J.C. Bachman, S. Muy, A. Grimaud, H.-H. Chang, N. Pour, S.F. Lux, O. Paschos, F. Maglia, S. Lupart, P. Lamp, *Chem. Rev.* **116** (2016) 23.
[136] K. Xu, *Chemical Reviews* **114** (2014) 11503.
[137] J. Awaka, N. Kijima, H. Hayakawa, J. Akimoto, *J. Solid State Chem.* **182** (2009) 2046.
[138] Z. Deng, Y. Mo, S.P. Ong, *NPG Asia Mater* **8** (2016) e254.
[139] S. Adams, R.P. Rao, *J. Mater. Chem.* **22** (2012) 7687.
[140] N. Bernstein, M.D. Johannes, K. Hoang, *Phys. Rev. Lett.* **109** (2012) 205702.
[141] Z. Hu, H. Liu, H. Ruan, R. Hu, Y. Su, L. Zhang, *Ceram. Int.* **42** (2016) 12156.
[142] E. Rangasamy, J. Wolfenstine, J. Sakamoto, *Solid State Ionics* **206** (2012) 28.
[143] C.A. Geiger, E. Alekseev, B. Lazic, M. Fisch, T. Armbruster, R. Langner, M. Fechtelkord, N. Kim, T. Pettke, W. Weppner, *Inorg. Chem.* **50** (2011) 1089.
[144] H. Buschmann, J. Dolle, S. Berendts, A. Kuhn, P. Bottke, M. Wilkening, P. Heitjans, A. Senyshyn, H. Ehrenberg, A. Lotnyk, V. Duppel, L. Kienle, J. Janek, *Phys. Chem. Chem. Phys.* **13** (2011) 19378.
[145] L.J. Miara, S.P. Ong, Y. Mo, W.D. Richards, Y. Park, J.M. Lee, H.S. Lee, G. Ceder, *Chem. Mater.* **25** (2013) 3048.
[146] W. Gu, M. Ezbiri, R.P. Rao, M. Avdeev, S. Adams, *Solid State Ionics* **274** (2015) 100.

[147] S. Ramakumar, L. Satyanarayana, S.V. Manorama, R. Murugan, *Phys. Chem. Chem. Phys.* **15** (2013) 11327.
[148] L.J. Miara, S.P. Ong, Y. Mo, W.D. Richards, Y. Park, J.M. Lee, H.S. Lee, G. Ceder, *Chem. Mater.* **25** (2013) 3048.
[149] H. Peng, Q. Wu, L. Xiao, *J. Sol-Gel Sci. Technol.* **66** (2013) 175.
[150] E.J. Cussen, *Chem. Commun.* (2006) 412.
[151] H.J. Deiseroth, S.T. Kong, H. Eckert, J. Vannahme, C. Reiner, T. Zaiß, M. Schlosser, *Angew. Chem., Int. Ed.* **47** (2008) 755.
[152] R.P. Rao, S. Adams, *Phys. Status Solidi A* **208** (2011) 1804.
[153] S. Boulineau, M. Courty, J.M. Tarascon, V. Viallet, *Solid State Ionics* **221** (2012) 1.
[154] O. Pecher, S.T. Kong, T. Goebel, V. Nickel, K. Weichert, C. Reiner, H.J. Deiseroth, J. Maier, F. Haarmann, D. Zahn, *Chem. - Eur. J.* **16** (2010) 8347.
[155] H.J. Deiseroth, J. Maier, K. Weichert, V. Nickel, S.T. Kong, C. Reiner, *Z. Anorg. Allg. Chem.* **637** (2011) 1287.
[156] V. Epp, Ö. Gün, H.J. Deiseroth, M. Wilkening, *J. Phys. Chem. Lett.* **4** (2013) 2118.
[157] M. Chen, R.P. Rao, S. Adams, *Solid State Ionics* **262** (2014) 183.
[158] R.P. Rao, N. Sharma, V.K. Peterson, S. Adams, *Solid State Ionics* **230** (2013) 72.
[159] B. Zhu, B.E. Mellander, J. Chen, *Mater. Res. Bull.* **28** (1993) 321.
[160] L. Zhang, K. Yang, J. Mi, L. Lu, L. Zhao, L. Wang, Y. Li, H. Zeng, *Adv. Energy Mater.* (2015).
[161] S.-H. Bo, Y. Wang, J.C. Kim, W.D. Richards, G. Ceder, *Chem. Mater.* **28** (2016) 252.
[162] L. Karlsson, R.L. McGreevy, *Solid State Ionics* **76** (1995) 301.
[163] P. Zetterström, R.L. McGreevy, A. Mellergård, J. Eriksen, *Appl. Phys. A* **74** (2002) S995.
[164] D. Wilmer, K. Funke, M. Witschas, R.D. Banhatti, M. Jansen, G. Korus, J. Fitter, R.E. Lechner, *Physica B* **266** (1999) 60.
[165] D. Wilmer, H. Feldmann, J. Combet, R.E. Lechner, *Physica B* **301** (2001) 99.
[166] P. Zetterström, R.L. McGreevy, A. Mellergård, J. Eriksen, *Applied Physics A* **74** (2002) s995.
[167] W.-G. Yin, J. Liu, C.-G. Duan, W.N. Mei, R.W. Smith, J.R. Hardy, *Phys. Rev. B* **70** (2004) 064302.
[168] H.M. Lu, J.R. Hardy, *Phys. Rev. Lett.* **64** (1990) 661.
[169] H.M. Lu, J.R. Hardy, *Phys Rev B* **42** (1990) 8339.
[170] L.X. Zhou, J.R. Hardy, H.Z. Cao, *Geophysical Research Letters* **24** (1997) 747.
[171] R.J. Harrison, A. Putnis, W. Kockelmann, *Phys. Chem. Chem. Phys.* **4** (2002) 3252.
[172] N. Kamaya, K. Homma, Y. Yamakawa, M. Hirayama, R. Kanno, M. Yonemura, T. Kamiyama, Y. Kato, S. Hama, K. Kawamoto, A. Mitsui, *Nat. Mater.* **10** (2011) 682.
[173] H.J. Deiseroth, S.T. Kong, H. Eckert, J. Vannahme, C. Reiner, T. Zaiss, M. Schlosser, *Angew. Chem., Int. Ed.* **47** (2008) 755.
[174] Z. Zhu, I.-H. Chu, Z. Deng, S.P. Ong, *Chem. Mater.* **27** (2015) 8318.
[175] A. Hayashi, K. Noi, A. Sakuda, M. Tatsumisago, *Nat. Commun.* **3** (2012) 856.
[176] M. Jansen, U. Henseler, *J. Solid State Chem.* **99** (1992) 110.
[177] N. Tanibata, K. Noi, A. Hayashi, M. Tatsumisago, *RSC Adv.* **4** (2014) 17120.
[178] N. Tanibata, A. Hayashi, M. Tatsumisago, *J. Electrochem. Soc.* **162** (2015) A793.
[179] N. Kamaya, K. Homma, Y. Yamakawa, M. Hirayama, R. Kanno, M. Yonemura, T. Kamiyama, Y. Kato, S. Hama, K. Kawamoto, *Nat. Mater.* **10** (2011) 682.

[180] Y. Mo, S.P. Ong, G. Ceder, *Chem. Mater.* **24** (2012) 15.
[181] S. Adams, R.P. Rao, *J. Mater. Chem.* **22** (2012) 7687.
[182] A. Kvist, A. Bengtzelius, *Fast Ion Transport in Solids* (1973).
[183] P. Bron, S. Johansson, K. Zick, J. Schmedt auf der Günne, S. Dehnen, B. Roling, *J Am Chem Soc* **135** (2013) 15694.
[184] A. Kuhn, O. Gerbig, C. Zhu, F. Falkenberg, J. Maier, B.V. Lotsch, *Phys. Chem. Chem. Phys.* **16** (2014) 14669.
[185] J. Walker, C. Catlow, *J. Phys. C: Solid State Phys.* **15** (1982) 6151.
[186] W. Smith, M.J. Gillan, *J. Phys.: Condens. Matter* **4** (1992) 3215.
[187] B. Hafskjold, X. Li, *J. Phys. Condens. Matter* **7** (1995) 2949.
[188] J.R. Walker, C.R.A. Catlow, *Nature* **286** (1980) 473.
[189] C.R. Peters, M. Bettman, J.W. Moore, M.D. Glick, *Acta Crystallogr* **27** (1971).
[190] R. Radzilowski, J. Kummer, *J. Electrochem. Soc.* **118** (1971) 714.
[191] W.L. Roth, *J. Solid State Chem.* **4** (1972) 60.
[192] P.K. Davies, F. Garzon, T. Feist, C.M. Katzan, *Solid State Ionics* **18** (1986) 1120.
[193] H. Engstrom, J.B. Bates, W.E. Brundage, J.C. Wang, *Solid State Ionics* **2** (1981) 265.
[194] J.B. Bates, H. Engstrom, J.C. Wang, B.C. Larson, N.J. Dudney, W.E. Brundage, *Solid State Ionics* **5** (1981) 159.
[195] G. Collin, J. Boilot, P. Colomban, R. Comes, *Phys. Rev. B* **34** (1986) 5838.
[196] J.T. Kummer, *Prog. Solid State Chem.* **7** (1972) 141.
[197] P. Padma Kumar, S. Yashonath, *J. Phys. Chem. B* **106** (2002) 3443.
[198] O. Kamishima, K. Kawamura, T. Hattori, J. Kawamura, *Solid State Ionics* **225** (2012) 47.
[199] R. Roy, E.R. Vance, J. Alamo, *Mater Res Bull* **17** (1982) 585.
[200] D.K. Agrawal, *Trans. Ind. Ceram. Soc.* **55** (1996) 1.
[201] R. Roy, D.K. Agrawal, J. Alamo, R.A. Roy, *Mater Res Bull* **19** (1984) 471.
[202] R. Roy, D.K. Agrawal, H.A. McKinstry, *Annu. Rev. Mater. Sci.* **19** (1989) 59.
[203] D.K. Agrawal, *J. Mater. Educ.* **16** (1994) 139.
[204] G.E. Lenain, H.A. McKinstry, S.Y. Limaye, A. Woodward, *Mater. Res. Bull.* **19** (1984) 1451.
[205] J. Alamo, R. Roy, *J. Mater. Sci.* **21** (1986) 444.
[206] G.E. Lenain, H.A. McKinstry, J. Alamo, D.K. Agrawal, *J. Mater. Sci.* **22** (1987) 17.
[207] H. Kohler, H. Schulz, *Mater. Res. Bull.* **20** (1985) 1461.
[208] K. Kang, Y.S. Meng, J. Bréger, C.P. Grey, G. Ceder, *Science* **311** (2006) 977.
[209] A. Martínez-Juárez, C. Pecharromán, J.E. Iglesias, J.M. Rojo, *J. Phys. Chem. B* **102** (1998) 372.
[210] R. Jalem, Y. Yamamoto, H. Shiiba, M. Nakayama, H. Munakata, T. Kasuga, K. Kanamura, *Chem. Mater.* **25** (2013) 425.
[211] P. Padma Kumar, S. Yashonath, *J. Am. Chem. Soc.* **124** (2002) 3828.
[212] B. Lang, B. Ziebarth, C. Elsasser, Inorg. Chem., 55 (2016), 2945
[213] M.A. Zendejas, J.O. Thomas, *Phys. Scr.* **47** (1993) 240.
[214] P.P. Kumar, S. Yashonath, *J. Phys. Chem. B* **106** (2002) 7081.
[215] S. Roy, P. Padma Kumar, *Phys. Chem. Chem. Phys.* **15** (2013) 4965.
[216] D.T. Qui, J.J. Capponi, J.C. Joubert, R.D. Shannon, *J. Solid State Chem.* **39** (1981) 219.
[217] A. Martínez-Juárez, C. Pecharromán, J.E. Iglesias, J.M. Rojo, *J. Phys. Chem. B* **102** (1998) 372.

[218] L. Jie-Rang, L. Shi-Chun, T. Shun-Bao, S. Hui-Jun, *Science in China Series A-Mathematics, Physics, Astronomy & Technological Science* **27** (1984) 889.
[219] M.A. Evstigneeva, V.B. Nalbandyan, A.A. Petrenko, B.S. Medvedev, A.A. Kataev, *Chem. Mater.* **23** (2011) 1174.

Chapter 2

Methodology

2.1 Introduction

Molecular dynamic (MD) simulations is a powerful tool for elucidation of structural and dynamical properties at the atomic level, thereby providing an understanding of the mechanism of physico-chemical properties of interest. Aided by the accelerated growth in computational techniques and also the developments of powerful algorithms, this technique is now well recognized for its predictive capability in optimization of structure and properties. It turns out a complimentary guideline for tailor making of materials. The works presented in this thesis are entirely based on MD simulations carried out on a family of fast ion conductors ($Na_2M_2TeO_6$ (M=Ni, Zn, Co and Mg) and $Li_{1+x}Ti_{2-x}Al_xP_3O_{12}$ ($x \leq 0.7$)) in order to extract useful microscopic insights contributing to conductivity.

The first ever Monte Carlo (MC) simulation was carried out by Metropolis in 1952 [34], on the MANIAC compute in Los, in which they simulated a dense liquid system employing a hard sphere model for the constituent particles. A few years later in 1957, another MC simulation was carried out by Wood and Parker [1] on liquid Argon (Ag) system employing empirically designed Lennard-Jones (LJ) interaction potential, and the results were readily compared with experimental data. Alder and Wainwright [35] employed these ideas to formulate the early form of MD, based on numerical solution of classical equation of motion by allowing the hard sphere particles to move at constant velocities. However, it is only in 1964, when Rahman [2] proposed a structured recipe for carrying of MD , demonstrating it on a system of LJ particles. This study was extended to di-atomic molecular liquid by Berne [5]. Since then much more complex systems, in terms of their extent and the nature of interaction between constituent particles, such as polymers [3] and proteins [4] are being investigated using molecular dynamics. The first MD simulation of a fast ion conductor was

carried out on α-AgI by Vashishta and Rahman in 1978 [5]. Currently computer simulation techniques are employed extensively in the study of solids, phase transitions, separation of mixtures, solid-solid and solid-liquid interfaces etc.

2.2 Molecular Dynamics

MD involves the numerical solution of the equations of motion for every constituent particle of the system, and provides the positions and velocities of them as a function of time from which theoretically all the properties of the system can be computed. There are two main classes of MD, based on the way the interatomic forces are calculated. In the first kind, known as classical MD the interaction potentials of constituent particles are predefined. Though it is very fast in computation, suffers from certain limitations, where electrons play an active role in the process, such as is the case when chemical bonds are formed or broken. For such purposes, density functional theory (DFT) [6, 7] based *ab initio* MD (AIMD), such as Car-Parinello MD (CPMD) [8] or Born-Oppenheimer MD (BOMD) is used [9]. But the computational overhead of AIMD is prohibitively high for large systems or cases where long simulation is required, such as are the cases discussed in this thesis. MD algorithms are currently available for different ensembles, such as microcanonical (NVE-MD), canonical (NVT-MD) and isobaric isothermal (NPT-MD) etc. Below we discuss the key concepts for carrying out MD simulations under different ensembles.

2.3 Microcanonical Molecular Dynamics (NVE-MD)

This is the most natural of ensembles in the context of MD simulations, where in the total number of particles (N), the volume (V) of the simulation box and the energy (E) of the system are kept constant. The total force acting on a particle due to the rest of the particles of the system is calculated by summing up the forces between all pairs,

$$\overrightarrow{F_i} = \sum_{\substack{j=1 \\ j \neq i}}^{N} \overrightarrow{F_{ij}}(r_{ij}) \tag{2.1}$$

r_{ij} being the interatomic distance between i^{th} and j^{th} atom and N is the total number of atom in the system. Force F_{ij} is calculated between the pair i and j by considering the spatial gradient of interatomic potential, u_{ij} (r_{ij}), between the pair of particles,

$$F_{ij} = -\frac{\partial u_{ij}}{\partial r_{ij}}\left(\frac{\alpha_j - \alpha_i}{r_{ij}}\right) \tag{2.2}$$

where α is the Cartesian components, x, y, and z. Therefore component wise acceleration of the i^{th} atom can be calculated as $\overrightarrow{a_i^{\alpha}} = \overrightarrow{F_i^{\alpha}} / m$, where $\overrightarrow{F_i^{\alpha}}$ is the total force acting on the i^{th} particle and m is the mass of it. Thus with proper initial positions and velocities, the equation of motion of each particle can be evaluated for the next time step following standard integration schemes. One of the popular integration scheme is the verlet algorithm [10, 11] where the position and velocity at the next time step $t + \delta t$ are calculated as follows,

$$\begin{aligned} \vec{r}(t+\delta t) &= 2\vec{r}(t) - \vec{r}(t-\delta t) + \vec{a}\delta t^2 \\ \vec{v}(t+\delta t) &= \frac{\vec{r}(t+\delta t) - \vec{r}(t-\delta t)}{2\delta t} \end{aligned} \tag{2.3}$$

where $\vec{r}(t)$ and $\vec{v}(t)$ are the position and velocity vector respectively at time t. The above equation is correct up to an order of δt^4. Time is discretised by a step-size of δt and typically of the order of femtoseconds (10^{-15} sec). However the main drawbacks of this algorithm is that the velocity does not appear explicitly in the equation, instead calculated as the first order central difference of positions from current and previous time steps. This is convenient particularly in controlling the temperature of the system, as discussed later in the chapter. A more popular algorithm is the "velocity"-form of Verlet algorithm.

Velocity-Verlet Algorithm

The scheme involves the following four steps [11, 12].

1. The first step is to move the velocity at the half time step ($t + \frac{\delta t}{2}$) using the initial velocity and acceleration following the equation,

$$\vec{v}\left(t + \frac{\delta t}{2}\right) = \vec{v}(t) + \frac{1}{2}\vec{a}(t)\delta t \tag{2.4}$$

2. Next step is to move the position of the atom at next step ($t + \delta t$) employing half moved velocity and previous position i.e.

$$\vec{r}(t+\delta t) = \vec{r}(t) + \vec{v}\left(t + \frac{\delta t}{2}\right)\delta t \tag{2.5}$$

3. In this step, the acceleration at the next time step $\vec{a}(t+\delta t)$ is calculated from the updated position; $\vec{r}(t+\delta t)$

4. Finally the full move of the velocity is completed by employing the half moved velocity and updated acceleration with the help of the equation,

$$\vec{v}(t+\delta t)=\vec{v}\left(t+\frac{\delta t}{2}\right)+\frac{1}{2}\vec{a}(t+\delta t)\delta t \tag{2.6}$$

Thus the position and velocity of the atom at time $t + \delta t$ is available. Repeating these four steps successively, for all the atoms in the system provides the trajectory. The trajectory at certain intervals are stored and analysed for system properties.

Temperature

According to equipartition theorem, there is an average energy of $\frac{1}{2}k_BT$ associated with each degree of freedom that appears as a square term in the Hamiltonian,

$$H=\sum_{i=1}^{N}u\left(\vec{r_1},\vec{r_2},...,\vec{r_N}\right)+\frac{1}{2}\sum_{i=1}^{N}m_iv_i^2 \tag{2.7}$$

There are 3N velocity degrees of freedom for a system consisting N number of atoms, and each one appears as $\frac{1}{2}m_iv_i^2$ in the kinetic energy (K) term in the Hamiltonian, H. Hence the instantaneous kinetic energy of the system is obtained as,

$$K=\frac{3}{2}Nk_BT=\frac{1}{2}\sum_{i=1}^{N}m_iv_i^2 \tag{2.8}$$

Thus temperature of the system is a function of the instantaneous K depending on instantaneous velocities of the particles in the system. Following the eqn. 2.8 the instantaneous and desired temperatures at any MD step can be calculated as,

$$T_{ins}=\frac{\sum_{i=1}^{N}m_i\left(v_i^{ins}\right)^2}{3Nk_B}$$
$$T_{des}=\frac{\sum_{i=1}^{N}m_i\left(v_i^{des}\right)^2}{3Nk_B} \tag{2.9}$$

The instantaneous temperature, T_{ins}, may not be same as the desired temperature. Therefore the desired temperature, T_{des}, will be obtained by multiplying the scale factor (S_f) to the velocities of each atom as follows,

$$S_f = \frac{v_i^{des}}{v_i^{ins}} = \sqrt{\frac{T_{des}}{T_{ins}}} \tag{2.10}$$

In practice, the instantaneous temperature of the system, T_{ins} over a few tens of MD steps is calculated, and a tolerance (δT_{tol}) is defined as required. The scaling is performed once it satisfies the condition: $T_{des} + \delta T_{tol} < T_{ins} < T_{des} - \delta T_{tol}$. The velocities of the atoms are scaled according to eqn. 2.10. This procedure when followed over a few thousands of MD steps at the early phase of the run, sets the instantaneous temperature of the system fluctuates around the desired temperature, T_{des}. Then the system is allowed to equilibrate without velocity scaling for a few nano-seconds of time. In practice the equilibrium is assumed once the instantaneous temperature and potential energy of the system settles to fluctuations about the mean. Remaining of the run, often termed as the production phase, is utilized for calculation of thermodynamic averages, and trajectories are stored for detailed analysis of structural and dynamical properties. Ensuring good energy and linear momentum conservation is very important for reliability of results.

The MD algorithm is founded on the ergodic hypothesis which says that the time average is equal to the ensemble average. It means that over long period of time, the system will evolve through all accessible microstates with constant energy ensuring reliable sampling. However, experiments are often conducted at constant temperature and constant pressure. Thus, to calculate lattice parameters or to investigate phase transitions, isobaric-isothermal molecular dynamics (NPT-MD) algorithm (to be discussed later) is developed.

Periodic Boundary Condition (PBC)

Typical number of atoms in bulk system is of the order of 10^{23} while in computer simulation typically the number of atoms is around 1000 − 10000 (that is, typically of size 20 to 40 Å). Hence in simulated system, a large fraction of atoms reside on the surface. Since the surface atoms of the simulation cell feel different atmosphere than the atoms which are deep inside, the nature of the bulk of the system is not correctly reproduced.

The surface effect can be minimized employing periodic boundary conditions, in which the original simulation cell is imagined to be surrounded by imaginary replicas of the original simulation cell. For an orthogonal simulation cell (with sides L_x, L_y, L_z), the co-ordinates (x', y', z') of the image particles in the surrounding replicas are related by,

$$\begin{aligned} x' &= x_{simu} + n_x L_x \\ y' &= y_{simu} + n_y L_y \\ z' &= z_{simu} + n_z L_z \end{aligned} \tag{2.11}$$

where x_{simu}, y_{simu} and z_{simu} are the coordinates of particles in the original simulation cell, and n_x, n_y, n_z are positive or negative integers including zero. With the help of the PBC, all the particles can find their infinite number of images. Thus infinite pairs of interactions have to be considered which is not physible. We have to forcefully consider the interaction up to certain distances. Typically the short range interaction dies out rapidly with in half of the box length (L). Hence a cut off distance R_c is chosen such that it is less than or equals to $L/2$. If we consider the interaction of each particle with in R_c, It allows the particle to interact with other real particles or its image whichever is closest. This condition is known as the minimum image convention.

For non-orthogonal simulation box the real co-ordinates should be transformed to scaled co-ordinates applying suitable matrix transformation to the real coordinates. For the purpose, and h –matrix is defined as,

$$h = \begin{pmatrix} a & b_x & c_x \\ 0 & b_y & c_y \\ 0 & 0 & c_z \end{pmatrix}$$

where, a, b and c are the cell parameters and subscripts are corresponding x, y and z components. If x, y and z are the real co-ordinates of an atom, then the corresponding scaled co-ordinates can be obtained following the equation, $\bar{s} = h^{-1}\bar{r}$. Scaled co-ordinates provides the corresponding co-ordinates in an orthogonal simulation box with sides of unit length. Now PBC can be implemented on the scaled coordinates using equation 2.11 itself, with $L_x = L_y = L_z = 1$.

Canonical ensemble Molecular Dynamics (NVT)

In order to control the temperature of the simulated system velocity scaling, discussed earlier may be employed. However, there is no rigorous proof that velocity scaling confirms to canonical ensemble. In this contest, extended Hamiltonian method to control temperature was first introduced by Nose [13, 14] and subsequently developed by Hoover [15]. Conceptually, the heat bath is an integral part of the system by introducing an extra degree of freedom $\tilde{s}$ and associated with a fictitious mass *Q*. $\widetilde{p_s}$ is the conjugate momentum of $\tilde{s}$. The mass of the fictitious particle determines the temperature fluctuation. The variable *s* actually scales the time (*t*) as,

$$dt = sdt \tag{2.12}$$

The atomic position variable remains same. Thus it the transformation is like

$$\tilde{r} = r,\ \dot{\tilde{r}} = \tilde{s}^{-1}\dot{r},\ \tilde{s} = s \text{ and } \dot{\tilde{s}} = \tilde{s}^{-1}\dot{s} \tag{2.13}$$

The Hamiltonian of the extended system is chosen as,

$$H = \sum_i \frac{\widetilde{p_i}^2}{2m_i} + U(\tilde{r}) + \frac{\widetilde{p_s}^2}{2Q} + gk_BT_0 \ln \tilde{s} \tag{2.14}$$

The first two terms are the kinetic energy and potential energy of the real system respectively. The third and fourth terms are the kinetic energy of the fictitious particle and corresponding potential energy. The potential of the fictitious particle is chosen in logarithmic form such that the system follows a canonical ensemble and $g = N_{df}$ is the total degrees of freedom and *d* indicates the dimensionality of the system.

Thus Nosé-Hoover equations can be written as,

$$\dot{\tilde{r}}_i = \frac{\widetilde{p_i}}{\mathrm{m_i}} \tag{2.15}$$

$$\dot{\widetilde{p}}_i = -\frac{p_s}{Q}\widetilde{p_i}$$

$$\dot{\tilde{s}} = \frac{\widetilde{p_s}}{\mathrm{Q}}$$

$$\dot{\widetilde{p}}_s = \sum_i \frac{p_i^2}{m_i} - k_BT \ln \tilde{s}$$

The experiments are mainly performed at constant pressure (P) instead of constant volume (V). Thus isothermal-isobaric MD is more realistic than NVT-MD. In NPT-MD, the cell volume is allowed to fluctuate and equilibrium volume is achieved by balancing internal pressure and the external set pressure.

Isobaric Isothermal Molecular Dynamics (NPT-MD)

The NVT-MD can be extended to NPT-MD by introducing one more degree of freedom (V) associated with hydrostatic pressure (P). The associated extended Hamiltonian can be written as,

$$H_{ext} = H(\tilde{p},\tilde{r}) + \frac{\tilde{p}_V^{\,2}}{2W} + \frac{\tilde{p}_s^{\,2}}{2Q} + gk_BT_0 \ln \tilde{s} + P_{ext}V \tag{2.16}$$

Similarly, the second and third term are the kinetic part associated with barostat and thermostat respectively and last two terms are the potential energy associated with the thermostat and change of volume respectively. The W is the mass of the fictitious particle associated with the degree of freedom V. Thus W determines the pressure fluctuations.

In NPT-MD simulations the shape and volume of the cell are allowed to vary depending on the difference in the required or external pressure, P_{ext} and the internal stress tensor. In the later chapters, we have employed the triclinic form of NPT-MD.

2.4 Interatomic potential

Quality of interatomic potential plays significant role in carrying out a successful simulation that would reproduce available experimental data and thus ensure reliability of the results. Depending on the chemical nature of matter several functional forms of interatomic potentials are proposed in the literature. Some of the popular forms are, the Lennard-Jones (LJ) [10, 16], Born-Mayer (BM) [10], Vashishta Rahman [5] etc. The form of the LJ potential is,

$$u\left(r_{ij}\right) = 4\varepsilon\left[\left(\frac{\sigma}{r_{ij}}\right)^{12} - \left(\frac{\sigma}{r_{ij}}\right)^{6}\right] \tag{2.17}$$

where r_{ij} is the interatomic distance between particle i and j. σ is equal to the diameter of the particle. LJ has been mostly employed to simulate inert gases such as argon, xenon etc. [17, 18]. A few ionic solids where LJ potential with an additional Coulombic term is also

modelled using [19]. The short-range attractive term arises due to the overlap of electron clouds and the attractive term appears due to the interaction between instantaneous dipoles. Born-Mayer-Huggins (BMH) potential [20] is one of the most common potential employed for simulation of ionic solids, especially alkali halides. It has the functional form,

$$u\left(r_{ij}\right)=\frac{q_i q_j}{r_{ij}}+A_{ij}\,exp\left(-\frac{r_{ij}}{\rho}\right)-\frac{C_{ij}}{r_{ij}^{\,6}}-\frac{D_{ij}}{r_{ij}^{\,8}} \tag{2.18}$$

where q_i is the charge of the ion, A_{ij}, C_{ij}, D_{ij} are the overlap repulsive energy, instantaneous dipole-dipole attractive term, dipole-quadrupole overlap attractive energy. BMH potential have been employed widely in simulating molten phases of several inorganic solids [20-22] such as β-alumina [23], Li_3N [24], $SrCl_2$ [25], CaF_2 [26, 27], $LiMn_2O_4$ [28], $Gd_2Zr_2O_7$ [29] etc.

In 1978 Vashistha and Rahaman [5] introduced a new functional form for the study of superionic conductor, α-AgI,

$$V_{ij}(r_{ij})=\frac{q_i q_j}{4\pi\varepsilon_0 r_{ij}}+\frac{A_{ij}\left(\sigma_i+\sigma_j\right)^{n_{ij}}}{r_{ij}^{\,n_{ij}}}-\frac{P_{ij}}{r_{ij}^{\,4}}-\frac{C_{ij}}{r_{ij}^{\,6}} \tag{2.19}$$

in the above expression q_i is the charge and σ_i is the ionic radius [48] of the i^{th} ion. The parameters, A_{ij}, P_{ij} and C_{ij} respectively describe the overlap-repulsion energy of the electron clouds, the charge dipole interactions (in an average sense) and the dispersion constant, between ion pairs i and j. It has a softer overlaping repulsion ($1/r^n$, where n = 11, 9 or 7, respectively for cation-cation, cation-anion and anion-anion pairs) compared to the more popular Born-Mayer (Buckingham) and Lennard-Jones potentials. Subsequently, this potential has been employed in the study of several other super ionic conductors as well [30-33].

Interaction between atoms can be separated into two classes; short range and long range. Coulomb interactions are long range in nature as they die off slower than the third power of the inverse distance between pairs. To save the computational time short range interactions are usually dealt with a cut-off distance (R_c) beyond which the potential energy $u(R_c) \approx 0$. As long as R_c is chosen to be sufficiently large the cut-off will only impose very minimal perturbation on the system. Again R_c cannot be larger than half of the smallest sides of the simulation box to be consistent with minimum image convention.

2.5 Ewald Summation

Coulomb potential is more demanding to deal with as it does not converge inside the simulation cell. In principle for large enough systems screening by the neighbouring atoms would diminish the effect of the potential. However, this would have occurred over a range of several of tens or hundreds of nanometres but unfortunately simulation cells are only few nanometres long. Therefore for Coulombic contribution, original simulation cell and all its infinite images must be considered [11]. The total Coulombic contribution due to the potential energy of the *N* particle system is,

$$u = \frac{1}{8\pi\varepsilon_0} \sum_{n} \sum_{\substack{i,j=1 \\ i \neq j}}^{N} \frac{q_i q_j}{|r_{ij} + nl|} \tag{2.20}$$

where $nl = n_x l_x, n_y l_y, n_z l_z$ are the lattice vectors of infinite periodic images. The sum is over all the periodic images, *n,* and over all particles *j* and *N* is the total number of particles. However, this sum is only conditionally convergent. In eqn. 2.20 the charge density have been represented as a sum of δ functions (the charge density of point charge) and the potential decays as *1/r*. In Ewald summation, a Gaussian charge distribution of opposite sign surrounding every charge q_i is assumed, such that the total charge of the cloud exactly cancels q_i. Another compensating Gaussian with the same charge is also needed. The point charge and the opposite Gaussian interaction can converge quickly and is calculated in real space considering as short range interaction (u_{srt}). And, the remaining contributions from the periodic compensating Gaussian charge distributions (i.e., long range interaction, u_{lr}) are calculated in the Fourier space. It can be written as $u_{Ewald} = u_{srt} + u_{lr} - u_{self}$. The contribution from each term can be calculated as follows.

Short-range part

The potential contribution from the screened point charges is short range in nature. Consider the expression for the screening Gaussian charge distribution of width α around the charge q_j $\rho(r) = -q_j \left(\frac{\alpha}{\pi}\right)^{\frac{3}{2}} e^{-\alpha r^2}$. The potential at a distance *r* from the centre of this Gaussian charge distribution using Poisson's equation can be written as,

$$u_{gs} = -\frac{q_j}{r} erf\left(\sqrt{\alpha r}\right) \tag{2.21}$$

where $$erf(x) = \frac{2}{\sqrt{\pi}} \int_0^x e^{-u^2} du$$

is the error function. The contribution of the screened point charge, u_{scr} at a distance r from the point charge is,

$$u_{scr} = u_{point} + u_{gs} = \frac{q_j}{r} - \frac{q_j}{r} erf\left(\sqrt{\alpha r}\right) = \frac{q_j}{r} erfc\left(\sqrt{\alpha r}\right) \tag{2.22}$$

where

$$erfc(x) = 1 - erf(x)$$

is the so called complementary error function. Total contribution from short range part is,

$$u_{srt} = \frac{1}{2} \sum_{\substack{i,j=1 \\ i \neq j}}^{N} \frac{q_i q_j erfc\left(\sqrt{\alpha r_{ij}}\right)}{r_{ij}} \tag{2.23}$$

The summation goes up to the number of atoms within the short range cut-off R_c. The total charge for the Gaussian part at $r = 0$ is,

$$u_{cnt}(r=0) = 2q_j \left(\frac{\alpha}{\pi}\right)^{\frac{1}{2}} \tag{2.24}$$

and it should be subtracted from total as it is a self-correction part. Therefore total self-correction for the entire system becomes,

$$u_{self}(r=0) = \frac{1}{2} \sum_{i=1}^{N} 2q_i^2 \left(\frac{\alpha}{\pi}\right)^{\frac{1}{2}} = \left(\frac{\alpha}{\pi}\right)^{\frac{1}{2}} \sum_{i=1}^{N} q_i^2 \tag{2.25}$$

Long-range part

The potential energy contribution from the compensating Gaussian charge distribution is calculated in Fourier space. The properties of Poisson's equation has been applied to calculate the contribution of the compensating Gaussian charge distribution. The total charge distribution of a periodic sum of Gaussians can be written as [11],

$$u_{Ewald} = \frac{1}{2}\sum_{\substack{i,j=1 \\ i\neq j}}^{N} \frac{q_i q_j erfc\left(\sqrt{\alpha} r_{ij}\right)}{r_{ij}} + \sum_{k\neq 0} \frac{4\pi}{k^2} |\rho(k)|^2 \, exp\left(-\frac{k^2}{4\alpha}\right) + \left(\frac{\alpha}{\pi}\right)^{\frac{1}{2}} \sum_{i=1}^{N} q_i^{\,2} \qquad (2.26)$$

where the long range contribution is given by $u_{lr} = \sum_{k\neq 0} \frac{4\pi}{k^2} |\rho(k)|^2 \, exp\left(-\frac{k^2}{4\alpha}\right)$

2.6 Property Calculation

Thermodynamic Properties

Once we have trajectory of the all particles, the thermodynamic quantities of the system such as, total energy, temperature, pressure of the system can be calculated from the computer simulation. Specific heat at constant volume (C_V) in microcanonical (NVE) and canonical ensemble (NVT), as well as specific heat (C_P) at constant pressure in isobaric isothermal ensemble (NPT) can be calculated from the fluctuations of temperature, total energy and enthalpy [21] as follows,

$$\begin{aligned} C_v(NVE) &= \frac{k_B}{\frac{2}{3N} - \frac{\langle T^2\rangle - \langle T\rangle^2}{\langle T\rangle^2}} \\ C_v(NVT) &= \frac{1}{k_B T^2}\left(\langle E^2\rangle - \langle E\rangle^2\right) \\ C_p(NPT) &= \frac{1}{k_B T^2}\left(\langle H^2\rangle - \langle H\rangle^2\right) \end{aligned} \qquad (2.27)$$

where E, P and V are the total energy, pressure and volume respectively and $H = E + PV$ is the enthalpy. These are so-called response functions which are essentially important in case of the normal to superionic phase transitions.

2.7 Radial Distribution function

The radial distribution function (RDF) or sometimes known as pair distribution function (PDF), is a useful tool to characterize the structure of the simulated system. The mathematical expression of RDF between pair of atom i and j is,

$$g_{ij}(r) = \frac{V}{4\pi r^2 \Delta r N_i N_j} \sum_{k=1}^{N_j} n_k(r, \Delta r) \qquad (2.28)$$

where V is the volume of the simulation box, and N_i and N_j are the total number of i^{th} and j^{th} atoms respectively constituting the system. The subscript of g_{ij} indicates that we are sitting on the i^{th} particle and looking at the j^{th} particle. Essentially it is the ratio of the number density of the j^{th} particles inside a spherical shell between radius r and $r + \Delta r$ with respect to the i^{th} particle to the total number density of the j^{th} particles. Thus, it clearly describes the distribution of the j^{th} particles with respect to the i^{th} particles. Running co-ordination number (RCN), $C_{ij}(r)$ at distance r, is defined as the integration of g_{ij} (r) from distance zero to distance r.

$$C_{ij}(r) = \int_0^r 4\pi s^2 g_{ij}(s) ds \tag{2.29}$$

Therefore, it essentially gives the number of neighbours of j^{th} particles sitting at a particular distance r with respect to the i^{th} particles.

2.8 Mean Square Displacement

Mean square displacement (*MSD*) describes the average distance square travelled by an atom with respect to time (t). It is defined as,

$$MSD = \left\langle |\vec{r_i}(t) - \vec{r_i}(0)|^2 \right\rangle \tag{2.30}$$

where $\vec{r_i}(t)$ is the position vector of the i^{th} particle after time t. For d-dimensional motion, the diffusivity D is estimated from the Einstein's equation [11],

$$D = \lim_{t' \to \infty} \frac{1}{2dNt} \langle \sum_{j=1}^{N} \left[\vec{r_j}(t+t') - \vec{r_j}(t) \right]^2 \rangle \tag{2.31}$$

The diffusion coefficient is related to the ionic conductivity through the Nernst–Einstein equation,

$$\sigma = \frac{cq^2 D}{k_B T} \tag{2.32}$$

where c is the number density of the mobile species, k_B the Boltzmann constant, T the temperature of the simulation, q is the formal charge of the mobile ion. The temperature dependence of the ionic conductivity generally obeys the Arrhenius equation,

$$\sigma = \frac{\sigma_0}{T}\exp(-E_a / k_B T). \qquad (2.33)$$

Thus the slope of $ln(\sigma T)$ against $1/T$ provides the activation energy E_a and σ_0 is a pre exponential factor. Activation energy is believed to be a direct measure of the microscopic barrier for ion transport, also offers a qualitative comparison of different fast ion conductors.

All these tools are employed in the analysis of the structural and dynamical properties of fast ion conductors described in the later chapters of this thesis.

Bibliography

[1] W. Wood, F. Parker, *J. Chem. Phys.* **27** (1957) 720.
[2] A. Rahman, *Phys. Rev.* **136** (1964) A405.
[3] J.-P. Ryckaert, A. Bellemans, *Chem. Phys. Lett.* **30** (1975) 123.
[4] J.A. McCammon, B.R. Gelin, M. Karplus, *Nature* **267** (1977) 585.
[5] P. Vashishta, A. Rahman, *Phys. Rev. Lett.* **40** (1978) 1337.
[6] P. Hohenberg, W. Kohn, *Kohn W, Sham LJ (1965) Phys Rev* **140** (1964) A1133.
[7] W. Kohn, L.J. Sham, *Phys. Rev.* **140** (1965) A1133.
[8] R. Car, M. Parrinello, *Phys. Rev. Lett.* **55** (1985) 2471.
[9] D. Marx, J. Hutter, *Ab initio molecular dynamics: basic theory and advanced methods*, Cambridge University Press (2009).
[10] M.P. Allen, D.J. Tildesley, *Computer simulation of liquids*, Oxford university press (1989).
[11] D. Frenkel, B. Smit, *Understanding molecular simulation: From algorithms to applications* (1996).
[12] M. Tuckerman, Statistical mechanics: theory and molecular simulation (2010)
[13] S. Nosé, *Mol. Phys.* **52** (1984).
[14] S. Nosé, *The Journal of Chemical Physics* **81** (1984) 511.
[15] W.G. Hoover, *Phys. Rev. A* **31** (1985) 1695.
[16] C. Kittel, D.F. Holcomb, *Am. J. Phys* **35** (1967) 547.
[17] R. Etters, J. Kaelberer, *Phys. Rev. A* **11** (1975) 1068.
[18] H.L. Davis, J. Jellinek, R.S. Berry, *J. Chem. Phys.* **86** (1987) 6456.
[19] D. Adams, *Mol. Phys.* **29** (1975) 307.
[20] M.P. Tosi, *Solid state physics* **16** (1964) 1.
[21] D. Adams, *Mol. Phys.* **28** (1974) 1241.
[22] J.W. Lewis, K. Singer, *J. Chem. Soc., Faraday Trans. 2* **71** (1975) 41.
[23] M. Wolf, J. Walker, C. Catlow, *Solid State Ionics* **13** (1984) 33.
[24] M. Wolf, C. Catlow, *J. Phys. C: Solid State Phys.* **17** (1984) 6635.
[25] M.J. Gillan, M. Dixon, *J. Phys. C: Solid State Phys.* **13** (1980) 1901.
[26] Z. Cheng, J. Chang, Z. Jia, N. Chen, *Mol. Simul.* **10** (1993) 27.
[27] R.A. Montani, *J. Chem. Phys.* **100** (1994) 8381.
[28] B. Ammundsen, J. Paulsen, *Adv. Mater.* **13** (2001) 943.
[29] P. Wilde, C. Catlow, *Solid State Ionics* **112** (1998) 173.
[30] J.R. Ray, P. Vashishta, *J. Chem. Phys.* **90** (1989) 6580.
[31] P. Sindzingre, M. Gillan, *J. Phys. C: Solid State Phys.* **21** (1988) 4017.
[32] C. Catlow, G.D. Price, *Nature* **347** (1990) 243.
[33] A. Annamareddy, J. Eapen, *J. Chem. Phys.* **143** (2015).
[34] N. Metropolis, A. W. Rosenbluth, M. N. Rosenbluth, A. H. Teller, and E. Teller, J. Chem. Phys. **21**, 1087 (1953).
[35] B. Alder and T. Wainwright, J. Chem. Phys. **27**, 1208 (1957).

Chapter 3

Ion Transport in $Na_2M_2TeO_6$: Insights from Molecular Dynamics Simulation

3.1 Introduction

The present modeling and MD simulations is motivated by the recent experimental studies of Evstigneeva et al. [1] who synthesized a family of fast ion of Na^+ conducting fast ion solids [2, 3] of the formula, $Na_2M_2TeO_6$, where M = Ni, Zn, Co or Mg. $Na_2M_2TeO_6$ consists of edge shared MO_6 and TeO_6 octahedral layers spanning the ab-plane, with the Na^+ ions occupying the inter-layer (shown in figure 3-1). The MO_6 and TeO_6 octahedra show honeycomb like order in the octahedral layer and arranged 2:1 ratio. Na^+ ions are located at Na1, Na2 and Na3 identified by XRD structure. There are three Na1 sites, two Na2 sites and one Na3 site per unit cell per layer. All the series have exhibited two dimensional conductivity due to rigid octahedral layers. The Ni-containing composition shows highest ionic conductivity of the family (σ = 0.11 S/cm at 573 K, which compares well with the β-alumina [4-7]) and promises scope for further improvements through aliovalent substitutions [8]. The present study provides an accurate interatomic potential for the family of $Na_2M_2TeO_6$, where M = Ni, Co, Zn or Mg, and fresh insights on ion transport in them is derived, focusing on the highest conducting $Na_2Ni_2TeO_6$.

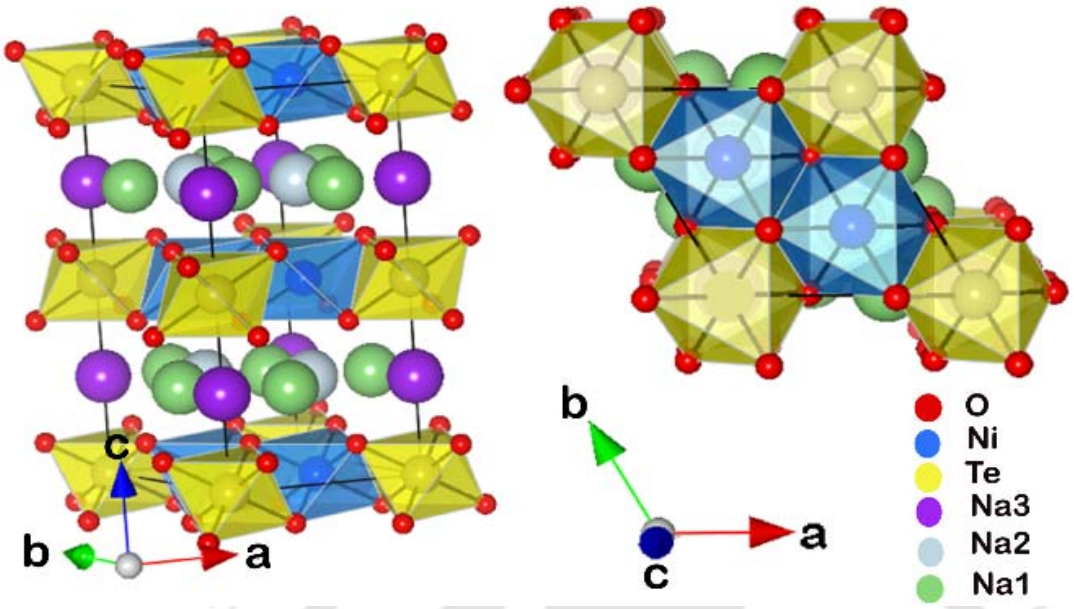

Figure 3-1. Views of the $Na_2Ni_2TeO_6$ structure having edge-shared octahedral layers parallel to the ab-plane; NiO_6 –octahedra (blue) and TeO_6-octahedra (yellow). One rhombohedral unit cell marked by black lines (left), along with the fringe atoms on the cell edges and oxygens (red) necessary for completing the octahedra are shown. The Na sites, Na1 (green), Na2 (light blue), and Na3 (violet), are also shown.

3.2 Methodology

3.2.1. Interatomic Potential

We employ the Vashishta-Rahman form of the interatomic potential, that have performed remarkably well for a variety of systems such as, AgI [9-12], Ag_2Se [13, 14], and NASICONs [15-17] and is given by,

$$V_{ij}(r_{ij}) = \frac{q_i q_j}{r_{ij}} + \frac{A_{ij}\left(\sigma_i + \sigma_j\right)^{n_{ij}}}{r_{ij}^{\,n_{ij}}} - \frac{P_{ij}}{r_{ij}^{\,4}} - \frac{C_{ij}}{r_{ij}^{\,6}} \tag{3.1}$$

where q_i is the charge and σ_i is the ionic radius [18] of the i^{th} ion. The parameters, A_{ij}, P_{ij} and C_{ij} respectively describe the overlap-repulsion energy of the electron clouds, the charge dipole interactions (in an average sense) and the dispersion constant, between ion pairs i and j as shown in figure 3-2. It has a softer overlap repulsion ($1/r^n$, where n = 11, 9 or 7,

Table 3.1. Inter ionic potential pair parameters employed in present study.

X	q_x (C)	σ_x (Å)	A_{Na-X} (eV)	A_{X-O} (eV)	C_{X-O} (eVÅ^6)	P_{X-O} (eVÅ^4)
Na	0.65	1.13	2.298	0.1061	0.00	0.0
M=Ni	1.30	0.69	24.256	3.0846	59.85	31.0
Zn	1.30	0.74	21.965	3.4876	89.85	35.0
Co	1.30	0.79	16.431	2.8356	94.85	35.0
Mg	1.30	0.86	11.082	2.1508	115.85	35.0
Te	3.90	0.70	9.081	3.9098	17.15	11.3
O	-1.30	1.21	0.106	0.9260	85.14	0.0

n_{ij}=11, 9 or 7 respectively for cation-cation, cation-anion and anion-anion.

respectively for cation-cation, cation-anion and anion-anion pairs) compared to the more popular Born-Mayer (Buckingham) where it decays exponentially and Lennard-Jones potentials, more so between the anions. An optimized set of parameters for the entire family of $Na_2M_2TeO_6$, where M = Ni, Co, Zn or Mg, is developed empirically (see Table 3.1) by fitting to their corresponding X-ray structure and conductivity at 600 K [1].

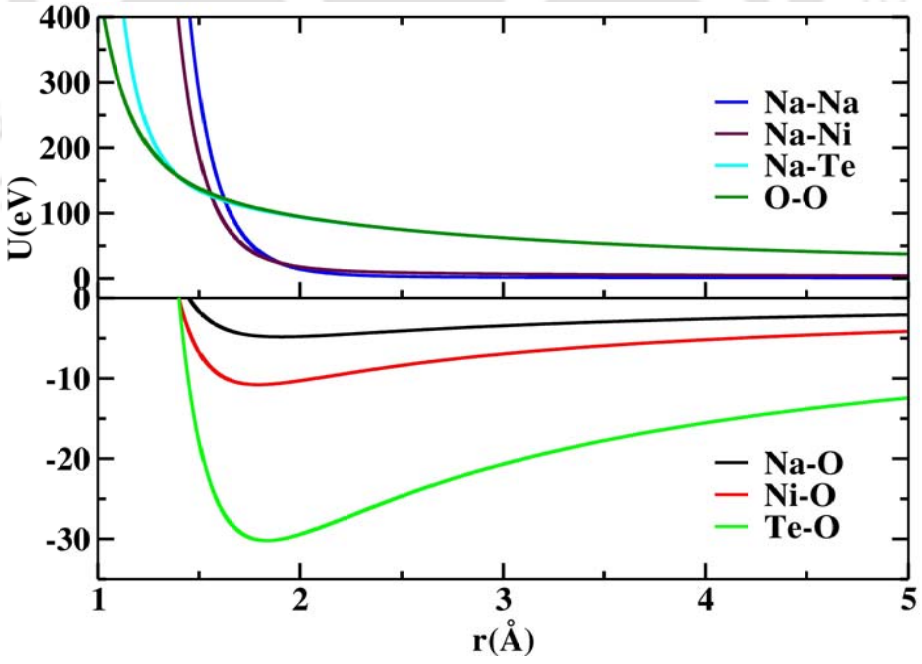

Figure 3-2. Plot of the interaction pair potential between selected species, Na-Na, Na-Ni, Na-Te, O-O (top panel), Na-O, Ni-O and Te-O (bottom panel), are given over a range of 1-5 Å.

The fitting procedure follows a series of MD simulations, each, typically, of 2 nano-seconds, with a refined set of parameters until various interatomic distances and local coordination numbers agree with the X-ray structure. After stabilizing the framework structure Na-Na and Na-O parameters are refined to reproduce the experimental conductivity. The Ni-O interaction is also a determined factor of the Na^+ diffusion. Lower the Ni-O produces higher Na^+ channel attributing higher diffusion.

3.2.2 Computational Details

Employing the optimized set of parameters listed in table 3.1 isothermal-isobaric ensemble molecular dynamics simulations (NPT-MD) are carried out at several temperatures, all at 1 atm. pressure. The NPT-MD method, due to Parrinello-Rahman [19], allows for changes in the shape as well as size of the simulation box. Simulations are started from their respective X-ray structures and with initial velocities sampled from a Gaussian distribution at the desired temperature. The rhombohedral unit cell comprises of 2 formula units of $Na_2M_2TeO_6$. The simulation super-cell in all cases included 5 × 5 × 2 unit cells comprising of 1100 ions (200-Na^+, 200-M^{2+}, 100-Te^{6+} and 600-O^{2-}). A short-range cut off 11 Å is implemented. A time step of 2 femtoseconds is used to evolve the trajectories. Typically the runs are 12 nanoseconds or longer, with trajectory samples stored at intervals of 200 femtoseconds for detailed analysis. However, a few long runs of 100 nanoseconds are carried to ensure convergence of properties, and also a few runs with larger systems consisting of 6×6×3 unit cells to ensure the adequacy of the system size. Periodic boundary conditions in all directions, and Ewald summation technique for the convergence of long-range Coulombic interactions are implemented. The NPT-MD simulations were performed with the software package LAMMPS [20]. Since the short-range part of the interaction potential (all except the Coulombic term in equation 3.1) is not available in the software, a tabulated form is used instead. A few micro canonical MD (NVE-MD) runs are also carried out (using our in-house software) for the Ni-containing system from which microscopic aspects such as the population and potential energy distribution of Na^+ ions in a unit cell are calculated.

3.3 Results and Discussion

3.3.1 Framework Structure

The $Na_2M_2TeO_6$ compounds, where M = Ni, Co, Zn, or Mg, has a layered structure of TeO_6 and MO_6 octahedra spanning the ab-plane of their hexagonal lattice following honeycomb order (see figure 3-1). The octahedral layers are held together along the c-axis by Van der Waals forces and by interactions mediated through Na^+ ions occupying their interlayers. The proposed interatomic potential retains these structural features in excellent agreement with the experiments. The average cell parameters of $Na_2M_2TeO_6$ calculated from isothermal-isobaric ensemble molecular dynamics (NPT-MD) averaging over 6000 frames at 300 K is compared with room-temperature experimental values in Table 3.2. The calculated lattice parameters on substitution at the M-site follows the trend observed in experiments. The deviations from experimental values in all cases are well within one percent. The lattice parameter fluctuation with the simulation time is also shown in figure 3-4 at 600 K for M = Ni, Co, Zn, or Mg. .

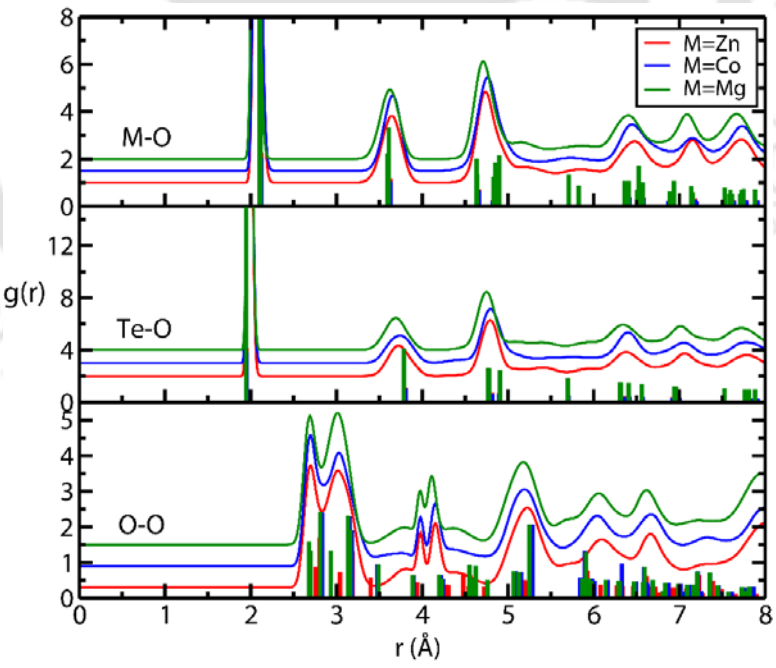

Figure 3-3. The radial distribution function (RDF), g(r), between selected ion pairs, M-O (M = Zn, Co and Mg), Te-O, O-O, of $Na_2M_2TeO_6$ at room temperature. The g(r)'s calculated for the X-ray structure are shown as vertical bars in matching colors. The functions are displaced uniformly along Y-axis for clarity.

Table 3.2. The average lattice parameters for $Na_2M_2TeO_6$ from NPT-MD at 300K is compared with experimental results.

Composition	Space Group	Para-meters	Expt.	NPT-MD	|Δ| (%)
$Na_2Ni_2TeO_6$	$P6_3/mcm$	a(Å)	5.207	5.211	0.06
		b(Å)	5.207	5.213	0.10
		c(Å)	11.156	11.163	0.06
		α	90.00	90.02	0.02
		β	90.00	89.97	0.03
		γ	120.00	120.04	0.03
$Na_2Zn_2TeO_6$	$P6_322$	a(Å)	5.280	5.285	0.10
		b(Å)	5.280	5.293	0.24
		c(Å)	11.294	11.306	0.10
		α	90.00	89.99	0.01
		β	90.00	89.95	0.05
		γ	120.00	120.16	0.13
$Na_2Co_2TeO_6$	$P6_322$	a(Å)	5.289	5.283	0.12
		b(Å)	5.289	5.269	0.38
		c(Å)	11.214	11.202	0.11
		α	90.00	89.51	0.54
		β	90.00	90.25	0.28
		γ	120.00	119.75	0.21
$Na_2Mg_2TeO_6$	$P6_322$	a(Å)	5.254	5.240	0.10
		b(Å)	5.254	5.246	0.24
		c(Å)	11.255	11.225	0.26
		α	90.00	90.21	0.23
		β	90.00	89.72	0.31
		γ	120.00	120.09	0.08

The radial distribution functions, g(r), between selected ion pairs, M-O, Te-O and O-O, from NPT-MD simulations at 300 K for the $Na_2M_2TeO_6$ compounds (M = Co, Zn and Mg) are shown in figure 3-3. The bar-plots are the corresponding g(r) based on room temperature X-ray structure [1]. All the peaks locations in the simulated g(r) are consistent with their static g(r), calculated for the X-ray structure, except for the thermal broadening. The Te and M ions makes sharp six-coordinations with the oxygens in all cases, and the

layer structure is retained intact. The average Te-O and M-O distances of the octahedra, for M=Ni, Zn, Co, Mg calculated from MD simulations (listed in Table 3.3) also show good agreement with the reported X-ray structure [1].

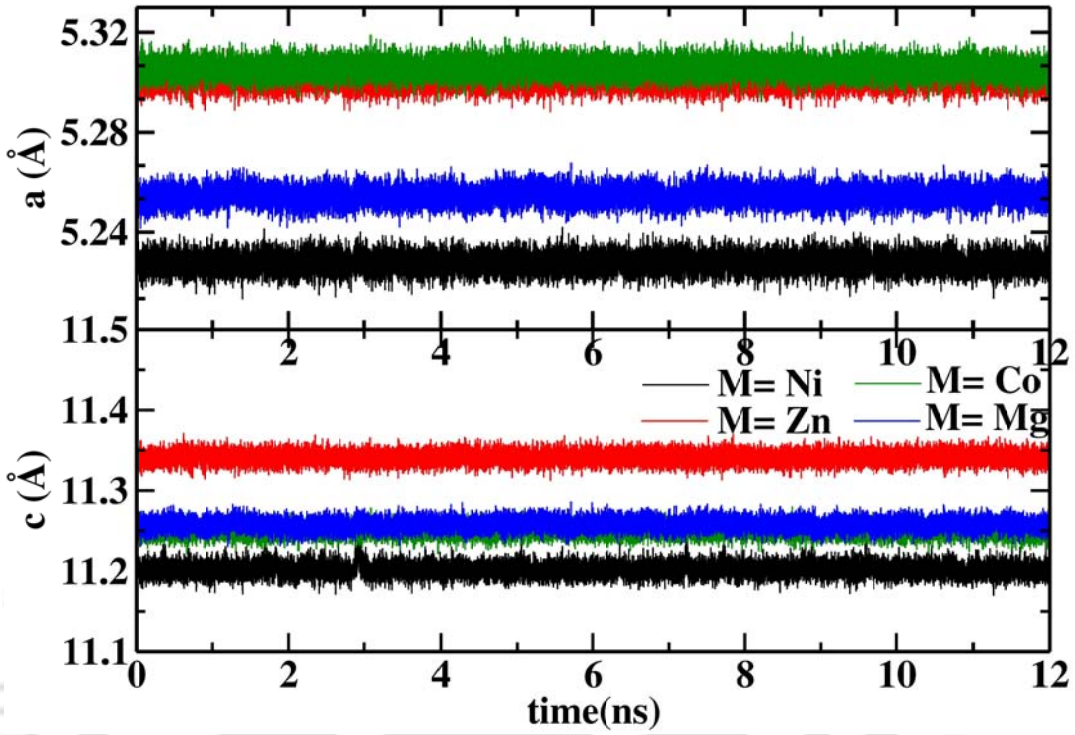

Figure 3-4. The lattice parameters fluctuation with the simulation time during the production phase for all the composition at 600 K.

Table 3.3. Average interatomic distances (in Å) for the Te-O and M-O octahedra (M = Ni, Zn, Co and Mg) from NPT-MD simulations at 300 K.

M	Ni		Zn		Co		Mg	
	Expt.	MD	Expt.	MD	Expt.	MD	Expt.	MD
Te-O	1.993	1.990	1.971	1.990	1.951	1.990	1.945	1.990
M-O	2.035	2.020	2.148	2.070	2.112	2.070	2.105	2.050

For the Ni-containing system the Te-O, Ni-O and O-O RDFs are calculated over the range of 300-800 K (figure 3-4) to demonstrate the stability of the system. Slight reduction in the intensities accompanied by thermal broadening of the peaks is observed with temperature. However the first peaks for the octahedral species remain well resolved, throughout the range, reflecting their sharp coordination with oxygens. These results

demonstrate that proposed interatomic potentials support the experimental structure of $Na_2M_2TeO_6$, where M = Ni, Co, Zn and Mg, over a wide range of temperatures.

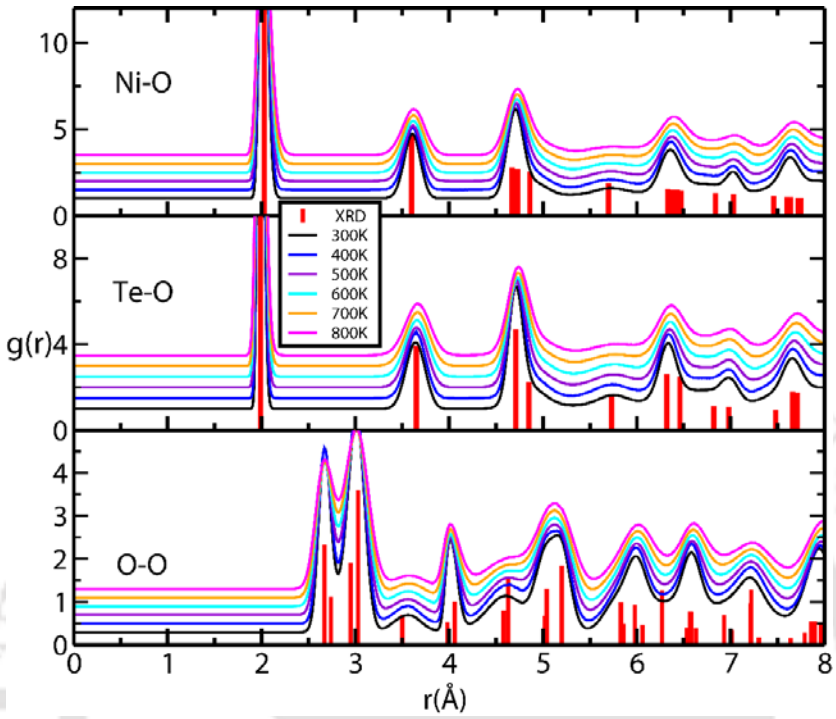

Figure 3-5. The radial distribution function, g(r), between selected ion pairs, Ni-O, Te-O, O-O, for $Na_2Ni_2TeO_6$ over 300-800 K. The vertical bars in red are the corresponding, g(r), based on X-ray structure [34]. The functions are displaced uniformly along Y-axis for clarity.

3.3.2 Ionic Conductivity

The Na^+ ions occupy the interlayers of the polyhedral sheets, and are loosely bound to the framework facilitating ionic conductivity. Evidently the closely packed octahedral layers restrict the Na^+ motion along c-axis of the cell resulting in two-dimensional conductivity. The mean squared displacements (MSD) of the Na^+ is calculated as a function of time are highly an-isotropic when resolved along the cell edges. The MSD of Na^+ along the c-axis converges rapidly due to inpenitrative octahedral framework layers, suggesting a value of about 0.2 Å for their thermal amplitudes. The MSDs of Na^+ parallel to the conducting layer at 600 K is shown in figure 3-6 for all compositions. The MSDs for the $Na_2M_2TeO_6$ show systematic decrease across the series, Ni, Zn, Co and Mg, in qualitative agreement with their measured conductivities. The framework ions, M = Ni, Zn, Co or Mg, Te and O, do not diffuse over the temperature range examined here. The MSDs of the framework species for

the Ni-system at 600 K is shown in the inset of figure 3-5. Following Einstein's relation the self-diffusion coefficient of Na^+ is calculated for the two-dimensional transport as,

$$D = \lim_{t\to\infty} \frac{1}{4Nt} \langle \sum_{j=1}^{N} \left[\vec{r_j}(t) - \vec{r_j}(0) \right]^2 \rangle \tag{3.2}$$

where N is the number of Na^+ in the system, r_j (t) is the position vector of the j^{th} ion at time t and the angular bracket indicates average over several time origins. The ionic conductivity of the system is calculated from the Nernst-Einstein relation,

$$\sigma = \frac{nq^2 D}{k_B T} \tag{3.3}$$

where n is the number density of Na^+ in the system, q -the formal charge of Na^+ (that is, +1|e|), k_B - Boltzmann constant, and T -the temperature in Kelvin. For the Ni-system the conductivity is calculated over 500-800 K from NPT-MD simulations employing equations 3.2 and 3.3. The Arrhenius plots, $log(\sigma T)$ versus inverse of temperature, presented in figure 3-6 shows deviation from linearity, suggesting non-Arrhenius behavior. M = Mg case, shows significant deviation from linearity toward the low temperature. Usually system exhibits less diffusivity at low temperature. Thus, poor statistics is quite common. Over all, the simulation results are in very good agreement with previous experimental observations.

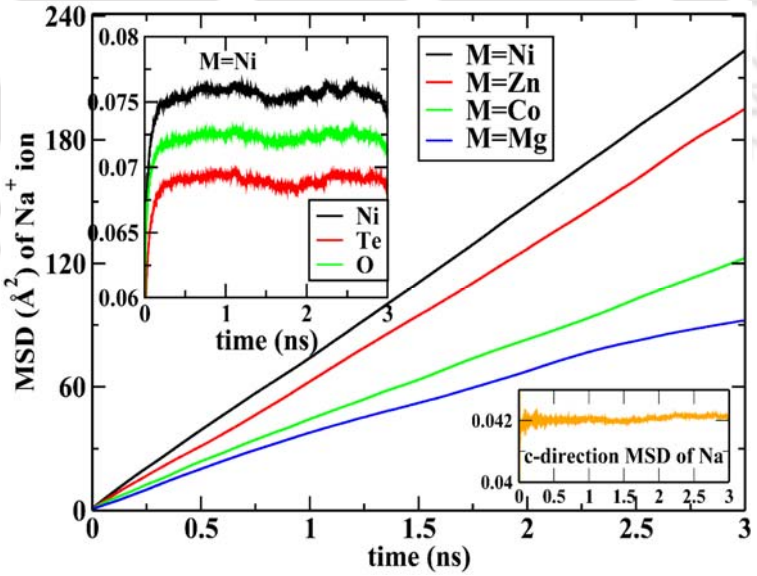

Figure 3-6. The mean square displacement (MSD) of Na^+ ions in $Na_2M_2TeO_6$ from MD simulation at 600 K. MSD of Na^+ along the *c*-direction shown in the inset (bottom-right) demonstrates anisotropic nature of Na^+ transport in the system. The MSDs of the framework species for $Na_2Ni_2TeO_6$ at 600 K is shown in the inset (top-left).

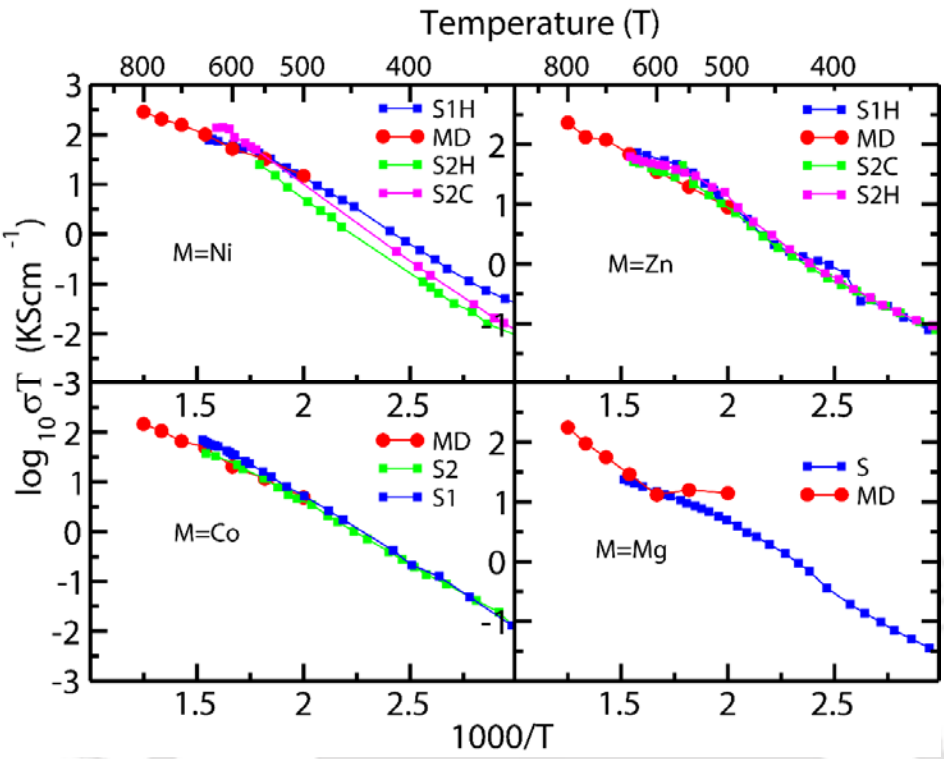

Figure 3-7. Arrhenius plot of Na^+ conductivity for $Na_2M_2TeO_6$, where M = Ni, Co, Zn or Mg, from MD simulation (shown as red dots) over 500-800 K. The experimental data shown are extracted from a high resolution copy of Figure 8 of Evstigneeva et al. [34] S1, S2 are samples numbers, H and C abbreviate heating and cooling cycles as reported in their original experimental report.

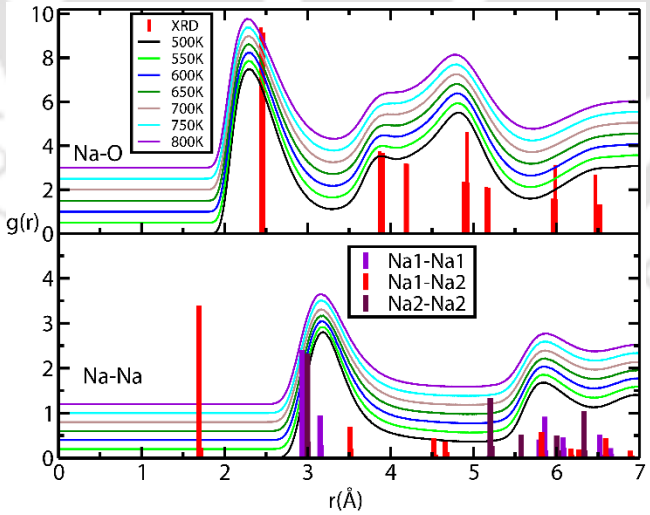

Figure 3-8. The radial distribution functions, g(r), for pairs Na-O (top) and Na-Na (bottom) in $Na_2Ni_2TeO_6$. The distribution of Na-sites, Na1-Na1, Na1-Na2 and Na2-Na2, for the X-ray structure is shown as vertical bars. A few select site-site distances are, Na1-Na1=2.93 Å (1^{st} neighbor), 3.15 Å (2^{nd}), Na2-Na2=3.00 and Na1-Na2=1.69 Å (1^{st}), 3.51 Å (2^{nd}). The functions are displaced uniformly along Y-axis for clarity.

3.3.3 Microscopics of Na^+ transport

The X-ray studies have proposed three Na^+ sites at the interlayer of $Na_2M_2TeO_6$. Labeled Na1, Na2 and Na3, these sites have a multiplicity of 3, 2 and 1, respectively, per interlayer per unit cell. The top and bottom conducting layers are not merged exactly. It shows some angular deviations. All these sites are the center of trigonal-prismatic arrangement of oxygen ions. The octahedral layers include tetrahedral holes formed between two neighboring NiO_6 and a TeO_6 octahedron (see figure 3-1). Na1 site is located mid-way between the two tetrahedral holes from the top and bottom layers. Na2 sites are sandwiched between the triangular faces of NiO_6 octahedra from the top and bottom layers, while Na3 between two TeO_6 octahedra. The calculated Na-O radial distribution functions, g(r), presented in figure 3-7, have broad features owing to the Na^+ diffusion but shows an average coordination of about 6 over 3.2 Å (up to the minimum following its 1st peak). The g(r) of the Na-sites with oxygens (based on the X-ray structure) is shown as a bar-plot. The 1st peak positions of the simulated Na-O g(r) are off by 0.2 Å with respect to the X-ray structure suggesting that the Na^+ ions populate these sites slightly off-centered.

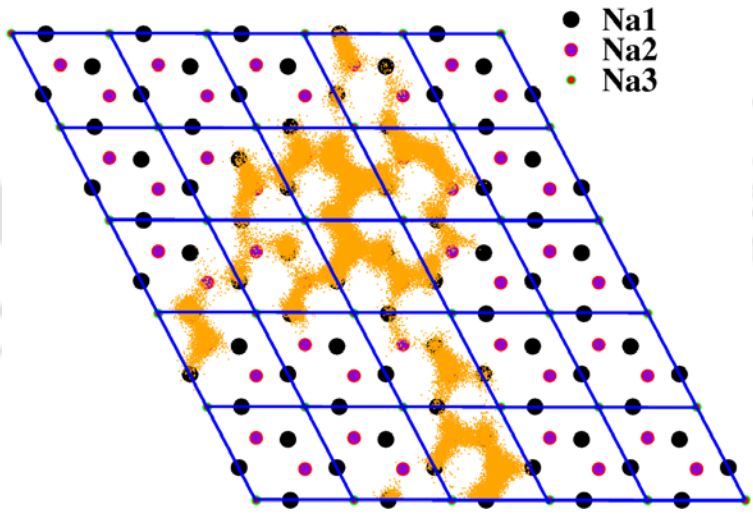

Figure 3-9. The MD trajectories of a randomly picked Na^+ -ion during 5.4 ns at 600 K is shown superimposed over the Na-site distribution.

Employing a spherical cut-off of 0.8 Å the Na^+ counts at the various sites have been estimated from the MD trajectory at 600 K. The estimated populations at Na1 and Na2 sites are roughly 50%, with Na3 measuring practically none. The population estimated are in qualitative agreement with Evstigneeva et al [1]. The Na-Na RDFs in figure 3-7 presents a

liquid-like distribution of the Na^+ -ions. Prominent in the g(r) is the absence of intensity around 1.7 Å corresponding to the nearest Na1-Na2 separation, which suggest that while an Na1-site is occupied by an Na^+ its nearest Na2 locations are vacant, and vice versa. However, simultaneous occupancy and two of two neighboring Na1 sites (at 2.93 and 3.15 Å) and two neighboring Na2 sites (at 3.00 Å) are permitted. The absence of peak around 4.5 - 4.7 Å, which correspond to the 3rd and, 4th Na2-neighbours of a Na1 site, also suggest the strong ion-ion correlation. Similar deduction may be attributed to the low intensity around 5.2 Å corresponding to the separation between two next-neighboring Na2 sites. This intermediate-range correlation of the Na-sublattice is evidently mediated through the Na^+ -ions itself.

The trajectory of a single, randomly picked, Na^+ is displayed superimposed over the various Na-sites the simulation cell for an exposure time of 5.4 ns (see figure 3-9). The Na^+ is seen to develop a well-connected pathway spread across several unit cells over this period. While the Na1 and Na2 sites forms the nodal-points of its trajectory, the Na3 sites are hardly visited. The potential energy of individual Na^+ -ions are calculated as,

$$V_i = \sum_{\substack{j=1 \\ j \neq i}}^{N_t} V_{ij} \tag{3.4}$$

where N_t is the total number of particles in the system, and V_{ij} is the pair wise interaction potential in eq.3.1, such that the total potential energy of the system is,

$$V_t = \frac{1}{2} \sum_{i=1}^{N_t} V_i \tag{3.5}$$

The potential energy of Na^+ -ions is calculated as in eq.3.4, sampled on a fine two-dimensional grid on the ab-plane spanning one unit cell (with all Na^+ coordinates also folded in to a single cell) and averaged over 60,000 configurations over a 12 ns long NVE-MD simulation at 600 K. figure 3-10 (left) displays the potential energy surface (PES) of Na^+ ions thus generated (replicated over 2×2 unit cells for ease of visualization of its continuity). Na2 sites presents the deepest of minima of about -2.65 eV and in basin of about 1 Å radius, while a very shallow minimum of -2.45 eV is observed at Na1. The energies at Na3 are much higher, above -2.32 eV, and do not play any active role in Na^+ transport. The deeper

minima at Na2, being located between two NiO_6 octahedra, can be attributed to the relatively low repulsion Na^+ with Ni^{2+}.

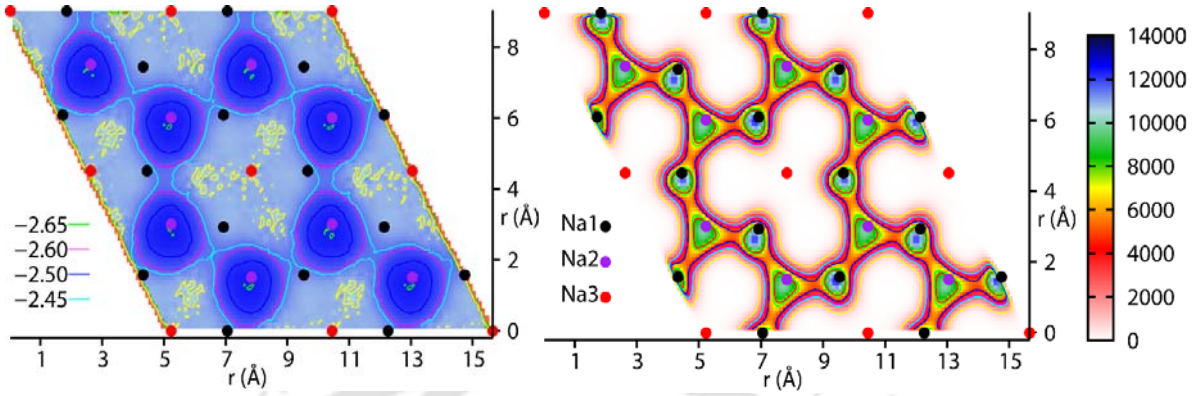

Figure 3-10. (Left-panel)The average individual potential energy (as in eq.3.4), and (right-panel) population profile (un-normalized) of Na^+ ions from MD simulations at 600 K (mapped on to 2×2 unit cells). The locations of the Na-sites, Na1, Na2 and Na3, from X-ray study [34] are marked by the common legends shown in the middle. The population contours reflects that the preferred migration pathway of Na^+ is Na1−Na2−Na1. The qualitative difference between the two distributions are attributed to the ion-ion correlations and entropic contributions (see text for detailed discussion).

profile in Figure 3-10 (left). We shall note that the population in terms of a reaction coordinate, λ, is proportional to the Boltzmann probability [21],

$$P(\lambda) = \frac{e^{-F(\lambda)/k_B T}}{Z} \tag{3.6}$$

where Z is the classical partition function at temperature T, k_B –the Boltzmann constant. The free-energy, $F(\lambda) = U(\lambda) - TS(\lambda)$, where $U(\lambda)$ and $S(\lambda)$ are respectively the internal energy and entropy at temperature T. The reaction coordinate, λ, in the present case may be identified with spatial coordinates on the *a-b* plane, and in the "mean-field" sense the potential energy landscape in figure 3-10 (left-panel) represents the $U(\lambda)$ above. Thus the free-energy profile of the Na^+ ions can be obtained by 'inverting' the population profile shown in figure 3-10 (right-panel). A minima of the potential energy, $U(\lambda)$, or a gain in entropy, $S(\lambda)$, brings about population at the sites. Now the absence of minima in $U(\lambda)$ around the Na1 sites in figure 3-10 (left-panel), despite their significant population, suggests entropic contributions.

A well-developed migration pathway of Na^+ connecting Na1−Na2−Na1 emerges from the population profile in figure 3-10 (right). Insight in to the mechanism of Na^+ transport through Na1–Na2–Na1 sites can be understood invoking the role of ion-ion

correlations, in the backdrop of the topology of Na-site's network. We shall note that there are three Na1 and two Na2 sites available for the two Na^+ ions per interlayer per unit cell of the system. Each Na1 has two neighboring Na2 sites at a distance of about 1.7 Å, and each Na2 has three Na1 neighbors at this distance. We shall, further, note that the ion-ion repulsion prohibits two Na^+ comes closer than 2.5 Å, as is evidenced in the Na-Na g(r) shown in figure 3-8. We shall consider a few representative scenarios to arrange two Na^+ -ions over the five Na-sites (three Na1 and two Na2) available per interlayer per unit cell:

(1) Two Na^+ occupy the two energetically favorable Na2 sites is 'too perfect' an arrangement, leaving no room for Na^+ transport in the system, since an Na^+ hop to any one of the three vacant Na1 neighbors brings it closer to another Na^+ by 1.7 Å (occupying the other Na1 site). In other words this arrangement restricts the accessible configurations and thus entropically unfavorable.

(2) Na^+ -ions occupies a Na1 sites inside the unit cell along with two other Na1 sites on opposite cell edges, such that the total of two Na^+ per interlayer per unit cell is accounted for. This amount to one Na1 site per cell (to be precise, two Na1's on two opposite cell edges contributing half) free for occupancy. The cell marked a) in figure 3-11 provides a schematic representation of this situation. However, this leaves the vacant Na1 site inaccessible as the Na2-site on its path remains unfavorable for the necessary 'stop-over' of an Na^+ due to its shorter distance to one of the occupied Na1 site.

(3) Na1 sites at all the four cell edges occupied, leaving the one inside the cell vacant, also leads to a similar 'road-block' as in scenario 2.

(4) Having exhausted the ordered arrangements, another scenario incorporating some degree of disorder into the Na^+ sub-lattice shall be examined. In figure 3-11, for instance, the unit cell marked *a* has arrangements as in scenario 2 above, and accounts for 2 Na^+ per cell. Starting from scenario 2 a disorder is created, where an Na^+ at the edge, shared by cells *b* and *c* is moved to the edge shared by cells *c* and *d*. Now cell *b* accounts for only one and half Na^+, while cell *d* includes two and half. This arrangement, however, allows for Na^+ hops from Na1 to Na2 sites in cell *b* as shown by arrow numbered 1, and further bifurcations to neighboring Na1 sites. The event can be followed by Na^+ hops shown by arrow labeled 2.

This process can propagate across the lattice and the system gains in terms of entropy, as more sites are now accessible to the Na^+ -ions.

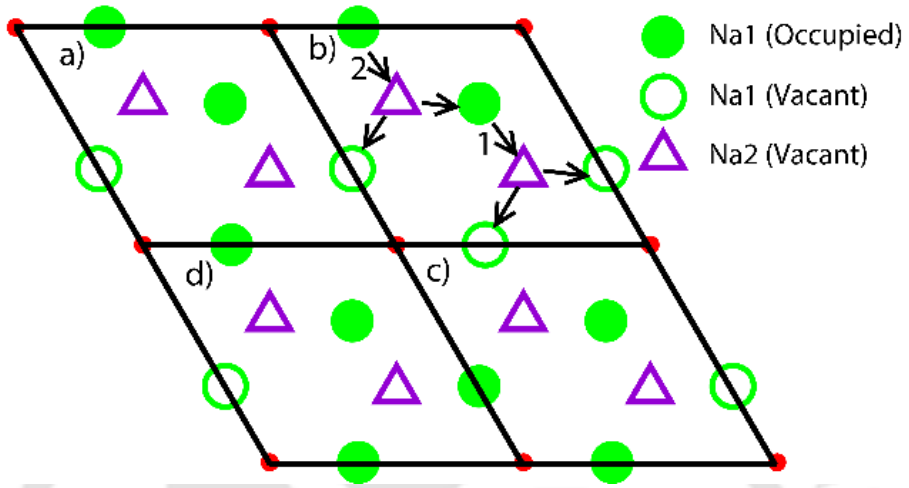

Figure 3-11. Schematic diagram of Na^+ -hoping mechanism in $Na_2Ni_2TeO_6$. The Na1 and Na2 sites in over 2×2 unit cells, marked a − d, per interlayer is shown. The open and filled symbols represent, respectively, the vacant and occupied sites. Refer to text for details.

We shall however note that scenario 4 above is just one of several proposals where disorder of the Na-sublattice increases the entropy (and consequently decreases the free energy as) facilitating Na^+ transport in the system. This explains the significant Na^+ population at Na1 site despite their relatively higher energy. The topology of the network of Na-sites demand that some degree of Na^+ disorder is essential for fast ion transport in $Na_2M_2TeO_6$. Further, the situation also proposes that the high degree of ion-ion correlation prevailing necessitates a cooperative mechanism to be operative in these system.

3.4 Conclusion

An interatomic potential is proposed for $Na_2M_2TeO_6$ –family of fast ion solid, where M = Ni, Co, Zn or Mg. The potential model reproduces the structure, conductivity and population of Na^+ at different Na sites in excellent quantitative agreement with experiments. Fresh insight on the microscopic aspects of ion transport is provided. The results suggest that ion-ion correlation and disordered Na^+ sub-lattice are key features to fast ion transport in these systems.

These observations form the motivation for the more detailed investigation of the role of ion-ion correlation on fast ion transport, discussed in Chapter 4 of the thesis.

Bibliography

[1] M.A. Evstigneeva, V.B. Nalbandyan, A.A. Petrenko, B.S. Medvedev, A.A. Kataev, *Chemistry of Materials* **23** (2011) 1174.
[2] A. Gupta, C. Buddie Mullins, J.B. Goodenough, *J. Power Sources* **243** (2013) 817.
[3] V. Kumar, A. Gupta, S. Uma, *Dalton Trans.* **42** (2013) 14992.
[4] B. Hafskjold, X. Li, *J. Phys. Condens. Matter* **7** (1995) 2949.
[5] M.A. Zendejas, J.O. Thomas, *Phys. Scr.* **1990** (1990) 235.
[6] S. Edvardsson, L. Ojamae, J.O. Thomas, *J. Phys. Condens. Matter* **6** (1994) 1319.
[7] Z. Skotniczny, J. MoScinski, Z. Rycerz, *J. Phys. C: Solid State Phys.* **19** (1986) 4781.
[8] V. Nalbandyan, A. Petrenko, M. Evstigneeva, *Solid State Ionics* **233** (2013) 7.
[9] M. Parrinello, A. Rahman, P. Vashishta, *Phys. Rev. Lett.* **50** (1983) 1073.
[10] K.-i. Nomura, Y. Yokoyama, M. Kobayashi, *Solid State Ionics* **154** (2002) 285.
[11] P. Boolchand, W. Bresser, *Nature* **410** (2001) 1070.
[12] A. Ivanov-Schitz, S. Savvin, G. Mazo, *Crystallogr. Rep.* **54** (2009) 292.
[13] P. Vashishta, A. Rahman, *Phys. Rev. Lett.* **40** (1978) 1337.
[14] P. Vashishta, R.K. Kalia, J.P. Rino, I. Ebbsjö, *Phys. Rev. B* **41** (1990) 12197.
[15] S. Roy, P.P. Kumar, *Phys. Chem. Chem. Phys.* **15** (2013) 4965.
[16] P.P. Kumar, S. Yashonath, *J. Am. Chem. Soc.* **124** (2002) 3828.
[17] S. Roy, P.P. Kumar, *J. Mater. Sci.* **47** (2012) 4946.
[18] J.E. Huheey, E.A. Keiter, R.L. Keiter, O.K. Medhi, *Inorganic chemistry: principles of structure and reactivity*, Pearson Education India (**2006**).
[19] M. Parrinello, A. Rahman, *J. Appl. Phys.* **52** (1981) 7182.
[20] S.J. Plimpton, *J. Comp. Phys.* **117** (1995).
[21] F. Reif, *Fundamentals of statistical and thermal physics*, McGraw-Hill: (**1985**).

Chapter 4

Role of Ion-Ion Correlations on Fast Ion Transport: Molecular Dynamics simulation of $Na_2Ni_2TeO_6$

4.1 Introduction

The present study follows the previous MD simulations of $Na_2Ni_2TeO_6$ discussed in Chapter 3. As mentioned earlier $Na_2Ni_2TeO_6$ consists of layers of edge shared NiO_6 and TeO_6 octahedra, forming honeycomb-like ordering on the *ab*-plane (see figure 4-1). The Na^+ ions intercalate face-shared trigonal-prismatic sites at the interlayers resulting high 2D conductivity (σ = 4-11 S/m) at 300 ^{0}C [1, 2].

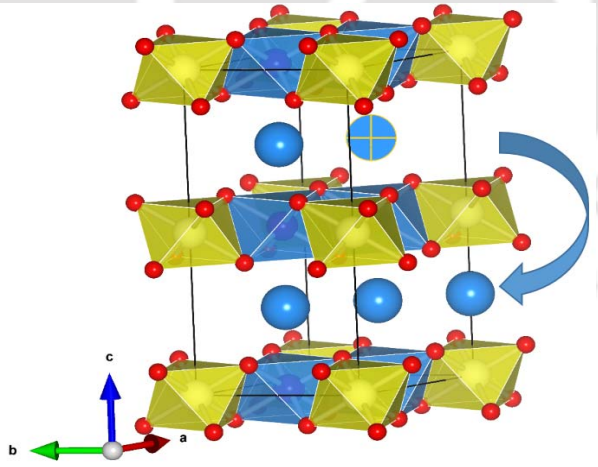

Figure 4-1. Rhombohedral unit cell of the $Na_2Ni_2TeO_6$ structure having edge-shared octahedral layers parallel to the *ab*-plane; NiO_6 –octahedra (blue) and TeO_6-octahedra (yellow), along with the fringe oxygens (red balls) necessary for completing the octahedra are shown. The Na-atoms (blue balls) are shown transferred between interlayers schematically.

The MD simulations presented here investigates the role of ion-ion interaction on transport properties, by tuning the Na^+ concentration at the interlayers. It shall be noted that the variation of conductivity with mobile ion concentration is universally observed in several fast ion conductors. In fact, it is an integral part of traditional experimental strategy to improve the conductivity by making aliovalent substitution around a parent composition, once a framework solid with promising ion transport properties are synthesized [3-8]. However, such aliovalent substitutions also result in change in lattice parameters, and thereby modifying the geometrical bottlenecks for ion transport. A typical example is the NASICONs, $Na_{1+x}Zr_2Si_xP_{3-x}O_{12}$, where the highest ionic conductivity is observed around x = 2, where the c-parameter of the rhombohedral lattice, and bottlenecks for ion transport, attains a maximum [9]. Further, aliovalent substitutions modify the Coulombic barriers for ion migration, depending on the ordering of the framework ions. Thus experimental outcome is in general a combined effect of various factors such as the mobile ion concentration, changes in structural parameters, cationic ordering of the host lattice etc. The present computational study, by virtue of the minimal structural changes on variation in Na^+ loading, provides fresh insights on the exclusive role of ion -ion interaction on transport property.

Table 4.1. Inter ionic potential pair parameters employed in present study.

ion (X)	q_x (C)	σ_x (Å)	$A_{Na\text{-}X}$ (eV)	$A_{X\text{-}O}$ (eV)	$C_{X\text{-}O}$ (eVÅ^6)	$P_{X\text{-}O}$ (eVÅ^4)
Na^+	0.65	1.13	2.298	0.1061	0.00	0.0
Ni^{2+}	1.30	0.69	24.256	3.0846	59.85	31.0
Te^{6+}	3.90	0.70	9.081	3.9098	17.15	11.3
O^{2-}	-1.30	1.21	0.106	0.9260	85.14	0.0

n_{ij} = 11, 9 or 7 respectively for cation-cation, cation-anion and anion-anion.

4.2 Computational Details

MD simulations are performed on $Na_2Ni_2TeO_6$ employing Vashishta-Rahman form of interatomic potential [10, 11],

$$u_{ij}(r_{ij}) = \frac{q_i q_j}{4\pi\varepsilon_0 r_{ij}} + \frac{A_{ij}\left(\sigma_i + \sigma_j\right)^{n_{ij}}}{r_{ij}^{\,n_{ij}}} - \frac{P_{ij}}{r_{ij}^{\,4}} - \frac{C_{ij}}{r_{ij}^{\,6}} \tag{4.1}$$

where q_i is the partial charge and σ_i is the ionic radius of the i^{th} ion. The first term represent the effective Coulombic interaction between ion pairs, i and j, separated by a distance r_{ij}, with ε_0 being the permittivity of the free space. A_{ij}, P_{ij} and C_{ij} are respectively the pre-factors controlling the overlap-repulsion between electron clouds, interactions due to atomic polarization and van der Waals attraction between ion pairs i and j. Notably, the overlap-repulsion term of the potential is softer in nature, with n = 11, 9 or 7, respectively for cation-cation, cation-anion and anion-anion pairs, compared to Born-Mayer (Buckingham) [12] or Lennard-Jones forms [3, 13-15]. An optimized set of parameters for $Na_2M_2TeO_6$ – family of solids, where M=Ni, Co, Zn, or Mg, is reported by us recently. Table 4.1 reproduces the parameters for $Na_2Ni_2TeO_6$, which is subsequently employed in the present study. Note that plausible changes in interatomic potential with local Na^+ concentration is not incorporated due to unavailability of experimental data.

The simulation super-cell comprises of 5×5×2 rhombohedral ($P6_3/mcm$) unit cells of $Na_2Ni_2TeO_6$ containing a total of 1100 ions (200 - Na^+, 200 - Ni^{2+}, 100 - Te^{6+} and 600 - O^{2-}). The structure consists of TeO_6 octahedra sharing edges with the surrounding NiO_6 octahedra, in a hexagonal honeycomb order, forming layers parallel to the ab-plane (see figure 4-1). The super-cell consists of four interlayers, perpendicular to the c-axis, each containing 50 Na^+ ions over the 5×5 unit cells on the *ab*-plane.

As mentioned earlier, present study focuses on the role of ion-ion correlation on the transport of ions in the solid. In order to effect modifications to the ion-ion interactions, while maintaining the overall charge neutrality of the system, we have varied the concentration of the Na^+ at the interlayers. Note that overall charge neutrality of the system is an essential condition for the use of Ewald summation that is typically employed in simulations to ensure the convergence of long-range Coulombic interactions.

Thus starting structures with different number of Na^+, 50+*y*/50-*y*/50+*y*/50-*y*, where *y* is an integer zero to 24 (that is, about 50% of the normal) are prepared− these quartet of numbers represent the number of Na^+ at the four interlayers perpendicular to the *c*-axis, and in the order, over the 5×5 unit cells on the *ab*-plane comprising the simulation super-cell.

The interlayers having different loadings are analyzed separately, which shall be referred to by the number of Na^+ ions confined in the interlayer across the 5×5 unit cells hence forth. Starting from the X-ray positions of the framework ions (Ni, Te and O), and Na^+ ions distributed randomly across the Na1 and Na2 sites identified in the X-ray studies, a series of MD simulations are carried out in the following ensembles:

1. Most of the results presented here are based on a series of micro canonical ensemble nanosecond of six nanoseconds long equilibration velocities of atoms are scaled at intervals to achieve a resulting average temperature of 600 K. The resulting (time averaged) temperatures (over the production phase) in all cases of loadings are well within ±10 K around the aspired value of 600 K. (NVE) MD simulations, allowing all atoms move (dynamic framework). These simulations of twelve nanoseconds duration (of which early six nanoseconds are dedicated to equilibration) are performed at the experimental density. During the first one
2. Isothermal-isobaric ensemble (NPT) MD simulations allowing for changes in shape and size of the super-cell are carried out at 300 K and at 1 atm. pressure. The NPT-MD simulations are of six nanoseconds long, at a time step of 2 femtoseconds. The objectives of these runs are solely to scrutinize the structural stability and changes in lattice parameters (with respect to the experimental values) upon different loadings of Na^+ ions at the interlayer of $Na_2Ni_2TeO_6$.

3. A series of NVE-MD simulations are performed with the framework ions (Ni, Te and O) kept immobile (static-framework) at their X-ray positions, allowing only the Na^+ ions move. These twelve nanoseconds long runs are performed at a desired temperature of 600 K (with the temperatures controlled by velocity-scaling during first one nanoseconds of six nanosecond long equilibration to result an eventual accuracy of ±10 K over the production phase). As discussed in the next section, for the extreme loadings, having above ±30% of Na^+ ions at the interlayer, some degree of bending and sliding of layers are noted in NPT- and NVE- MD runs. The objectives of these static-framework runs are to ensure that the qualitative nature of the results are unaffected with respect to these structural imperfections at extreme loadings.

The temperatures mentioned in the rest of the article are the desired values for NVE-MD runs, in static as well as dynamic framework calculations, which includes a tolerance value

of ±10 K. Ewald summation technique and periodic boundary conditions are employed in all cases. The NPT-MD simulations are performed using LAMMPS (employing a tabular form of the potential in eq. 4.1), and NVE-MD simulations, both in the dynamic and static frameworks, are using our in-house software.

4.3 Results and Discussion

4.3.1 Structure

The $Na_2Ni_2TeO_6$ forms layers of edge shared NiO_6 and TeO_6 octahedra, arranged in a honeycomb order parallel to the ab-plane (figure 4-1). The interlayers of these metal-oxide slabs, having a spacing of about 3.5 Å (measured between oxygen layers), accommodates the charge balancing Na^+ ions. Each unit cell consists of two interlayers, each containing two Na^+ ions per unit cell. Previous MD simulations have shown that, metal-oxide layers are impenetrable, leading to anisotropic conduction of Na^+ in the ab-plane. The present NPT-MD simulations of $Na_2Ni_2TeO_6$ for the various Na^+ loadings produced average cell dimensions and angles close to the normally-loaded, 50/50/50/50-system, and within 0.5%

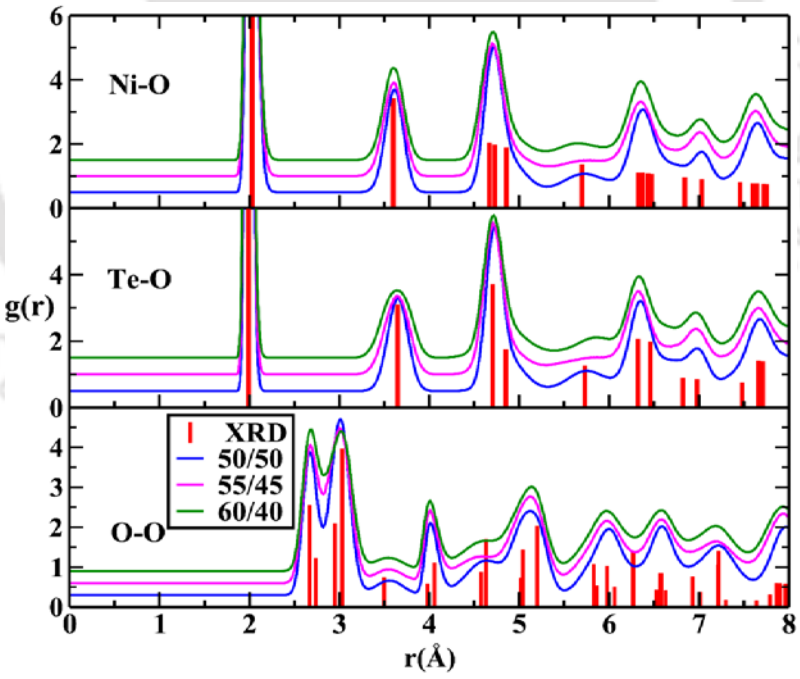

Figure 4-2. The radial distribution function (RDF), g(r), between select ion pairs, Ni-O, Te-O, O-O, of $Na_2Ni_2TeO_6$ for different loadings from NPT-MD simulations at 300 K. The g(r)s calculated for the X-ray structure [33] are shown as vertical bars in red. The functions are displaced uniformly along Y-axis for clarity.

of the experimental values. However, for the extreme loadings having ±30% or more Na^+ ions (that is 65/35/65/35 composition and beyond) some degree of sliding, and bending or undulations of the layers are noted. This prompted us to carry out the series of static framework simulations, and eliminate the role of structural imperfections on transport properties. Table 4.2 provides a comparison of the average cell parameters from NPT-MD simulations at 300 K for the 60/40/60/40, 55/45/55/45 and 50/50/50/50 -loadings. Thus the interlayer spacing are practically insensitive to the loading (except for the structural imperfections at extreme loadings, mentioned above), and thus not a significant factor for the observed changes in the Na^+ diffusivities to be discussed later. The radial distribution functions forms, *g(r)*s, between select ion pairs, Ni-O, Te-O and O-O for these loadings are shown in figure 4-2. The peak positions of these *g(r)*s compares well with the *g(r)*s calculated from the X-ray structure (shown as vertical bars) for the corresponding ion pairs. Also, Ni and Te makes sharp oxygen coordination of six, as expected. Thus the $[Ni_2TeO_6]^{2-}$ framework permits a significant degree of compositional variation of the Na^+ at its interlayers.

Table 4.2. Comparison of the lattice parameters from experiment (at 300 K), calculated from NPT-MD at 300K and their respective percentage (Δ) deviations for systems having variably loaded interlayers, 50/50/50/50 (50/50), 55/45/55/45 (55/45) and 60/40/60/40 (60/40).

Lattice parameters	Expt.	50/50	|Δ|(%)	55/45	|Δ|(%)	60/40	|Δ|(%)
a(Å)	5.207	5.211	0.06	5.226	0.36	5.224	0.30
b(Å)	5.207	5.213	0.10	5.223	0.30	5.224	0.30
c(Å)	11.156	11.163	0.06	11.216	0.53	11.204	0.43
α(degree)	90	90.02	0.02	90.01	0.01	89.96	0.04
β(degree)	90	89.97	0.03	91.28	0.30	89.98	0.02
γ(degree)	120	120.04	0.03	119.95	0.04	119.99	0.01

4.3.2 Ionic Conductivity

Having observed that the $[Ni_2TeO_6]^{2-}$ framework permits up to ±30% variation in the number of Na^+ ions at the interlayers without appreciable structural changes, detailed investigation of Na^+ transport at the interlayers is carried out. For each of the individual

interlayers having different Na^+ loadings the diffusivity of Na^+ is calculated from the mean squared displacement (MSD) versus time, using the Einstein relation,

$$D = \lim_{t\to\infty} \frac{1}{4Nt} \langle \sum_{j=1}^{N} \left[\vec{r_j}(t) - \vec{r_j}(0) \right]^2 \rangle \qquad (4.2)$$

where r_j is the position vector of the j^{th} Na^+ ion, t the period of observation, and N the number of Na^+ ions in a given interlayer. The angular bracket implies averaging over several time origins. The factor of four at the denominator, instead of six, implies two dimensional diffusivity is estimated, as there is no long range motion of Na^+ along the c-axis.

The mean squared displacement of Na^+ ions confined to individual interlayers at 600 K are shown in figure 4-3 for Na^+ loadings over the range of 40 to 60. The corresponding dc conductivity calculated using the Nernst-Einstein relation,

$$\sigma = \frac{Nq^2D}{Vk_BT} \qquad (4.3)$$

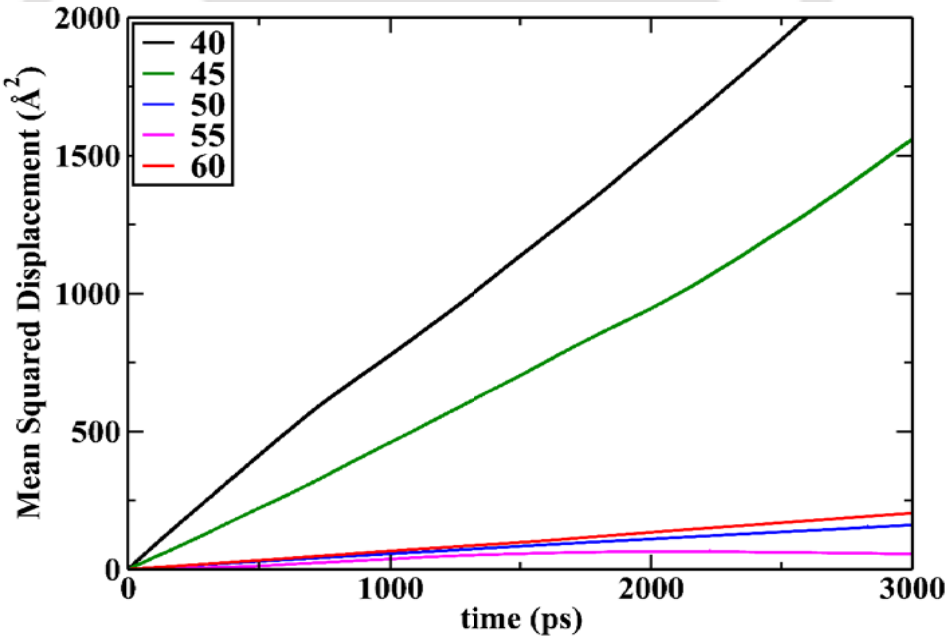

Figure 4-3. The mean square displacement (MSD) of Na^+ ions for a few interlayers having different loadings of Na^+ in $Na_2Ni_2TeO_6$ from NVE-MD (dynamic framework simulations) at 600 K. The legend indicates the number of Na^+ ions per interlayer across 5×5 unit cells on the *ab*-plane.

where N is the number of Na^+ per unit cell in a given interlayer and V is half the unit cell volume (as there are two interlayers per unit cell). q is the formal charge of Na^+ (+1|e|), k_B –

the Boltzmann constant, and T – the temperature in Kelvin. The diffusion coefficients from dynamic (DF) and static (SF) frameworks, as well as ionic conductivity, at 600 K – all relative to their respective normally-loaded interlayer (having 50 Na^+ ions), are shown in figure 4-4 as a function of Na^+ loadings. The Na^+ diffusivities of the normally-loaded interlayer at 600 K are estimated to be 0.014 and 0.044 $Å^2$/picosecond, respectively for the dynamic (DF) and static (SF) -frameworks. This, roughly three-fold enhancement of Na^+ diffusivity in the static framework (SF), is fairly uniform across the composition range. A qualitative understanding of this enhancement may be derived noting that in the static framework the Na^+ ion recoils off the framework more vigorously than in the dynamic case (this can be argued by drawing the parallel to an elastic, head-on collision of two masses where the recoil velocity of the lighter particle (analogous to Na^+) increases with mass of the other particle (analogous to the static framework). This high recoil velocity translates to higher cage-frequency of oscillation of the Na^+ ions. A higher cage-frequency (attempt-frequency) enhances the diffusivity of the ions.

The Na^+ diffusivity in the static and dynamic framework, as well as the conductivity (calculated for the dynamic framework) shows remarkably anomalous behavior with peak values around the loading state of 40 (figure 4-4). Thus a reduction in the Na^+ concentration at the interlayers by about 20% (from the normal loading state of 50) enhances the conductivity through nearly an order of magnitude. The observed trend suggest that further reduction does not favor the Na^+ transport. Since negligible changes in lattice parameters are observed over ± 30% variation in the number of Na^+ ions (that is, over 40 to 60 Na^+-loadings) at the interlayers the observed effect is attributed largely to the changes in ion-ion interaction due to the change in Na^+ concentration.

4.3.3 Microscopic Na^+ Transport

There are three crystallographically different Na^+ sites, named Na1, Na2 and Na3, are identified in the X-ray studies of Evstigneeva et al. [1]. These sites respectively have multiplicities of three, two and one at each interlayer per unit cell. All of these three sites

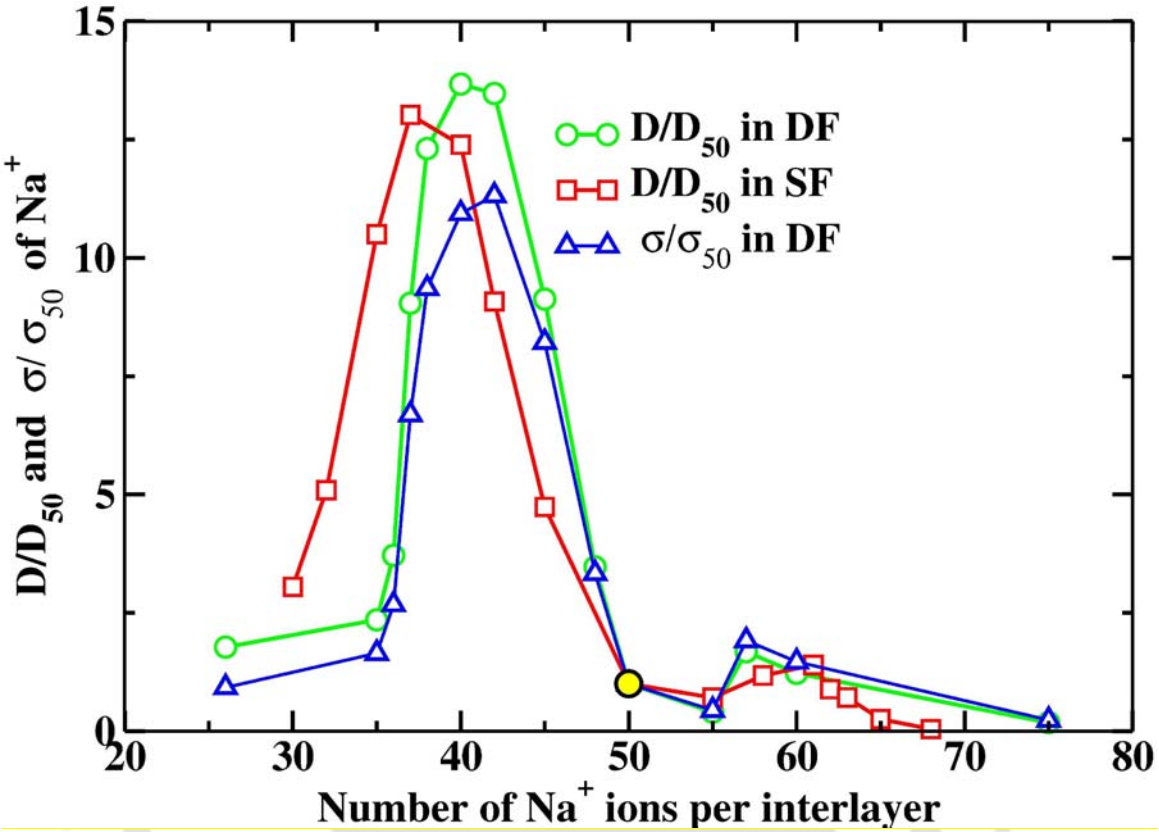

Figure 4-4. The Na^+ diffusion coefficients (D) and conductivity (σ) in the dynamic framework (DF) for variably loaded interlayers are shown relative to their respective values of the normal interlayer (having 50 Na^+ ions, marked by the yellow circle), from NVE-MD simulations at 600 K. The diffusivities in the static (SF) frameworks relative to its normal interlayer (D_{50} = 0.014 and 0.044 $Å^2$/ps for dynamic and static framework respectively) are also shown.

have a trigonal bi-prismatic arrangement of oxygens, three from the top and three from the bottom metal-oxide layers as shown in figure 4-5. For the Na2 site the three oxygens above and below are the triangular faces of two NiO_6 octahedra from the top and bottom layers, while for the Na3 site the triangular faces are of TeO_6 octahedra on top and bottom layers. The Na1 site is aligned along the tetrahedral voids, due to the face sharing of the polyhedra, and has two Ni and one Te neighbors each from top and bottom layers.

The potential energy of individual Na^+ -ions are calculated as,

$$u_i = \sum_{\substack{j=1 \\ j \neq i}}^{N_t} u_{ij} \tag{4.4}$$

where N_t is the total number of particles in the system, and u_{ij} is the interaction potential in eq.4.1, such that the total potential energy of the system is,

$$u_t = \frac{1}{2}\sum_{i=1}^{N_t} u_i \tag{4.5}$$

The 6 ns trajectories from NVE-MD simulations at 600 K are analyzed for energetics, site occupancy and migration pathways of Na^+. The potential energy of the individual Na^+ ions (due to the rest of the ions in the system), averaged over the MD trajectory and over all the Na^+ ions in a given interlayer, is mapped on to the ab-plane. The potential energy surface (PES) thus generated, spanning 2×2 unit cells, is shown in figure 4-6 for three different Na^+ loadings, namely, 40, 50 and 60. The right column displays the corresponding population of Na^+ ions, again, mapped over 2×2 unit cells on the ab-plane. Locations of the Na^+ sites, Na1, Na2 and Na3, are also marked in the backdrop.

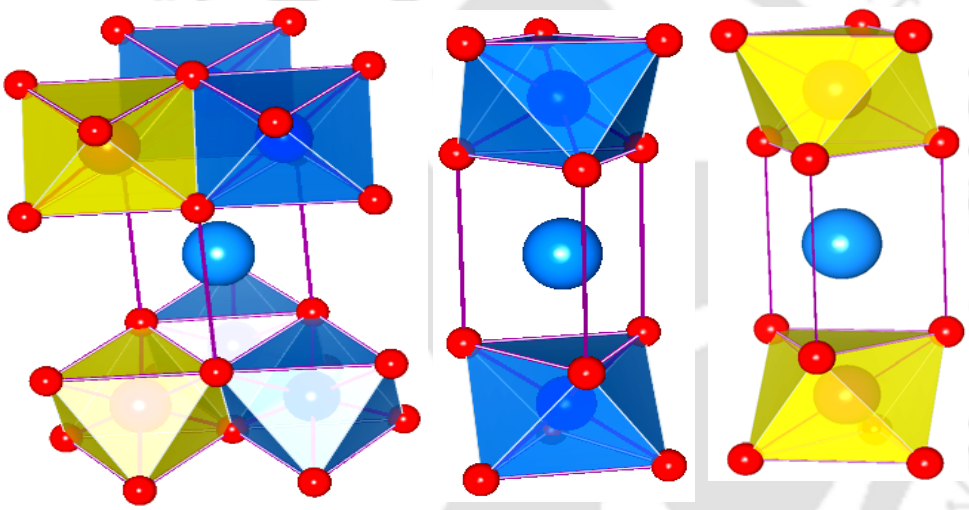

Figure 4-5. The polyhedral environments of the different Na sites, Na1, Na2 and Na3 (from left to right). NiO_6 octahedra are shown in blue and TeO_6 octahedra in yellow.

In the under-loaded interlayer (having 40 Na^+ ions, that is, 20% lower concentration) a deep potential minima of about -2.76 eV is observed at the Na2 site, with no appreciable minimum at the Na1 site. The population of Na^+ ions shown in the top right column also follow the trend, with an estimated 70% of Na^+ ions at the Na2, leaving the Na1 and Na3 sites practically unvisited. We shall note that owing to the presence of the two Te^{6+} neighbors at a distance of 2.78 Å the Na3 site is expected to be of higher energy for an occupying Na^+ ion, and thus least preferred. It turns out that the Na2 site that has two Ni^{2+} neighbors at a distance of 2.78 Å have the lowest energy among the three. The Na1 site is intermediate in energy due to its two Te^{6+} and four Ni^{2+} neighbors, but at a larger distance of

3.32 and 3.26 Å respectively. The migration pathway of Na^+ ions in this case connects two neighboring Na2 sites directly.

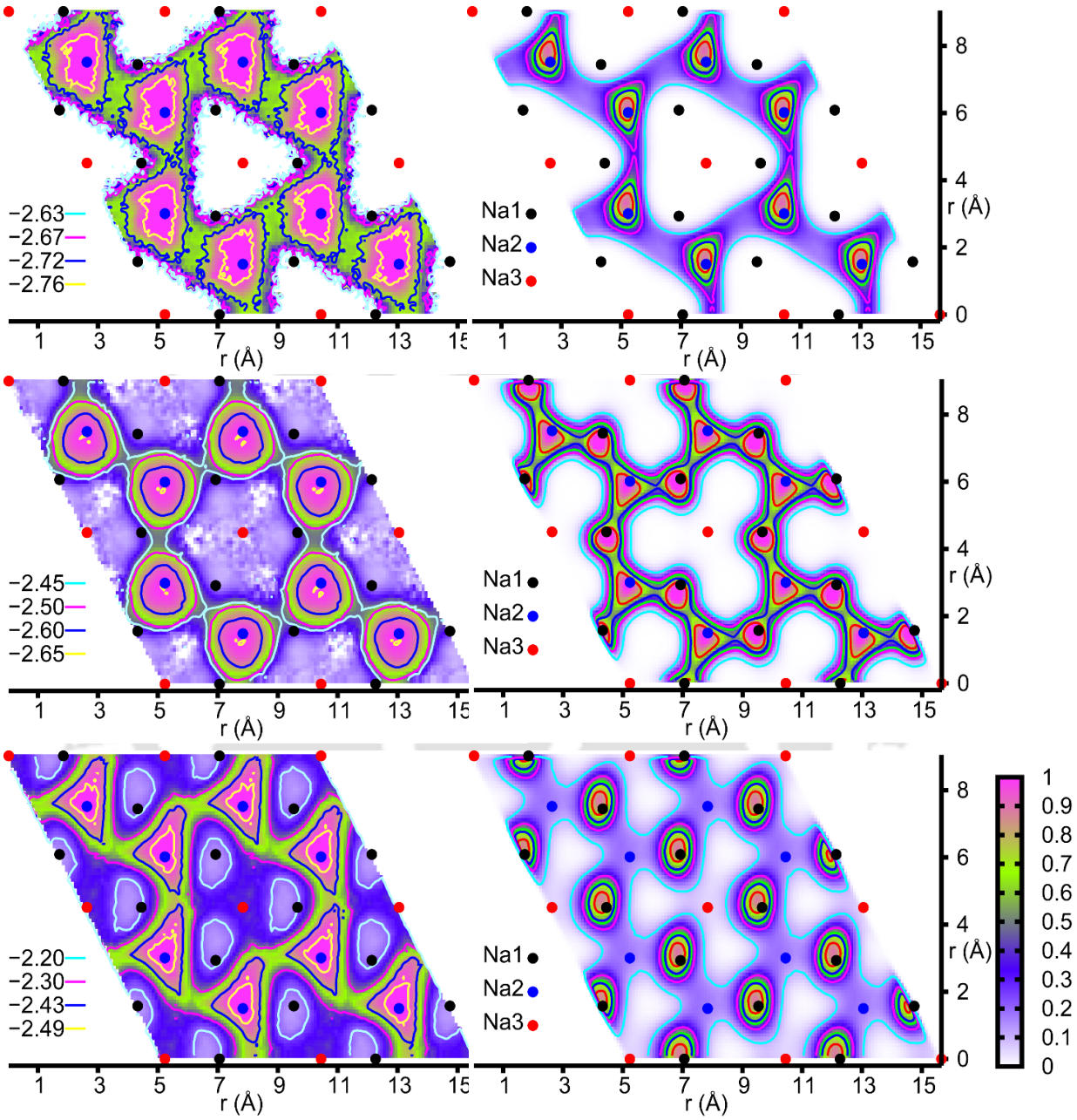

Figure 4-6**.** From top to bottom, (left-column) the potential energy profile in eV (as in eq. 4.4), and (right-column) population profile of Na^+ ions from NVE-MD (dynamic framework simulations) at 600 K (mapped on to 2×2 unit cells), for the under-loaded, normal and over-loaded interlayers, having respectively 40, 50 and 60 Na^+ ions. The population profiles are normalized with respect to their respective peak values, and the color map on extreme right is common to all loadings. The locations of the Na-sites, Na1, Na2 and Na3, from X-ray study are marked by the common legends shown in the middle.

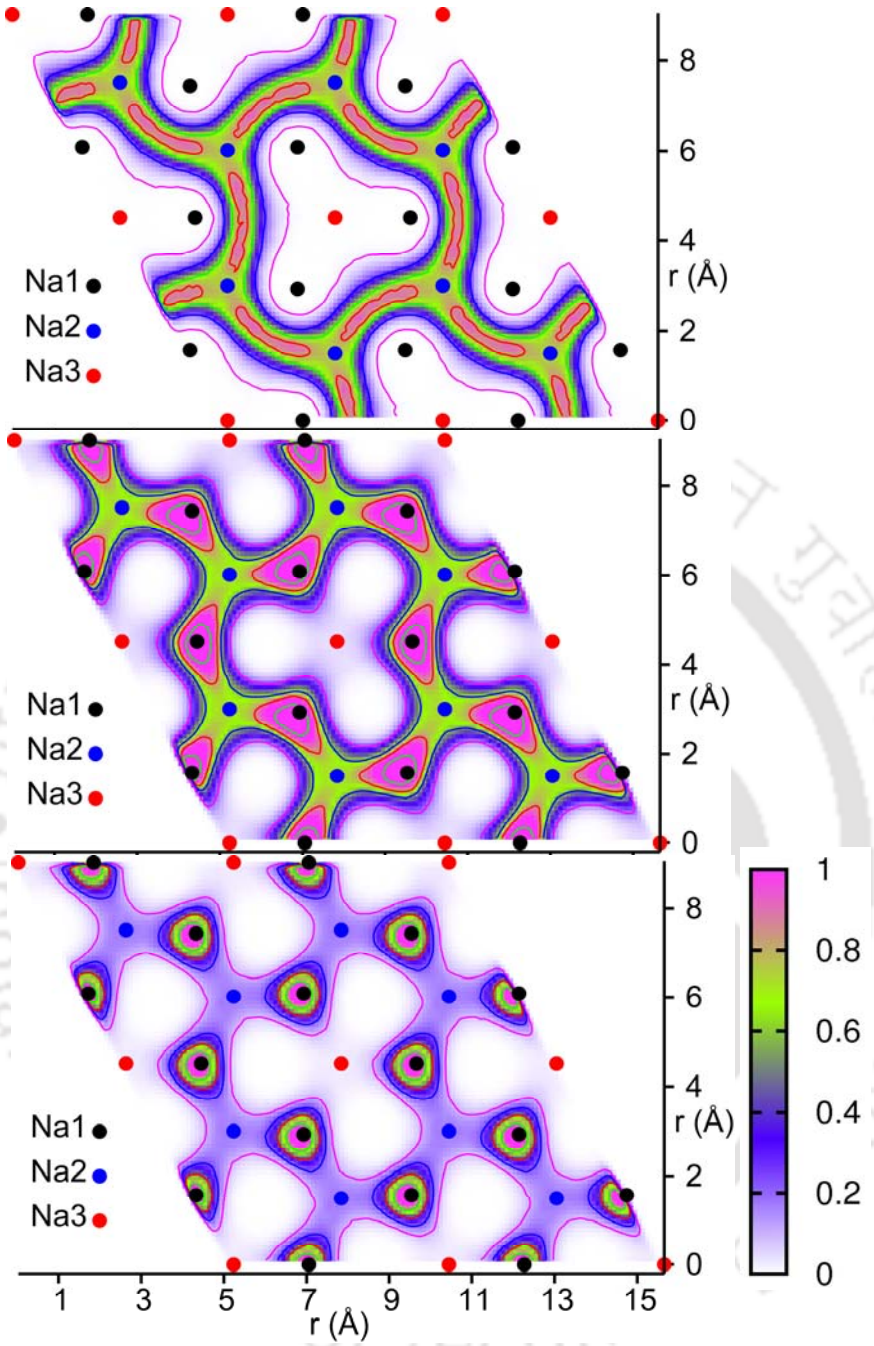

Figure 4-7**.** From top to bottom, the population profile of Na^+ ions from NVE-MD (rigid framework simulations) at 600 K (mapped on to 2×2 unit cells), for the under-loaded, normal and over-loaded interlayers, having respectively 40, 50 and 60 Na^+ ions. The population profiles are normalized with respect to their respective peak values, and the color map on extreme right is common to all loadings. The locations of the Na-sites, Na1, Na2 and Na3, from X-ray study are marked by the common legends shown in the middle.

The PES for normal-loaded interlayer (having 50 Na^+ ions) too shows a deep minimum at the Na2 sites and hardly any minimum at the Na1 site. But the population

profile (middle, right column) depicts a contrasting picture, where in Na1 and Na2 sites have nearly matching occupancy. The preferred migration pathway now connects nearby Na1 and Na2 sites. The overloaded interlayer (having 60 Na^+ ions, of 20% higher concentration) still has the Na2 sites offering the lowest energy, at about -2.49 eV, now higher by 0.27 eV compared to the under-loaded case. Interestingly, the population at Na2 is very low at 12%, and Na1 accommodates most Na^+ ions at a given instant despite being energetically unfavorable. The Na3 sites still remain scarcely visited. The preferred migration channel for the Na^+ remain Na2-Na1-Na2, though much less traversed in comparison with the normal-loading agreeing with the low conductivity calculated.

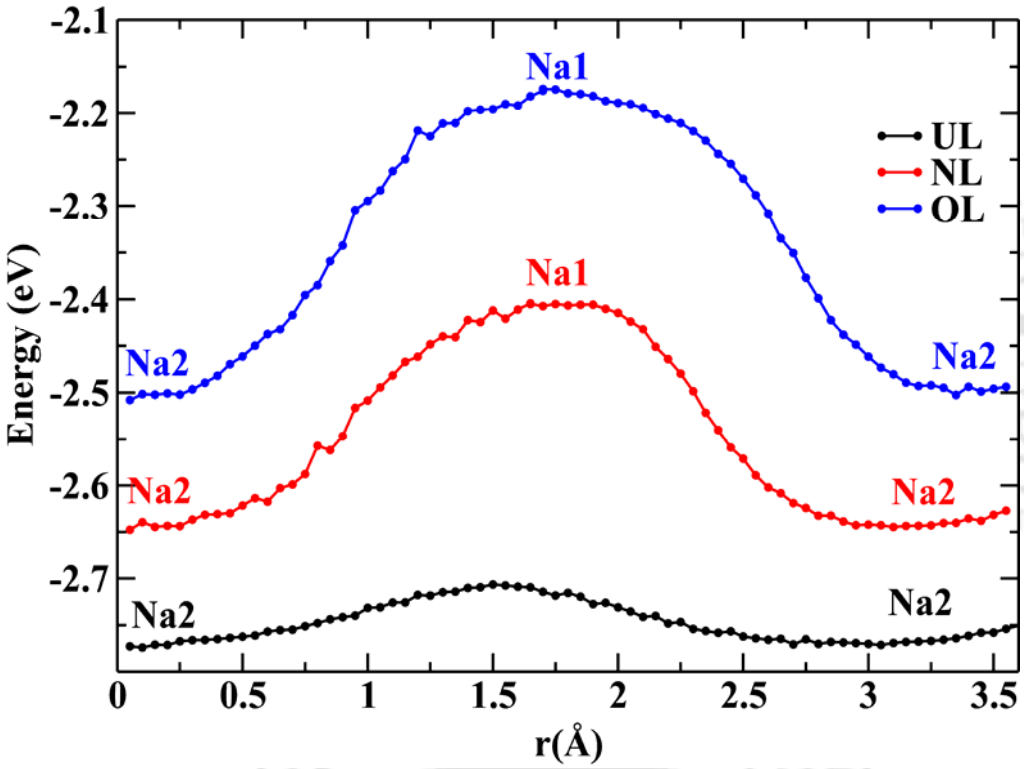

Figure 4-8. The average potential energy barriers (eq. 4.4) for Na^+ hops from an Na2 to a neighboring Na2 site for under loaded (UL), normal loaded (NL) and over loaded (OL) cases from NVE-MD simulations at 600 K. The potential energies are sampled along the approximate migration path (marked by dotted lines on the population profile shown on right-column of figure 4-6) and projected along the line joining the Na2 sites.

The population profile of the conduction layer having 40, 50 and 60 Na^+ ions are displayed in figure 4-7 for the rigid framework model. The population channels are connected Na2 to Na2 for under loaded case where Na1 does not play any role. On contrast, the channels are connected as Na1-Na2-Na1 for both 50 and 60 loaded interlayer. All three

cases, the Na3 sites are forbidden. Thus, the population profile supports the qualitative agreement as obtained from the dynamical framework model.

The above observations can be summarized as follows. In the under-loaded interlayer the Na^+ ions are largely guided by the framework as the Na^+ - Na^+ repulsion is marginal owing to low concentration. The populations and pathways of Na^+ migration are dictated solely by the potential energy landscape. In the normal-loaded interlayer the Na^+ - Na^+ interactions are more significant, and their average energies are higher (more towards the positive). The ions now start exploring higher energy regions of the landscape in an effort to avoid each other, and populates energetically less favorable sites (Na1). As noted in our previous study Na^+ ions keeps themselves away by more than 2.5 Å (see figure 4-10), and holds good for all the loadings examined presently as well. This forbids simultaneous occupation of neighboring Na1 and Na2 sites (which are only about 1.67 Å away).

Populating the higher energy sites gains the system in terms of entropy, owing to the additional configurations now accessible, or in other words, to the greater disorder. As detailed in our earlier study, as the number of Na2 sites and Na^+ ions being equal in the normal-loaded interlayer (two in an interlayer per unit cell), a disordered Na^+ sub-lattice is imperative for their transport in this system. Upon further loadings (60 –loading corresponds to 2.4 Na^+/unit cell/interlayer) the Na^+ ions, now in excess of the comfortable Na2 sites (2 Na^+/unit cell/interlayer), opts for Na1 sites that are more in number (3 Na^+/unit cell/interlayer). In fact, any appreciable occupancy at Na2 is unfavorable as this brings them closer to one or more Na^+ ions occupying neighboring Na1 sites. Thus, with the increase in concentration of mobile ions, ion-ion repulsions turnout to be an important factor in controlling the site occupancies and migration path of ions. Consequently, ion transport is dictated more and more by the entropic factors, than energetic considerations.

4.3.4 Hop Mechanism

The mechanism and time scales of ion hops in the lattice can be deduced from the self-part of the van Hove correlation function $G_s(r,t)$, given by,

$$G_s(r,t) = \frac{1}{N}\sum_{i=1}^{N}\langle \delta(r - |\, r_i(t) - r_i(0)\,|)\rangle \tag{4.6}$$

where N is, in general, the number of Na^+ ions in the system (in the present case the number of Na^+ ions in aparticular interlayer), $r_i(t)$ – refers to the position of the ion after a delay time t, and δ – the Dirac delta function. $G_s(r;t)$ describe the probability distribution that an ion initially at the origin $t = 0$ is found at a distance r after a time t. Figure 4-9 shows the Na^+ distributions for the under-loaded (40 Na^+ ions/interlayer/simulation super-cell), normal and over-loaded cases. In the under case (left-panel) the $G_s(r;t)$ at a delay time of 1 pico-second suggest the distribution just at the onset of developing the second peak. At a delay time of 20 pico-seconds a the fully developed second peak around 3.14 Å, corresponding to the nearest neighbor distance of two Na2 sites, is evidenced. The distribution shifts to the larger distances with considerable spread at longer times as the Na^+ ions diffuses away from the original site.

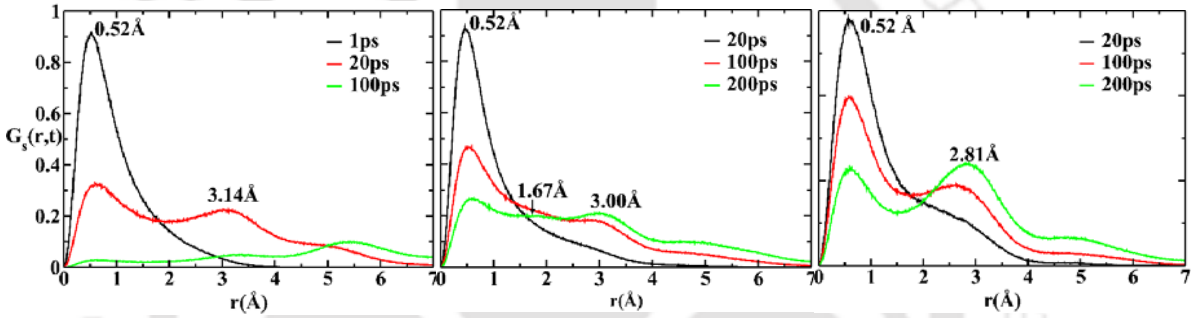

Figure 4-9. The self-part of van Hove correlation function of Na^+ ions for the three representative cases, under-loaded (left), normal (middle) and over-loaded (right) interlayers are shown (from dynamics framework NVE-MD at 600 K).

For the normal-loaded case (50 Na^+ ions/interlayer/simulation-super-cell) shown in the middle-panel of figure 4-9 the residence time of the Na^+ ions is larger and the second peaks starts developing around 20 picoseconds consistent with its one order lower diffusivity compared to the under-loaded case. In this particular case the emergence of a peak at around 1.67 Å signify Na^+ hops between neighboring Na1-Na2 sites, also by virtue of their comparable population. In the over-loaded case (60 Na^+ ions/interlayer/simulation-super-cell) the time scales of Na^+ hops are similar to the normal-loaded interlayer consistent with their comparable Na^+ diffusivity. The distinction, however, is absence of the peak around 1.67 Å. Though Na1-Na2-Na1 forms the preferred migration channel in this case, the absence of the peak and the low population of Na2 sites, suggest Na^+ ions makes only a brief stopover at the Na2 sites before proceeding to the next Na1 sites.

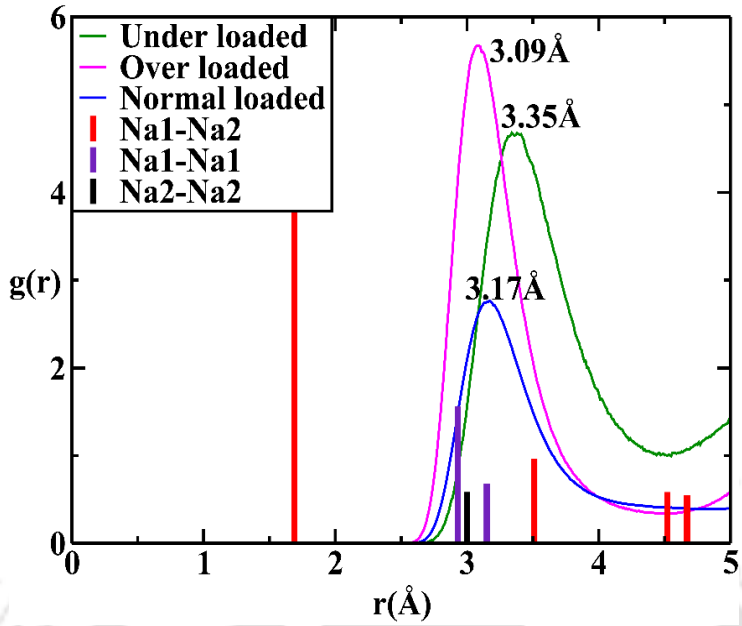

Figure 4-10. The radial distribution functions, g(r), for pair Na-Na for three interlayers such as under loaded, over-loaded and normal loaded in $Na_2Ni_2TeO_6$ from NVE-MD (dynamic framework simulations) at 600 K. The Na1-Na1, Na1-Na2 and Na2-Na2, for the X-ray structure [33] is shown as vertical bars.

4.4 Conclusion

The role of ion-ion correlation on Na^+ transport in $Na_2Ni_2TeO_6$ is examined employing molecular dynamics simulation. The Na^+ diffusivity and conductivity are found to vary by well over an order of magnitude depending on the Na^+ content at the interlayers of $Na_2Ni_2TeO_6$. It is observed that 20% lower concentration of Na^+ in the system is optimal to maximize the ionic conductivity in the system. This is almost entirely attributed to ion-ion correlations, as the present study, by design, is devoid of other contributing factors such as lattice expansion and Coulombic barriers due to aliovalent substitution in the framework.

The Na2 sites located between two NiO_6 octahedra on top and bottom metal-oxygen layers is found to be of lowest energy across the range of ±20% around the standard Na^+ composition. At low concentrations of mobile Na^+ ions at the interlayer, the populations follow the energetic comfort of the framework and migration channels involve direct transfer between lowest energy Na2 sites. With the increase in concentration of Na^+, Na1 sites that are energetically less favorable starts populating, and the migration channels connecting Na2-Na1-Na2 emerge. The rigid framework model also shows the above results

satisfactorily The gradual evolution of the Na^+ population in favor of sites that are energetically less favorable but higher in multiplicity suggest the switching from an energy driven to entropy driven mechanism with Na^+ concentration.

Bibliography

[1] M.A. Evstigneeva, V.B. Nalbandyan, A.A. Petrenko, B.S. Medvedev, A.A. Kataev, *Chem. Mater.* **23** (2011) 1174.
[2] R. Berthelot, W. Schmidt, A.W. Sleight, M.A. Subramanian, *J. Solid State Chem.* **196** (2012) 225.
[3] A. Ivanov-Schitz, S. Savvin, G. Mazo, *Crystallogr. Rep.* **54** (2009) 292.
[4] M. Razmkhah, M.H. Mosavian, F. Moosavi, *Int. J. Hydrogen Energy* **39** (2014) 8437.
[5] K. Arbi, M. Hoelzel, A. Kuhn, F. García-Alvarado, J. Sanz, *Inorg. Chem.* **52** (2013) 9290.
[6] K. Arbi, J. Rojo, J. Sanz, *J. Eur. Ceram. Soc.* **27** (2007) 4215.
[7] K. Saranya, C. Deviannapoorani, L. Dhivya, S. Ramakumar, N. Janani, R. Murugan, *Mater. Lett.* **77** (2012) 57.
[8] B. Hafskjold, X. Li, *J. Phys. Condens. Matter* **7** (1995) 2949.
[9] P.P. Kumar, S. Yashonath, *J. Phys. Chem. B* **106** (2002) 7081.
[10] P. Vashishta, A. Rahman, *Phys. Rev. Lett.* **40** (1978) 1337.
[11] P. Vashishta, R.K. Kalia, J.P. Rino, I. Ebbsjö, *Phys. Rev. B* **41** (1990) 12197.
[12] G. Lewis, C. Catlow, *J. Phys. C: Solid State Phys.* **18** (1985) 1149.
[13] M. Parrinello, A. Rahman, P. Vashishta, *Phys. Rev. Lett.* **50** (1983) 1073.
[14] K.-i. Nomura, Y. Yokoyama, M. Kobayashi, *Solid State Ionics* **154** (2002) 285.
[15] P. Boolchand, W. Bresser, *Nature* **410** (2001) 1070.

Chapter 5

Molecular Dynamics Study of Li ion transport in $Li_{1+x}Al_xTi_{2-x}(PO_4)_3$ System (0.0<x<0.67)

5.1 Introduction

NASICON-type materials are particularly attractive for battery applications owing to its high three dimensional ionic conductivity, as well as high thermal and chemical stability [1]. After the pioneer work by Hong [2] and Goodenough *et al.* [3], a large number of studies have been carried out in search of better electrolytes within this class of materials [1, 4]. NASICONs are well known for their stability against variety of ion substitutions in its polyhedral framework [1]. Generalized formula of NASICONs can be written as $AMM'P_3O_{12}$ where the site "A" typically can be replaced by monovalent alkali ions (Li^+, Na^+, K^+, Rb^+, and Cs^+), and alkaline earth ions (Mg^{2+}, Ca^{2+}, Sr^{2+}, and Ba^{2+}) etc. The M and M′ sites can accommodate divalent (Zn^{2+}, Cd^{2+}, Ni^{2+} etc.), trivalent (Cr^{3+}, Al^{3+}, In^{3+} etc.) tetravalent (Ge^{4+}, Ti^{4+}, Sn^{4+}, Hf^{4+}, Zr^{4+} etc.), and pentavalent (V^{5+}, Nb^{5+}, Ta^{5+} etc.) cations. Phosphorous sites can also be replaced by Si or As. Several factors have been proposed to be responsible for high ionic conductivity of these materials such as, (a) open framework structure facilitating interconnected, low barrier channels for cations, (b) weak framework alkali interactions relative to electrostatic interactions between neighboring alkali ions, [5] etc.

Recently, Arbi *et al.* [6, 7] have reported that the optimum incorporation of Li in the system, $Li_{1+x}Al_xTi_{2-x}(PO_4)_3$ (LATP), a NASICON type material, wherein partial substitution (x = 0.30) of Ti^{4+} by Al^{3+} enhances the ionic conductivity by two-three orders of magnitudes at room temperature. The enhancement in conductivity near x = 0.30 is not well understood so far [8-15]. Based on previous experimental, and theoretical or computational studies several factors contributing to the fast ion transport in this system could be inferred,

1. Size of the mobile ion and bottlenecks for ion transport, imposed by the framework, could play a critical role in fast ion conduction. Generally larger bottlenecks help faster ionic movement as reported in the studies of $LiM_2(PO_4)_3$ (M = Ge, Ti, Sn, Hf and Zr etc) [10, 16]. On the contrary, Kummer reported that in β-alumina the Na^+ and Ag^+ exhibits the highest conductivity than smaller Li^+ ions [17]. A theoretical explanation to this phenomenon rendered by Kumar and Yashonath who predicted an optimal ion size, opposed to smaller size, for highest mobility, based on MD simulation of NASICON systems [18].
2. Optimal mobile ion density could also be responsible for high ionic conductivity [12]. For instance, the conductivity enhancement in $Na_{1+x}Zr_2Si_xP_{3-x}O_{12}$, at $x = 2$ composition [4, 19, 20] could be a result of this optimal concentration or opening up of bottleneck size due to lattice expansion. One of the proposals is that the high ion-ion correlation between mobile ions, which in turn depend on the mobile ion concentration, was proposed to be the reason for high ionic conductivity [21, 22]. In our previous study, discussed in chapter 4, we have observed in chapter 4 that an optimal Na^+ concentration can enhance the conductivity by an order of magnitude at the interlayers of $Na_2Ni_2TeO_6$.
3. Roy and Kumar [23] have recently studied the influence of Si/P ordering on the conductivity of $Na_3Zr_2Si_2PO_{12}$. There are six basal planes perpendicular to *c*-axis and each plane consists of three tetrahedra per unit cell. Three framework structures with different Si/P ordering are studied. First, two Si^{4+} and one P^{5+} in each plane are placed. The second one where two planes made of SiO_4 tetrahedra sandwiching one plane made of PO_4 tetrahedra. The third structure where Si^{4+} and P^{5+} has placed randomly at the Si/P sites. The conductivity was noted to vary by more than one order of magnitude depending on the Si/P order in the structure. The study suggests the significance of the framework cationic order in conductivity with aliovalent substitutions. Experimentally, such orders could be possible depending on the sintering temperature and duration. This possibly explains the large variance in the reported ionic conductivities by different groups.

In the absence of detailed microscopic structural and dynamical properties of the system, the factors responsible for the variation in the conductivity with Li^+ content in these

Table 5-1. $R\bar{3}c$ structural details of the system LATP.

Atom	Wyckoff position	x/a	y/b	z/c
Li1	6b	0.000	0.000	0.000
Li2	18e	-0.280	0.000	0.250
Li3	36f	0.050	0.290	0.070
mid-Li	36f	0.025	0.184	0.001
Ti, Al	12c	0.000	0.000	0.142
P	18e	0.290	0.000	0.250
O1	36f	0.185	0.996	0.190
O2	36f	0.188	0.164	0.081

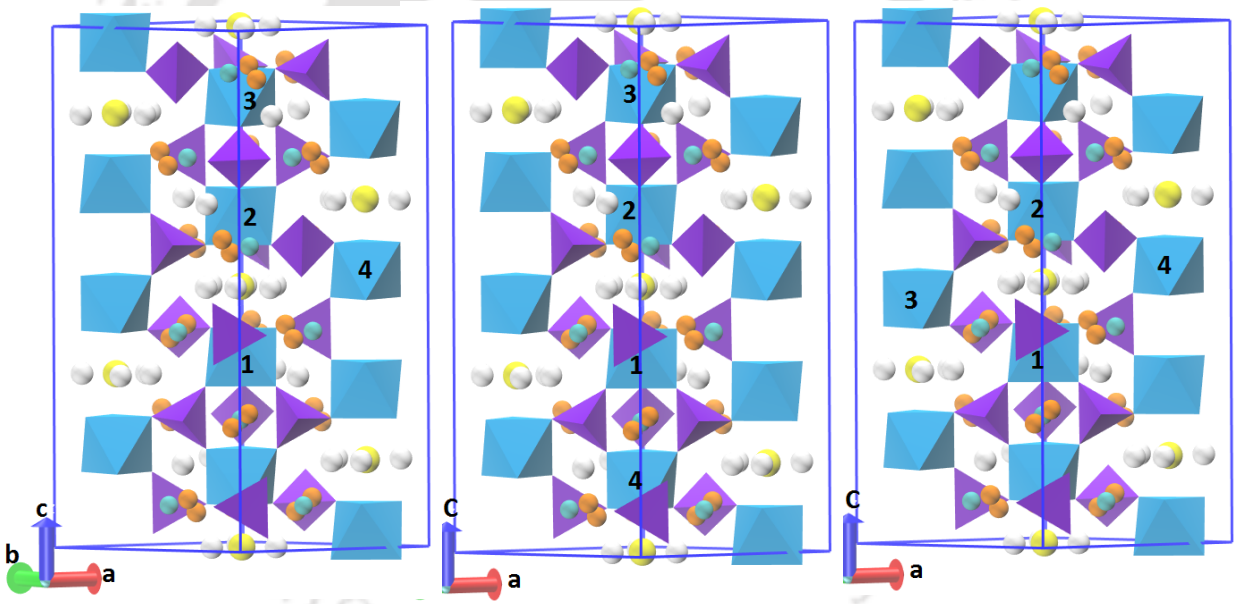

Figure 5-1. Polyhedra view of $Li_{1+x}Al_xTi_{2-x}(PO_4)_3$. $(Ti/Al)O_6$ octahedra (shown in color cyan) shares corners with PO_4 (purple) tetrahedra forming the three dimensional framework. The interstitial Li sites Li1 (yellow), Li2 (cyan), Li3 (orange) and mid-Li (white) are shown. Three different Al^{3+} ordering at the Ti^{4+} sites are shown; order1 (left), order2 (middle) and order3 (right). The indices mark the sequential order in which Al^{3+} is substituted for Ti^{4+} respectively for the compositions, x = 0.16, 0.33, 0.50 and 0.67.

systems remain largely speculative. While it is really hard to gain such atomistic level understanding by using experimental probes, computational methods such as molecular dynamics (MD) offers powerful alternative.

The present study employs molecular dynamics (MD) investigation on the NASICON-system, $Li_{1+x}Al_xTi_{2-x}(PO_4)_3$ ($0.0 \leq x \leq 0.67$), that stabilizes in the rhombohedral ($R\bar{3}c$ space group) structure. It is formed by infinite ribbons of $[Al_xTi_{2-x}(PO_4)_3]^-$ unit consisting of corner-shared $(Ti/Al)O_6$ octahedra and PO_4 tetrahedra. Several interstitial Li-sites such as Li1, mid-Li (mLi), Li2 [24] and Li3 [7] are reported (see table 5-1). The Li1-site (6b position) is surrounded by six O atoms forming $Li1O_6$ octahedra. Li2-site (18e position) is surrounded by irregular eight O atoms. Mid-Li is located between Li1 and Li2 with 5 coordinated O atoms. Another newly reported site Li3 as reported by Arbi *et al.* [7] is located between mid-Li and Li2, shown in Figure 5-1.

MD simulations are carried out at five different compositions of $Li_{1+x}Al_xTi_{2-x}(PO_4)_3$, namely, x = 0.0, 0.16, 0.33, 0.50, and 0.67. Insights into the structure, conductivity, ion occupancy at various sites, ion hopping paths from one site to another and free energy profiles have been derived along with the influences of Al^{3+}/Ti^{4+} ordering on diffusion of Li^+ ions.

Table 5-2. Inter ionic potential pair parameters employed in present study.

X	q_x (C)	σ_x (Å)	A_{XO} (eV)	C_{XO} (eVÅ^6)	n_{XO}
Li	0.702	0.59	0.1716	0.000	9
Ti	2.808	0.74	1.239	9.917	9
Al	2.106	0.67	0.852	9.279	9
P	3.510	0.31	3.616	9.279	9
O	-1.404	1.21	0.448	47.999	7

$A_{Li\text{-}Li}$ = 5.0 eV and $n_{Li\text{-}Li}$ = 11.

5.2 Computational Details

Isothermal and isobaric molecular dynamics (NPT-MD) simulations are carried out for the system $Li_{1+x}Al_xTi_{2-x}(PO_4)_3$ ($0.0 \leq x \leq 0.67$) from 450-700 K temperature and at 1 atm pressure employing Parrinello-Rahman-Vashishta form [25, 26] of interatomic potential,

$$V_{ij}(r_{ij}) = \frac{q_i q_j}{r_{ij}} + \frac{A_{ij}\left(\sigma_i + \sigma_j\right)^{n_{ij}}}{r_{ij}^{\,n_{ij}}} - \frac{C_{ij}}{r_{ij}^{\,6}} \qquad (5.1)$$

where q_i being charge and σ_i being the ionic radius of the i^{th} ion; A_{ij} and C_{ij} are respectively the overlapping repulsive energy and dispersion constant between the pair of ions. These parameters are listed in table 5-2. The partial charges of all ions and the pair parameters of P−O and O−O are taken from the previous study [20] and the parameters of the Ti−O, Al−O, Li−O and Li−Li pairs are calculated by the empirical fitting of the structure and conductivity. The present short range repulsion of the O−O pair is larger than the previous studies [20] as structural stability goes down with smaller ion (Li^+ and Al^{3+}) substitution. The simulated LATP supercell consists of 3×3×1 rhombohedral unit cells ($R\bar{3}c$ symmetry) having 972 to 1008 ions across the compositions range x = 0.00 to 0.67. The initial lattice parameters for all compositions are $a = b$ = 8.5109, c = 21.0 Å and $\alpha = \beta = 90^0$, $\gamma = 120^0$ [6, 27] and are allowed to evolved. A short range cutoff distance of about 10.5 Å is implemented.

These substitutions permits up to four Al^{3+} incorporation per unit cell. We have examined a few different ordering of Al^{3+} ion in the structures. The Al^{3+} ions are substituted at the Ti-sites sequentially in the order of the index, for compositions x = 0.16 to 0.67, as indicated in figure 5-1 (left), and named order1. The Al^{3+} ions are placed along c-axis of the octahedral ribbon as shown in order2 series (see figure 5-1). In the order2 series, x = 0.67 structure shows even higher conductivity than x = 0.33 composition, thus not following the reported trend in the conductivity. Again four Al^{3+} ions are placed at the four nearest octahedral centres of a TiO_6 octahedra sequentially as shown in order3 series. However, in the order3 series, for x = 0.67 structure the octahedral and tetrahedral connectivity in the skeleton are found to be broken indicating structural instability. Suggesting that these are

probably not formed in experiments as well. Hence the remaining of the analysis are carried out only for the order1-series in figure 5-1 (left).

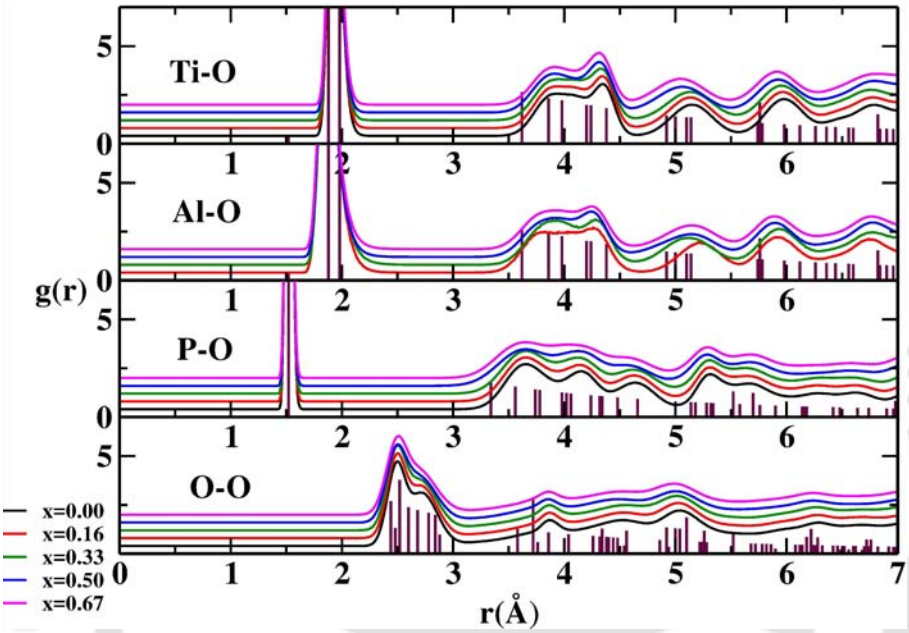

Figure 5-2. The radial distribution function (RDF), g(r), between selected ion pairs, Ti−O, Al−O, P−O, and O−O of $Li_{1+x}Ti_{2-x}Al_x(PO_4)_3$ across the compositions at 600 K from NPT-MD. The g(r)s calculated from the X-ray structure are shown as vertical bars in brown. The functions are displaced uniformly along Y-axis for clarity.

The Li^+ ions are placed at Li1 sites and extra Li ions are located randomly chosen Li3 sites. Then a series of isothermal-isobaric molecular dynamic simulations (NPT-MD) are performed systematically for all the above compositions and over the temperature range 450 to 700 K employing the software package LAMMPS [28]. The temperature and pressure are kept fixed by using Nose-Hoover thermostat and barostat respectively [29, 30]. Also a series of micro-canonical (NVE) MD simulations are performed at 600 K starting from the final configuration of the average cell parameters from the NPT-MD simulation for the investigation of Li^+ ion migration path and free energy distributions. Periodic boundary conditions are employed in all three directions together with Ewald summation technique for the convergence of long range Coulombic interactions. The run lengths are typically of 12 nanoseconds long with a time step of 2 femtoseconds including few nanoseconds of

equilibration. During the production phase the trajectory of the system are stored at intervals of 200 femtoseconds for further analysis. The averaging of structural and dynamical properties are calculated over 60000 frames.

Few more NPT-MD runs are performed for longer (25 nanoseconds) duration, for larger system (6×6×2 super cells). The structural stability of the LATP goes down beyond x = 0.67, supporting the experimental trend, wherein phase segregation and formation of phosphate glass is reported [31]. The thermal stability is also examined for all these compositions and system stability is examined up to 1200 K for compositions of $x \leq 0.33$. The x = 0.67 composition is not stable beyond 700 K supporting previous experimental studies [31].

Table 5-3. Lattice parameters across the composition calculated from NPT-MD at 600 K.

Compositions	a (Å)		c (Å)	
X	MD	Expt [7]	MD	Expt [7]
0.00	8.680	8.512	21.420	20.954
0.16	8.667	8.506	21.380	20.930
0.33	8.652	8.500	21.350	20.905
0.50	8.667	8.495	20.919	20.882
0.67	8.652	8.488	20.883	20.856

5.3 Results and Discussions

5.3.1 Structure

The LATP skeleton is formed by corner shared $(Ti/Al)O_6$-octahedra and PO_4-tetrahedra. The Ti−O, Al−O, and P−O radial distribution functions (RDFs) are shown in figure 5-2 at 600 K for x = 0.0, 0.16, 0.33, 0.50, and 0.67 compositions from NPT-MD. The RDFs calculated from XRD structure by Arbi *et al.* [27], represented by vertical lines, is shown as the reference in figure 5-2. The average bond distances for bonded pairs Ti−O, Al−O, and P−O, are 1.93, 1.86 and 1.52 Å respectively at 600 K from NPT-MD. The first peak of the Al−O RDFs are broader than Ti−O for the LATP system owing to their weaker interaction compared to the Ti−O pair. The coordination numbers for Ti^{4+}/Al^{3+} and P^{5+} are found to be sharp at 6, and 4 oxygens respectively for all the compositions confirming that $(Ti/Al)O_6$

octahedra and PO_4 tetrahedra are intact. The angles of the rhombohedral unit cell are also closed to the expected values (not shown), $\alpha = \beta = 90°$ and $\gamma = 120°$. The variation of lattice parameters with compositions obtained in this study suggests that the trend across the compositions have been successfully reproduced.

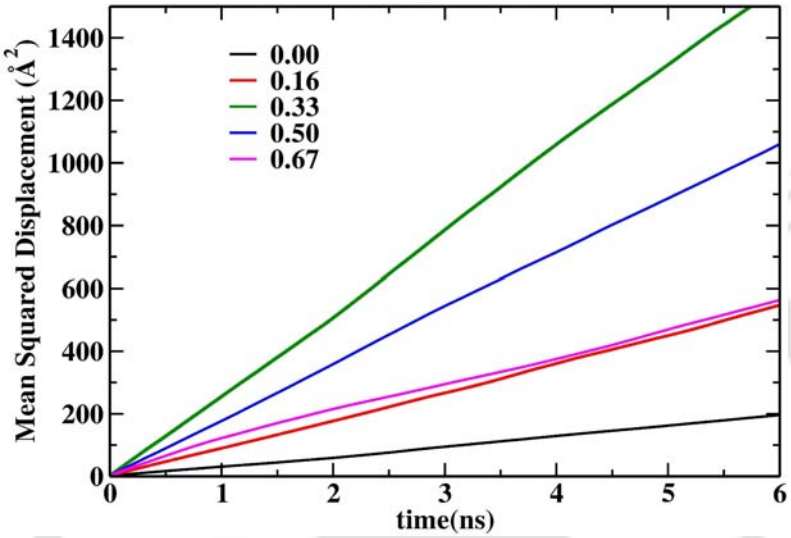

Figure 5-3. The mean square displacement (MSD) of Li^+ ions for several compositions $Li_{1+x}Ti_{2-x}Al_x(PO_4)_3$ from NPT-MD simulation at 600 K.

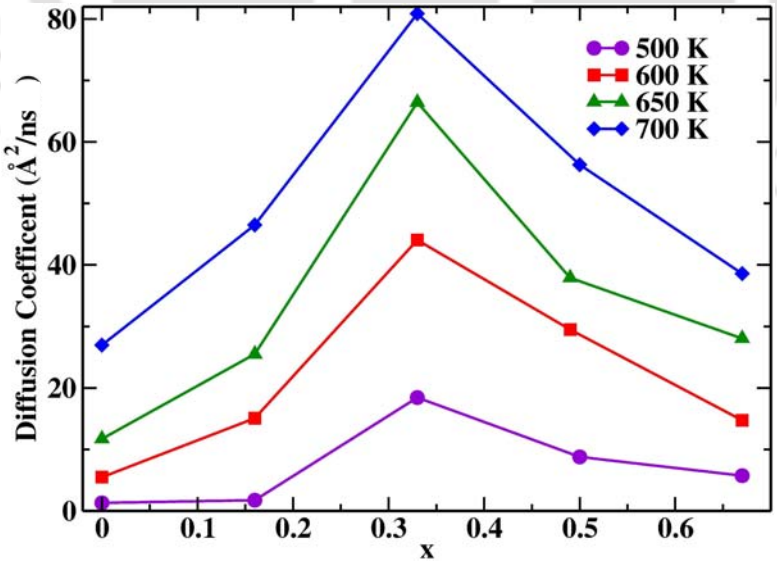

Figure 5-4. Diffusion coefficient vs several compositions for the compositions x = 0.00, 0.16, 0.33, 0.50 and 0.67 with mentioned temperature range.

5.3.2 Conductivity and Ionic Motion

Mean square displacement (MSD) of Li^+ ions are calculated and it is gradually increasing in time following Einstein diffusion equation for all compositions (figure 5-3). The Diffusivity is enhanced for $x = 0.33$ composition by one order of magnitude at 500 K (see figure 5-4). The conductivity, σ, is also calculated following the Nernst−Einstein relation,

$$\sigma = \frac{nq^2D}{k_BT} \tag{5.2}$$

where n is the mobile ion density (varies with compositions x), q is the formal charge of Li^+ (+1|e|), k_B – the Boltzmann constant, and T – the temperature in Kelvin.

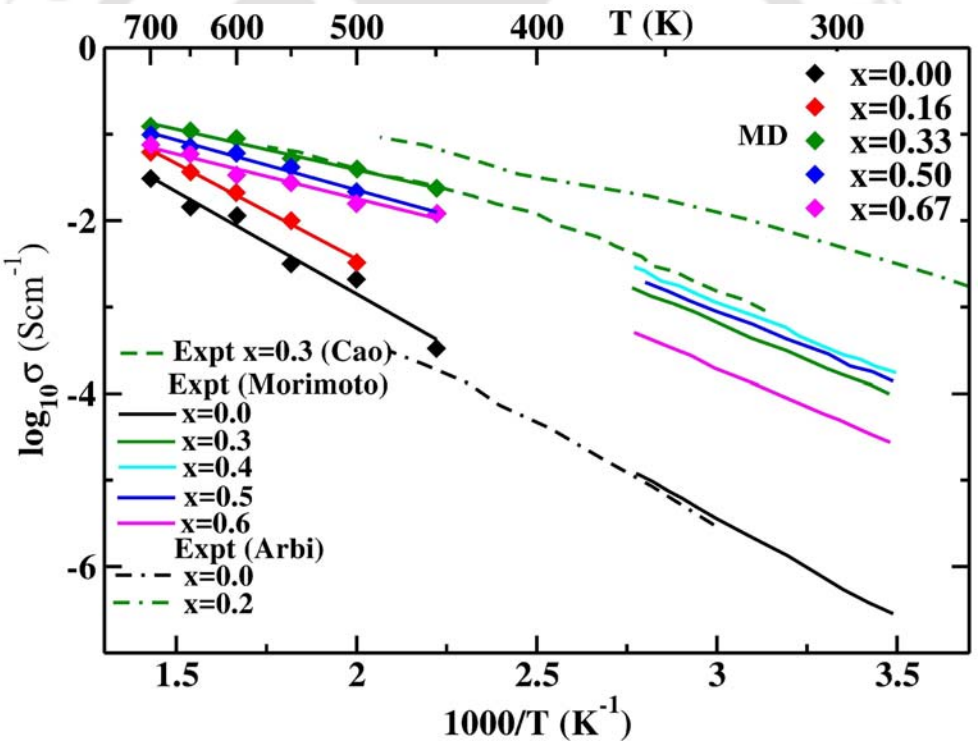

Figure 5-5. Arrhenius plot of Li^+ conductivity for $Li_{1+x}Ti_{2-x}Al_x(PO_4)_3$ where $0.0 \le x \le 0.67$ from MD simulation (shown in diamond symbol) over 400-700 K. The experimental data are extracted from the figures of Arbi *et al.* [7, 32], Morimoto *et al.* [31] and Cao *et al.* [33].

The compound at $x = 0.33$ has shown a conductivity value of $\sigma \approx 0.1$ Scm^{-1} at 600 K while pure LATP ($x = 0.0$) reveals poor conductivity ($\sigma \approx 0.01$ Scm^{-1} at T = 600 K).

The Arrhenius plots for the various compositions are generated from the conductivity calculation as shown in figure 5-5 and are compared with the available experimental results [7, 31, 34]. We have performed our study at high temperature to get better statistics. However, the conductivity variation with temperature are quite comparable qualitatively as reported in experiments. The activation energies are also computed following Arrhenius equation,

$$\sigma = \sigma_0 exp\left(-E_a / k_B T\right) \tag{5.3}$$

where E_a is the activation energy, σ_0 is the pre-exponential factor, k_B is the Boltzmann constant and T is the absolute temperature. The E_a for all compositions are listed in table 5-4. The activation energy reduces with compositions and shows an anomalous behavior at x = 0.33 agreeing with experimental report [6, 7].

Table 5-4. Comparison of composition vs. activation energy and free energy barrier.

X	Activation energy (E_a) in eV		Free Energy Barrier
	MD	Experiment	(eV)
0.00	0.472	0.49 [6], 0.31 [7]	0.32
0.16	0.441	--	0.23
0.33	0.187	0.29 [6], 0.18 [7] (x = 0.2)	0.19
0.50	0.230	0.28 [31]	0.22
0.67	0.206	0.26 [31] (x = 0.6)	0.24

5.3.3 Microscopic Details

Two types of bottlenecks are present in the pathway of Li^+ ion migration. These bottlenecks are located at distances 1.2 Å (between Li1 and mid-Li) and 2.21 Å (between mid-Li and Li2) from Li1 sites described in previous studies [4, 18, 35]. The bottleneck radii, labelled as r1 and r2, are calculated from NPT-MD for all the compositions and listed in table 5-5. Both of them have reduced with the increasing compositions (x) and have increased with increasing temperature. However, these changes are marginal. Thus not a significant factor for the observed conductivity variation, supporting previous literatures [8, 11].

Table 5-5. Bottleneck radius (Å) for Li^+ ion transport in $Li_{1+x}Ti_{2-x}Al_x(PO_4)_3$.

Temp (K)	Compositions									
	x = 0.00		x = 0.16		x = 0.33		x = 0.49		x = 0.67	
	r1(Å)	r2(Å)	r1(Å)	r2(Å)	r1(Å)	r2(Å)	r1(Å)	r2(Å)	r1(Å)	r2(Å)
450	2.2203	2.1964	2.2202	2.1930	2.2217	2.1891	2.2178	2.1840	2.2112	2.1774
500	2.2213	2.1971	2.2210	2.1936	2.2217	2.1893	2.2187	2.1848	2.2113	2.1777
550	2.2229	2.1980	2.2226	2.1944	2.2230	2.1903	2.2191	2.1853	2.2122	2.1785
600	2.2246	2.1990	2.2247	2.1956	2.2243	2.1910	2.2196	2.1859	2.2133	2.1793
650	2.2274	2.2005	2.2273	2.1969	2.2267	2.1923	2.2210	2.1868	2.2146	2.1802
700	2.2303	2.2021	2.2301	2.1984	2.2288	2.1935	2.2227	2.1880	2.2148	2.1806

Table 5-6**.** Population of Li^+ ions at the Li1, mid-Li and Li3 sites.

X	Li1	mid-Li	Li3
0.00	0.49	0.47	0.04
0.16	0.46	0.33	0.20
0.33	0.37	0.29	0.32
0.50	0.36	0.28	0.36
0.67	0.37	0.20	0.43

The negligible counts at Li2 sites (not shown) is already reflected from iso-surface plots (figure 5-6). The counts at Li3 increases, while that at Li1 and mid-Li sites decreases with composition (shown in Table 5-6). Thus presence of extra Li^+ ions make the Li1 sites uncomfortable. This observations is in qualitative agreement with the neutron diffraction results by Arbi *et al.*[7].

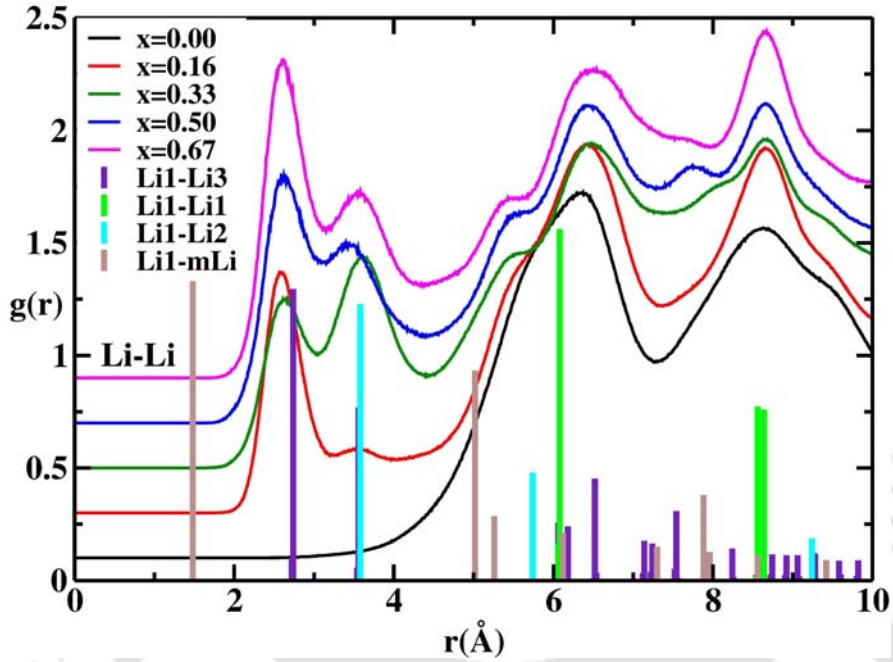

Figure 5-6. The radial distribution functions, g(r), for pairs Li-Li of the system $Li_{1+x}Ti_{2-x}Al_x(PO_4)_3$ for different compositions. The bar plots are indicating Li1-Li1, Li1-Li2, Li1-mLi and Li1-Li3 RDFs calculated from XRD-structure. The functions are displaced uniformly along y-axis.

We have also shown the RDFs (figure 5-6) of different Li-sites from Li1 sites by the bar plots. The other distances such as Li2-Li3, Li2-mLi, Li2-Li2 etc. are not shown to avoid complexity. Absence of peak near 1.5 Å, corresponding to Li1-mLi distance indicates that simultaneous occupancy of Li1 and mid-Li is not allowed due to Li^+−Li^+ repulsion. The first and second peaks of the x = 0.0 system shows up near 6.3 Å and 8.7 Å corresponding roughly to the Li1−Li1 first and second neighboring distances. Therefore, x = 0.0 system limits Li^+ occupy only to Li1 sites as detected by XRD [7]. Notably in LATP structure (x > 0.0), peaks near 2.64 and 3.57 Å occurs due to the additional lithium ions. The peaks at 2.74 Å and 3.56 Å for LATP (x > 0.0) correspond to first and second Li1−Li3 neighboring distances respectively. Thus occupancy at Li3 site is allowed for LATP systems supporting several recent literatures [7, 36, 37].

In order to understand the microscopic motion of the Li^+ ions, the coordinates of the Li^+ are mapped into a single unit cell and is divided the whole unit cell into three dimensional grids.

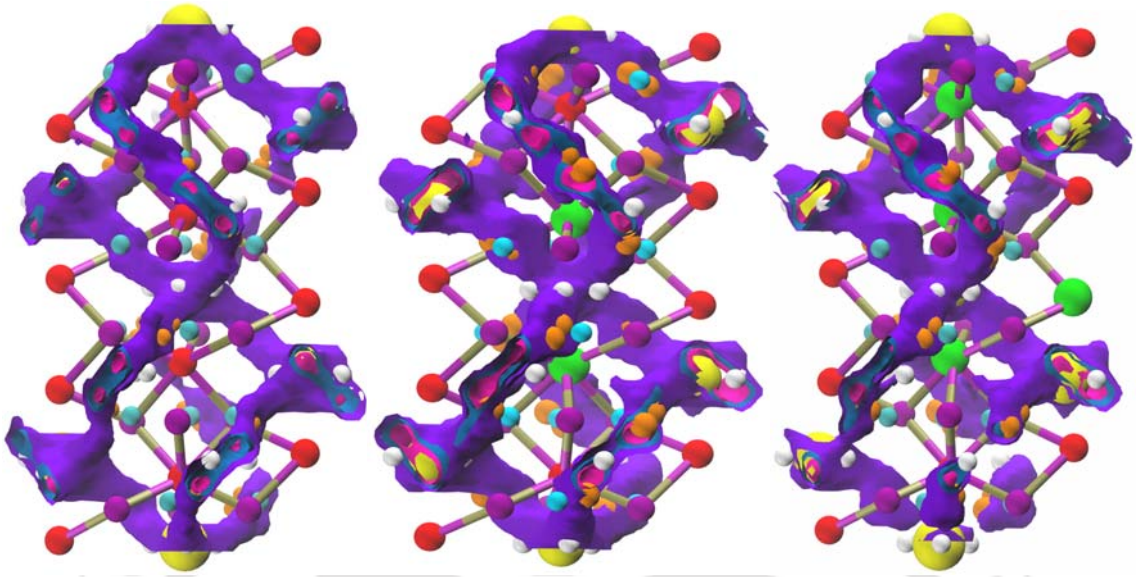

Figure 5-7. Three dimensional population distribution of Li^+ ions (violet) in rhombohedral unit cell with framework structure (ball and stick): P^{5+} (red), Ti^{4+} (purple), Al^{3+} (green) connected through O (not shown); for all compositions at 600 K. The interstitial Li sites are indicated by Li1(yellow), Li2 (cyan), Li3 (orange) and mid-Li (white). Different colored iso-surfaces indicate different iso-values.

The populations are counted in each grid to generate the iso-surface plot (figure 5-7) of the Li^+ ion population for the normalized iso-values of the corresponding compositions along with the framework and all Li sites and the outer surface indicates smaller iso-value. It displays the demonstration of the three dimensional population distribution and the connecting ion channels are clearly visible. This is the direct qualitative evidence of different site preferences. Essentially, there are six channels (three up and three bottom) coming out from the each Li1 site for all compositions. For $x = 0.0$ system, Li^+ ion shows high populations at Li1 sites and mid-Li (close to Li1) sites. On the other hand, the high populations of Li^+ is seen in Li1, mid-Li and some Li3-sites with Al^{3+} substitution. The ion channels for $x = 0.33$ is well connected resulting the highest diffusion. On the other hand some of the channels for $x = 0.67$ composition is broken resulting lower conductivity [7, 37].

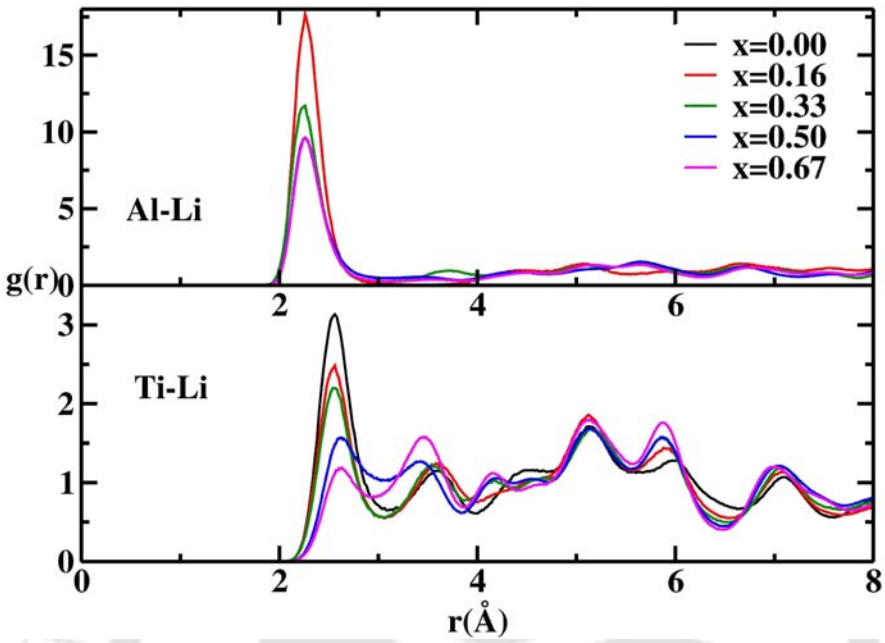

Figure 5-8. The radial distribution functions, g(r), for pairs Al-Li (top) and Ti-Li (bottom) in $Li_{1+x}Ti_{2-x}Al_x(PO_4)_3$ for all compositions at 600 K.

Al−Li and Ti−Li RDFs are also investigated across the composition to observe the local environment of Li near the Al or Ti (figure 5-8). The Ti-Li RDFs deviate significantly from Ti-Li RDFs for the x = 0.0 system. The first peak appears near 2.57 Å for all compositions and heights are diminishing with increasing Al^{3+} ion. Therefore, the number of Li^+ ions near Ti^{4+} reduces with the composition in presence of more Li-Li repulsion, while first peak of Al−Li is located near 2.28 Å and peak heights are higher compared to Ti−Li RDFs. Hence, Li^+ prefers to come closer to Al^{3+} than Ti^{4+} due to its smaller ionic radius and lower charge of Al^{3+}.

The free energy along the path of two neighboring Li1 sites has been calculated from the population following the equation 5.4. The population density distribution ($P(r)$) of Li^+ inside a cylinder of cross-sectional radius 1.0 Å connecting all Li1 to nearest Li1 is counted, as a function of distance r from its original Li1 site, and normalized such that $\int_V P(r)dV = 1$ (where dV is elementary volume of the cylinder). Free energy distributions are obtained from population density distribution [38, 39] (figure 5-9) for all compositions [40] following the equation,

$$\Delta F = -k_B T \ln P(r) \tag{5.4}$$

where T is the temperature in Kelvin and k_B is the Boltzmann constant.

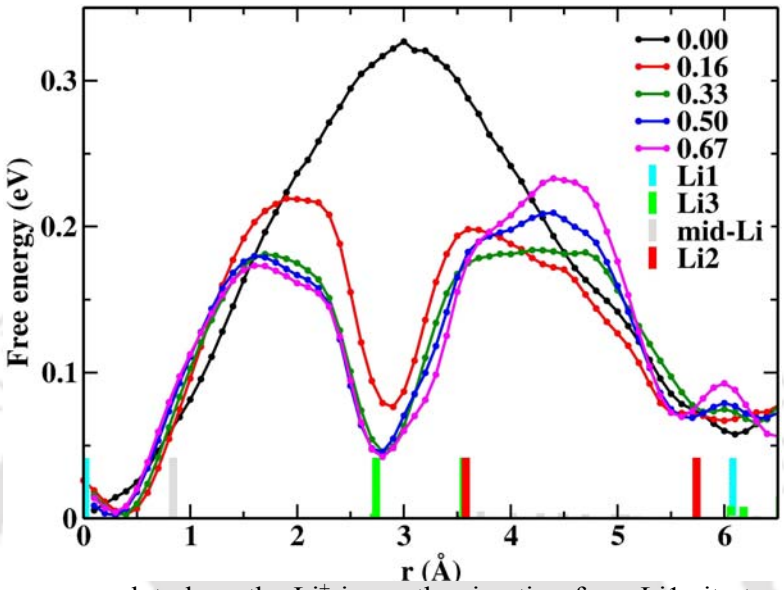

Figure 5-9. Free energy plot along the Li^+ ion path migration from Li1 site to another nearest Li1 site. x = 0.33 shows the least free energy barrier height roughly 0.19 eV and x = 0.0 composition exhibits highest (0.32 eV). The extra minima appear for x > 0.0 reported as Li3 sites.

Interestingly, the free energy distribution for x = 0.0 along the connecting Li1−Li1 site shows two minima at two Li1 sites and an extra minima is found for all x > 0.0 compositions. The intermediate minima is found at around Li1-Li3 distance which is consistent with Li−Li RDFs peak at 2.8Å. Two such minima are expected for composition x > 0.0 composition due to splitting of the Li3 sites. However, their separation is around 0.86 Å only. The free energy barrier heights are listed in the table 5-5 obtained from the figure 5-9. The free energy barrier is maximum (0.32 eV) for x = 0.0 composition and least (0.19 eV) for x = 0.33 following qualitative trend with the activation energies.

5.4 Conclusion

Molecular dynamics study has been carried out on the system $Li_{1+x}Ti_{2-x}Al_x(PO_4)_3$ ($0.0 \leq x \leq 0.67$) employing refined potential parameters. It reproduces gross structural properties, such as, lattice parameters, Ti-O and Al-O bond lengths, and conductivity variation across the compositions. The variation of bottleneck size across the series is found marginal. Hence it

does not play a significant role on the conductivity variation observed. For x = 0.0 composition, all the Li^+ occupies energetically favorable Li1 sites resulting low Li^+ diffusion. The incorporation of additional Li^+ ions in the system forces them to explore new sites (Li3) which are energetically less preferable but more in number (thirty six compared to six Li1 sites in a single unit cell). The increase Li3 site occupancy is supported by Li−Li RDFs, three dimensional Li^+ ion distribution and free energy distribution along the conduction channel. The population at Li1 and mid-Li sites decreases systematically with composition, while that at the Li3 site increases. At x = 0.33 composition, the population of Li^+ ions at the various sites, Li1, mid-Li, Li3, are nearly equal. This indicates higher Li^+ disorder across the Li-sites gaining more entropy for the system. Hence x = 0.33 composition produces best conductivity among the series.

Bibliography

[1] N. Anantharamulu, K. Koteswara Rao, G. Rambabu, B. Vijaya Kumar, V. Radha, M. Vithal, *J Mater Sci* **46** (2011) 2821.
[2] H.P. Hong, *Mater. Res. Bull.* **11** (1976) 173.
[3] J.B. Goodenough, H.P. Hong, J.A. Kafalas, *Mater. Res. Bull.* **11** (1976) 203.
[4] H. Kohler, H. Schulz, *Mater. Res. Bull.* **20** (1985) 1461.
[5] C. Masquelier, L. Croguennec, *Chem. Rev.* **113** (2013) 6552.
[6] K. Arbi, J. Rojo, J. Sanz, *J. Eur. Ceram. Soc.* **27** (2007) 4215.
[7] K. Arbi, M. Hoelzel, A. Kuhn, F. García-Alvarado, J. Sanz, *Inorg. Chem.* **52** (2013) 9290.
[8] M. Pérez-Estébanez, J. Isasi-Marín, D. Többens, A. Rivera-Calzada, C. León, *Solid State Ionics* **266** (2014) 1.
[9] B. Wang, M. Greenblatt, S. Wang, S. Hwu, *Chemistry of Materials* **5** (1993) 23.
[10] K. Arbi, M. Paris, J. Sanz, *J. Phys. Chem. B* **110** (2006) 6454.
[11] H. Aono, E. Sugimoto, Y. Sadaoka, N. Imanaka, G.y. Adachi, *J. Electrochem. Soc.* **137** (1990) 1023.
[12] B.E. Francisco, C.R. Stoldt, J.-C. M'Peko, *J. Phys. Chem. C* **119** (2015) 16432.
[13] J. Emery, T. Šalkus, M. Barré, *J. Phys. Chem. C* **121** (2017) 246.
[14] K. Takahashi, J. Ohmura, D. Im, D. Lee, T. Zhang, N. Imanishi, A. Hirano, M. Phillipps, Y. Takeda, O. Yamamoto, *Journal of the Electrochemical Society* **159** (2012) A342.
[15] C. Vinod Chandran, S. Pristat, E. Witt, F. Tietz, P. Heitjans, *J. Phys. Chem. C* **120** (2016) 8436.
[16] A. Martínez-Juárez, C. Pecharromán, J.E. Iglesias, J.M. Rojo, *J. Phys. Chem. B* **102** (1998) 372.
[17] J.T. Kummer, *Prog. Solid State Chem.* **7** (1972) 141.
[18] P. Padma Kumar, S. Yashonath, *J. Phys. Chem. B* **106** (2002) 3443.
[19] K. Kang, Y.S. Meng, J. Bréger, C.P. Grey, G. Ceder, *Science* **311** (2006) 977.
[20] P. Padma Kumar, S. Yashonath, *J. Am. Chem. Soc.* **124** (2002) 3828.
[21] J.P. Boilot, G. Collin, P. Colomban, *J. Solid State Chem.* **73** (1988) 160.
[22] J.P. Boilot, G. Collin, P. Colomban, *Mater. Res. Bull.* **22** (1987) 669.
[23] S. Roy, P. Padma Kumar, *Phys. Chem. Chem. Phys.* **15** (2013) 4965.
[24] B. Lang, B. Ziebarth, C. Elsasser, *Chemistry of Materials* **27** (2015) 5040.
[25] P. Vashishta, A. Rahman, *Phys. Rev. Lett.* **40** (1978) 1337.
[26] M. Parrinello, A. Rahman, P. Vashishta, *Phys. Rev. Lett.* **50** (1983) 1073.
[27] K. Arbi, M. Hoelzel, A. Kuhn, F. García-Alvarado, J. Sanz, *Inorg. Chem.* **52** (2013) 9290.
[28] M.L. Parks, S.J. Plimpton, R.B. Lehoucq, S.A. Silling, *Sandia National Laboratory Report, SAND2008-0135, Albuquerque, New Mexico* (2008).
[29] G.J. Martyna, D.J. Tobias, M.L. Klein, *J. Chem. Phys.* **101** (1994) 4177.
[30] M. Parrinello, A. Rahman, *Journal of Applied Physics* **52** (1981) 7182.

[31] H. Morimoto, M. Hirukawa, A. Matsumoto, T. Kurahayashi, N. Ito, S.-i. Tobishima, *Electrochemistry* **82** (2014) 870.
[32] C. Chen, Z. Lu, F. Ciucci, *Sci. Rep.* **7** (2017) 40769.
[33] C. Cao, Z.B. Li, X.L. Wang, X.B. Zhao, W.Q. Han, *Front. Energy Res.* **2** (2014).
[34] C. Cao, Z.-B. Li, X.-L. Wang, X.-B. Zhao, W.-Q. Han, *Front. Energy Res.* **2** (2014) 25.
[35] D.T. Qui, J.J. Capponi, J.C. Joubert, R.D. Shannon, *J. Solid State Chem.* **39** (1981) 219.
[36] M. Monchak, T. Hupfer, A. Senyshyn, H. Boysen, D. Chernyshov, T. Hansen, K.G. Schell, E.C. Bucharsky, M.J. Hoffmann, H. Ehrenberg, *Inorganic Chemistry* **55** (2016) 2941.
[37] B. Lang, B. Ziebarth, C. Elsässer, *Chemistry of Materials* **27** (2015) 5040.
[38] D. Frenkel, B. Smit, *Understanding molecular simulation: From algorithms to applications* (1996).
[39] F. Reif, *Fundamentals of statistical and thermal physics*, McGraw-Hill: (**1985**).
[40] P.P. Kumar, S. Yashonath, *J. Phys. Chem. B* **106** (2002) 7081.

Chapter 6

Conclusion

Fast ion conducting solids are a technologically important class of materials, particularly for battery and fuel cell applications. A brief survey of the state-of-the-art of materials for such applications is presented in Chapter 1 of this thesis. The development of better batteries and fuel cells demand search for solid electrolytes with significantly higher ionic conductivities. This search for improved fast ion conducting solids would be greatly benefitted if the factors influencing fast ion transport in solids could be better understood. Atomistic simulation techniques, such as molecular dynamics, discussed in Chapter 2 of the thesis, forms one of powerful methods to gain such insights. Later chapters discuss molecular dynamics studies on two of the promising fast ion conductors namely, $Na_2M_2TeO_6$ (M = Ni, Zn, Co and Mg). and $Li_{1+x}Al_xTi_{2-x}(PO_4)_3$ ($0.0 \leq x \leq 0.67$), and insights on microscopic factors that facilitate fast ion conduction in these systems is highlighted.

In Chapter 3 of the thesis discusses molecular dynamics simulation studies on the recently discovered family of superionic conductor $Na_2M_2TeO_6$ (M = Ni, Zn, Co and Mg). An inter atomic potential is developed for this system empirically by fitting of the structure and conductivity. The proposed potential reproduces several structural and dynamical properties. The calculated lattice parameters and bond lengths of the framework species are in excellent agreement with previous experimental results. The Ni composition produces best Na^+ conductivity in this series with least activation energy. The temperature dependence of the ionic conductivity of the series is also in agreement with the reported experimental results. The occupancy of Na^+ ions at Na1, Na2 and Na3 sites are calculated. The Na+ population at Na1 and Na2 sites is found comparable, whereas Na3 site remains unvisited. The calculated potential energy distribution on the conducting plane finds the

energy minima at Na2 sites. No minima in potential energy is observed at the Na3 sites. Despite this the population profile finds the maxima at both the Na1 and Na2 sites. The Na-Na radial distribution function shows that the simultaneous occupancy at Na1 and Na2 sites is forbidden. It is argued that any kind of ordered arrangement of the Na^+ at the Na2 or Na1 blocks the diffusion paths. It hints upon the entropic contribution as population is fully determined by the free energy.

In order to investigate this aspect we have carried out MD simulation by varying the concentration of Na^+ at the interlayers, as detailed in Chapter 4. The concentration variation is effected though moving Na^+ ions from on interlayer to the very next layer maintaining charge conservation. The possible framework distortions due to this is minimal across most of concentration range. It is observed that the Na^+ diffusion is strongly influenced by the variation in concentration owing to the increase in the Na^+ - Na^+ repulsion. The ionic conductivity of the interlayer containing 20% lower concentration of Na^+ (than the normal concentration) is an order of magnitude higher.

The average potential energy landscape of individual Na^+ in the interlayer finds the energy minima at Na2 for all examined concentration with different depth. The overall energy goes higher with higher concentrations. Interestingly, the population profile of the under-loaded case, having 20% lower concentration of Na^+, follows the potential energy profile. At the normal concentration, the Na1 and Na2 are almost equally probable, while the population is mostly shifted to the Na1 sites for higher Na^+ concentration. Population at the energetically higher Na1 sites suggest increases in the entropy of the system. With the increase in concentration of Na^+, Na1 sites that are energetically less favorable starts populating, and the migration channels connecting Na2-Na1-Na2 emerge. The gradual evolution of the Na^+ population with concentration in favour of sites that are energetically less favorable but higher in multiplicity, reflect switching from an energy driven to entropy driven mechanism.

The Chapter 5 of the thesis discusses $Li_{1+x}Ti_{2-x}Al_x(PO_4)_3$, a NASICON type material. The MD study is performed for the material with composition $0.0 \leq x \leq 0.67$ with a refined pair potential. The proposed interatomic potential reproduces the structure and conductivity agreeing with experimental results. The general trend of cell parameter variation with compositions is found to be monotonically decreasing with the composition. At the lowest

concentration, $x = 0.0$, the Li+ ions are found localized at the Li1 sites. The incorporation of more Li^+ in to the system forces the system to explore energetically higher Li3 sites. The population of the Li3 sites is supported by occupancy estimates at various sites, Li–Li RDFs, three dimensional Li^+ ion distribution and free energy profile. The free energy distribution exhibits least barrier height for the $x = 0.33$ in the Li^+ migration. Further at this composition the Li1, mid-Li and Li3 sites have nearly equal occupancy. Thus the higher Li^+ disorder across the Li-sites promotes the entropy in the system, resulting in higher conductivity.

The thesis presents results from our molecular dynamics studies on some of the promising fast ion conducting solids, and brings out fresh insights on microscopic of ion transport mechanism and factors that influence ionic conductivity.

Publications

Journals:

1. Sau, K.; Kumar, P. P., Ion transport in $Na_2M_2TeO_6$: insights from molecular dynamics simulation. *J. Phys. Chem. C* **2015**, *119*, 1651-1658. (This publication is based on the Chapter 3.)
2. Sau, K.; Kumar, P. P., Role of Ion–Ion Correlations on Fast Ion Transport: Molecular Dynamics Simulation of $Na_2Ni_2TeO_6$. *J. Phys. Chem. C* **2015**, *119*, 18030-18037. (This publication is based on the Chapter 4.)
3. Sau, K., Influence of ion–ion correlation on Na^+ transport in $Na_2Ni_2TeO_6$: molecular dynamics study. Sau, K. *Ionics* **2016**, 22, 2379

Conference Proceedings:

4. Sau, K.; Kumar, P. P. In Molecular Dynamics Investigation of Na in $Na_2Ni_2TeO_6$, *AIP Conference Proceedings*, **2014**; 1361-1363. (This publication is based on the Chapter 3.)
5. Sau, K., Ion-Ion Repulsion And Entropic Effects On Na^+ Transport In $Na_2Ni_2TeO_6$: Molecular Dynamics Study. *AIP Conference Proceedings*, **2016**, 1728, 020119-1020119-4.